Technische Universiteit Delft

Master Thesis

An Investigation of a Prediction Method for Failure in the Transition Zones of Locally Reinforced CFRP Materials by Steel Hybridization

Kryštof Kořán

TU Delft DLR

Master Thesis

AE-4030

by

Kryštof Kořán

to obtain the degree of Master of Science
at the Delft University of Technology,
to be defended publicly on Friday July 13, 2018 at 9:30 AM.

Student number:	4512278	
Project duration:	November 13, 2017 – June 29, 2018	
Supervision:	Prof. Dr. ir. René Alderliesten,	TU Delft, University supervisor
	Dipl-Ing. Enno Petersen,	DLR Braunschweig, Daily supervisor

Abstract

Local metal hybridization is a practice, wherein composite layers are substituted by equally thick metallic foils in a finite region of the laminate. The method can be used to locally increase the bearing strength of the laminate, but also introduces a potential weak-point. The transition zone (TZ) between the fully composite and hybrid laminate must be carefully designed in order to avoid premature failure in this region.

In this research, a methodology is designed to predict failure behavior in the TZ under a tension-bending loading case. A tool is designed for a combined loading test, in which a specimen is eccentrically loaded in tension. Specimens with a tailored geometry and various TZ arrangements were designed and manufactured. With the use of digital image correlation and observations by microscopy, the results of the tests are used to validate a finite element model. Interlaminar failure is modeled using cohesive zone interfaces with parameters validated by experimental correlation. The Cuntze criterion is applied with a damage degradation model for characterizing intralaminar failure. Characteristics of a good TZ design are recognized based on knowledge of the sequence of events leading to failure. The principle of a good design is to increase the moment of inertia by placing steel foils at outer positions, to the extent where the increased tendency for delamination does not become critical. A methodology is set up as a tool for future designers to evaluate and (algorithmically) optimize their local hybridization designs.

Acknowledgments

First and foremost, my thanks go to my thesis supervisor at DLR Dipl.-Ing. Enno Petersen. His incredible attention and openness to discussion all throughout the thesis helped make this project a valuable learning experience.

I would also like to thank Prof.Dr.ir. René Alderliesten. His challenging but helpful questions and comments were always able to steer the project in the right direction.

Lastly, my gratitude goes to my family and greater family at home and in the world. To Joshua for helping me see the bigger picture. To Isa for her love during this time. To my parents Ilona and Pavel for their support, for giving me the privileged opportunity to pursue higher education in the first place.

Kryštof Kořán
Braunschweig, June 2018

Contents

List of Figures ix

List of Tables xi

1 Introduction 1
- 1.1 Challenges of Joining in CFRP . . . 1
- 1.2 Scope and Aims . . . 2

2 Project Background 5
- 2.1 Technological Background . . . 5
  - 2.1.1 History of Fiber Metal Laminates . . . 5
  - 2.1.2 Mechanical Properties of FMLs . . . 7
- 2.2 Failure Types in Unidirectional Composites and FMLs . . . 11
  - 2.2.1 Intralaminar Failure . . . 11
  - 2.2.2 Interlaminar Failure . . . 13
- 2.3 Failure in joining . . . 14
- 2.4 Failure Criteria . . . 15
- 2.5 ATLAS Project Background . . . 18
  - 2.5.1 Layup design . . . 18
  - 2.5.2 Loading Case . . . 18

3 Experimental method 19
- 3.1 Previous Investigations of the Transition Zone . . . 19
- 3.2 Design of a Test for Combined Loading . . . 21
  - 3.2.1 Calculation of Loading Ratio . . . 22
  - 3.2.2 Design of Tooling . . . 23
- 3.3 Specimen Design . . . 23
  - 3.3.1 Layup . . . 24
  - 3.3.2 Transition Zone Design . . . 25
  - 3.3.3 Specimen Geometry . . . 26
- 3.4 Specimen Manufacturing . . . 26
  - 3.4.1 Preparation and Surface Treatment . . . 27
  - 3.4.2 Laminate Layup and Curing . . . 27
  - 3.4.3 Specimen Preparation and Quality Inspection . . . 28
- 3.5 Strain measurement with Digital Image Correlation . . . 30
  - 3.5.1 Specimen Preparation and System Setup . . . 30
  - 3.5.2 Measurement and Calculation . . . 31

4 Finite Element Modelling **33**
4.1 Modelling Interlaminar and Intralaminar Failure . . . 33
4.1.1 Virtual Crack Closure Technique . . . 33
4.1.2 Cohesive Zone Modelling . . . 34
4.2 Modelling Strategy . . . 36
4.2.1 Surface Definition and Interaction Properties . . . 37
4.2.2 Meshing Strategy and Boundary Conditions . . . 42
4.2.3 Material properties . . . 43
4.2.4 Stiffness Degradation and Damage . . . 43

5 Results and Discussion **45**
5.1 Test Results . . . 45
5.1.1 Suitability of the Test . . . 45
5.1.2 Load/Displacement Response . . . 46
5.1.3 Failure Identification by Microscopy . . . 47
5.1.4 Strain Field Analysis with DIC . . . 50
5.2 Numerical Results . . . 52
5.2.1 Model Correlation . . . 52
5.2.2 Failure Mode Identification . . . 52
5.2.3 Predictive Capabilities of the Model . . . 56
5.2.4 Variation of Step Distance . . . 57
5.3 Relation of Results to the ATLAS project . . . 58
5.4 Discussion Summary . . . 59

6 Conclusion **63**

7 Appendix **65**

Bibliography **73**

List of Figures

1.1 TZ in a CFRP bolted laminate [21] . . . 1

2.1 Absolute bearing strengths of Steel/CFRP and HTCL laminates with varying metal content.[19] 9
2.2 Comparison of specific bearing strength in HTCL and steel/CFRP laminates [19] . . . 10
2.3 Failure modes in composites . . . 11
2.4 Microfailure modes under tensile loading [42] . . . 12
2.5 Common failure modes in fibers and matrix alone, and in UD composites[23] . . . 13
2.6 Micrographs illustrating failure modes in UD composites[57] . . . 14
2.7 Crack growth modes: I Opening II Shearing III Tearing . . . 14
2.8 Failure modes in bolted laminates: (a) shear-out (b) net tension failure (c) cleavage (d) bearing failure. Combinations of failures modes are also possible [42] Pin bearing test setup with ratios dimensions labels[22] . . . 15
2.9 Tension and compression Fiber Failure (FF) and compression, tension and shear induced Inter Fiber Failure (IFF) modes[15] . . . 17

3.1 TZ arrangements investigated by Petersen et al. [56] . . . 19
3.2 Strain field in the TZs of bearing loaded FML specimens [60] . . . 20
3.3 Hinged clamp tooling used by [37] . . . 22
3.4 Experimental setup . . . 24
3.5 TZ arrangements: a) Short-Long b) Long-Short c) Short-Long-Short d) Long-Short-Long 25
3.6 Dimensioned specimen drawing . . . 26
3.7 Laminates on the tool with sealant tape dams to prevent resin flow out . . . 27
3.8 Autoclave laminate curing cycle . . . 28
3.9 Microscopic images of TZ cross-sections . . . 29
3.10 Manufacturing steel foil edge imperfections . . . 29
3.11 Typical 2D DIC setup[52] . . . 31

4.1 Dugdale Barenblatt crack model cohesive zone [62] . . . 34
4.2 Plots of cohesive constitutive equations [82] . . . 35
4.3 Benchmark DCB and ENF test simulation correlations . . . 39
4.4 Correlation of ENF experimental and model results using experimentally obtained ERR 40
4.5 Effect of increasing interlaminar strength in FEM ENF test for a steel-0° interface Legend nomenclature: mode I strength - mode II/III strength - mode I ERR - mode II/III ERR . . . 41
4.6 Edge effects observed in DCB and ENF simulations - crack progression in x-direction 41
4.7 Model simplification and loading . . . 43

5.1 Strain variation at opposing APs in TZ1-5 . . . 46
5.2 TZ1 Test data with FEM overlay . . . 47

5.3 Comparison of average experimental series failure loads and displacements 48
5.4 Crack growth at abutting points 49
5.5 Crack growth through composite layers 49
5.6 Delaminations not originating at APs 49
5.7 Loss of spleckle pattern due to specimen cracking 50
5.8 TZ1-4 Longitudinal strain in x 51
5.9 TZ1-4 Shear strain in xy 51
5.10 Local model correlation of DIC and FEM displacement of TZ1-4 52
5.11 First separation at AP initiating at foil edge 53
5.12 Delamination visualization with the quadratic traction criterion 54
5.13 Delamination visualization with the quadratic traction criterion 54
5.14 Damage criterion indicating delamination along long TZ1 foil (path shown in figure 5.12) 55
5.15 TZ1 matrix tensile damage failure mode index 55
5.16 TZ2 Tensile fiber failure mode criterion visualization 56
5.17 Comparison of ultimate failure force across TZs from FEM results with deviation from experimental values 57
5.18 FEM results for TZ5 with varying step lengths 58
5.19 Suggestion of an ordering for the ATLAS laminate with an initial spacing of 10 mm . . 59
5.20 State of damage at 11.7 kN of loading 60
5.21 State of damage at 14.5 kN of loading 61
5.22 Fiber damage leading to ultimate failure at a load of 20.7 kN 61

7.1 TZ2 Machine force/displacement output 65
7.2 TZ3 Machine force/displacement output 66
7.3 TZ5 Machine force/displacement output 66
7.4 TZ6 Machine force/displacement output 67
7.5 TZ2-1 Shear strain 67
7.6 TZ2-1 Strain 68
7.7 TZ3-4 Shear strain 68
7.8 TZ3-4 Strain 69
7.9 TZ5-1 Shear strain 69
7.10 TZ5-1 Strain 70
7.11 TZ6-5 Shear strain 70
7.12 TZ6-5 Strain 71
7.13 TZ1 Tensile fiber failure mode criterion visualization 71
7.14 TZ3 Tensile fiber failure mode criterion visualization 71
7.15 TZ4 Tensile fiber failure mode criterion visualization 72
7.16 TZ6 Tensile fiber failure mode criterion visualization 72

List of Tables

3.1 Test matrix showing excluded samples 30

4.1 Mode I, II and III fracture toughness for various material interfaces [54] 38
4.2 Prepreg and steel foil elastic and strength material properties 43
4.3 Stiffness degradation in each failure mode (FM) 44

Nomenclature

Δa	VCCT element length
Δu	VCCT nodal displacement
Δv	VCCT nodal displacement
μ_b	Coefficient of friction of the bolt
μ_{12}	Poisson's ratio in the 12 direction
μ_{23}	Poisson's ratio in the 23 direction
σ_x	Stress in x
σ_y	Stress in y
τ^0	Cohesive strength
τ_{xy}	Shear stress in xy
b	VCCT specimen width
D	Bolt diameter
E	Young's modulus
e	Eccentricity
E_3	Material through-thickness Young's modulus
$E11$	Young's modulus in the 11 direction
$E22$	Young's modulus in the 22 direction
$E33$	Young's modulus in the 33 direction
F	Force
G_I	Energy release rate in mode I
G_{12}	Shear modulus in the 12 direction
G_{13}	Shear modulus in the 13 direction
G_{23}	Shear modulus in the 23 direction
G_{III}	Energy release rate in mode III
G_{II}	Energy release rate in mode II

I	Second moment of inertia
K	Interface stiffness
l_{cz}	Cohesive zone length coefficient
M	Moment
S_{12}	In-plane shear allowable
T	Bolt tensioning torque
X^c	Compressive stress allowable in x
X^t	Tensile stress allowable in x
X_1	VCCT nodal force in x
y	transverse displacement
Y^c	Compressive stress allowable in y
Y^t	Tensile stress allowable in y
Y_1	VCCT nodal force in y
Z_1	VCCT nodal force in z
AP	Abutting Point
CF	Carbon Fiber
CFRP	Carbon Fiber Reinforced Polymer
CTE	Coefficient of Therman Expansion
CZL	Cohesive Zone Length
CZM	Cohesive Zone Model
DIC	Digital Image Correlation
ERR	Energy Release Rate
FEM	Finite Element Method
FML	Fiber Metal Laminate
HTCL	Hybrid Titanium Composite Laminate
MVC	Metal Volume Content
TZ	Transition Zone
UD	Uni-directional
VCCT	Vrtual Crack Closure Technique

1 Introduction

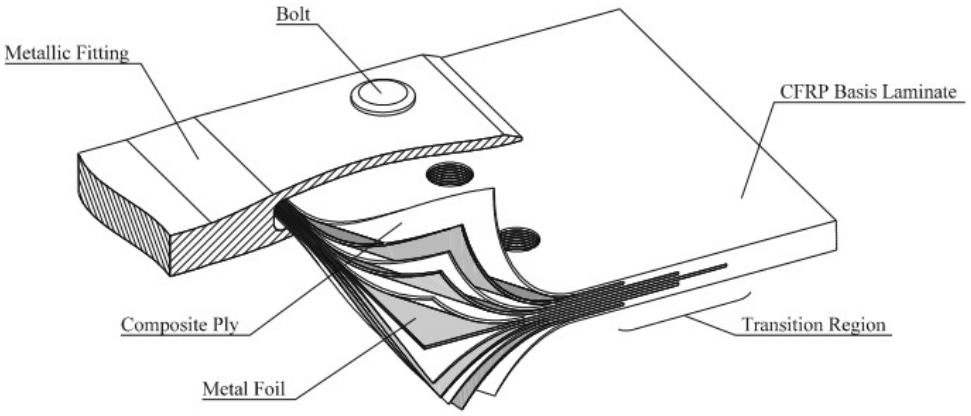

Figure 1.1: TZ in a CFRP bolted laminate [21]

The mass commercialization of civil aviation throughout the 1990s and predictions of tripling numbers of passengers in the next 20 years [77] pushed major aircraft manufacturers to develop larger aircraft. The increase was initiated and responded to by the development of wide body aircraft [77]. The fuselage diameter thus increased, as did cabin pressures, both leading to higher stressed structures [78]. For more people to fly in more heavily loaded aircraft, the structural demands increased. Furthermore Airbus planned to introduce the A380 to compete with the dominant Boeing 747. Their plans aimed to reduce the operating costs to a minimum of 15% less than of the B747-400 [65]. The contrary demands of increased capacity and safety at reduced costs called for new technological advancements. Composites alone suffer poor impact resistance, while aluminum alloys have low fatigue strength. These became the motivations for the initial developments of pioneering fiber metal laminate (FML) materials.

1.1. Challenges of Joining in CFRP

The assembly of aircraft rests on the reliable joining of individual structures. Even though adhesive joining has gained much attention in the last decade, the majority of joints are still utilizing riveting and bolting techniques. The associated notching of the structure carries the clear disadvantage of creating stress concentrations in a notch sensitive material. The design practice using purely composite materials utilizes some compensatory techniques for dealing with this weakness. These can be in the forms of metallic inserts [11, 58], z-pinns [41], local thickening of the laminate or increasing the numbers of fasteners, all of which will contribute to increasing the mass of the joint [20].

Many investigations were done with findings confirming the hypothesis that the addition of metallic layers increases the bearing strength and fatigue life of both continuous and notched laminates [2].

Lamination of composites and metals also carries some challenges, such as achieving good bond strength and preventing premature delamination. Overcoming these, hybridization can be used to avoid the need for any further compensatory techniques. Initially the majority of literature focused on the analysis of Glare. Since its introduction it was, and arguably still is, the most successful and proven hybrid material around. The titanium/carbon fiber reinforced polymer (CFRP) combination has also been the focus of many studies [12, 19, 21]. Only until the 2010s though has real attention been given to steel/CFRP hybridization, among other in local hybridization applications. The unique advantage of the high strength of steel made it another interesting hybrid candidate.

A distinction is made between cases of global and local hybridization. Global hybridization is understood as a a practice where metallic lamina are added to the composite lamina in the whole of the structure. Both material layers are thus continuous. The technology of local hybridization was patented in 2000 by Kolesnikov [38]. In this case the metallic lamina substitute the fibers in a discrete area. The fibrous laminae are interrupted and are substituted by equally thick metallic laminae in the hybridization zone. This means that there is a transition zone (TZ) between the sections of the fully composite and hybridized structure, as illustrated in figure 1.1. Both hybridization practices increase the bearing strength of the material, however hybridizing only locally increases the potential for weight savings. The importance of the transition zone design was demonstrated in literature and is also a topic of this thesis.

1.2. Scope and Aims

The present thesis project focuses on the unaddressed area of TZ design. The design of the TZ has been shown to have an effect on the joint performance, but limited literature exists on the methodology used to numerically characterize the behavior in the TZ as influenced by varying the TZ design. The aim of this project is to develop this methodology. A complex combined tensile/bending load case is adopted from an industrial application of the design of a wing root connection. A prerequisite goal to creating a numerical model analysis tool is the design and conduction of tests, which can be used for validation. Such a model can then be generalized to further applications, also under single load cases, where local hybridization is employed and a TZ design is required.

- Section 2.1 looks at the history of FMLs and the developments resulting in advantages over pure composites. Which materials and material combinations have been investigated in the past, and which are the materials most suitable for local hybridization.
- Section 2.2 focuses on the failure in composites and the criteria used to predict it. Which failure types can be expected in FMLs, and what are the suitable failure criteria for complexly predicting FML failure, recognizing interaction between fiber and matrix failure and different failure modes.
- Chapter 3 contains a review of the current literature relevant to TZ design. What the existing

TZ guidelines are and what the dominating failure type is for specific load cases. A description of the design of the combined loading testing method follows. This includes the tooling design, specimen design and manufacturing and methods used for experimental measurement of specimen strain.

- Chapter 4 focuses on the numerical simulation of the experimental setup described in chapter 3. The numerical methods which are available and finally employed for simulating both inter- and intralaminar failure in FMLs are described. Some benchmark simulations are discussed, which serve to validate the modelling choices and parameters.
- The Results and Discussion chapter 5 presents the experimental and numerical results. The suitability of the experiment to emulate the load case is discussed, as is the correlatory and predictive behavior of the model. The failure modes observed by microscopy are compared to the failure indices obtained from the model. The performance of individual TZ arrangements is judged based on these observations.
- The conclusions drawn from the results chapter are summarized in chapter 6. Some recommendations are given for future improvements to the experimental and numerical methods.

2

Project Background

2.1. Technological Background

The purpose of this chapter is to set up a context of wider theory for the specific thesis topic. Its aim is to give the reader the background knowledge about FMLs, failure and project specifics, based on which the methodology and discussion of the results are founded.

2.1.1. History of Fiber Metal Laminates

Aramid Fiber Reinforced Polymer / Aluminum Laminates

FMLs have been around since the early 1980s. The first commercialized and structurally applied material ARALL was developed at the Technische Universiteit Delft (TUD) and later manufactured by the Aluminum Company of America (Alcoa). The aramid fiber and aluminum 7075 laminate was developed for the lower wing skin of the Fokker F27 and F50 and later used in the Boeing C-17 cargo door [2]. ARALL showed unfavorable characteristics, such as low fatigue resistance or corrosion resistance of the aluminum. Besides, aramid fibers form weak bonds with the adhesive and it is therefore difficult to manufacture laminates with a fiber volume fraction of more than 50% with the required mechanical properties [5].

Carbon Fiber Reinforced Polymer / Aluminum Laminates

An attempt at improving the performance was made by replacing aramid fibers with carbon fibers to make CARALL. Unlike aramid or glass fiber aluminum hybrids, where aluminum is hybridized with less stiff materials, CARALL has the potential to outperform monolithic aluminum in stiffness and fatigue strength by the addition of stiffer and stronger fibers. The most significant resistance to the success of this combination was the galvanic corrosion of the aluminum lamina. This remains a challenge to the present day and the literature on successful developments is scarce. Some attempts have been made in recent years which underline the issue. Marzuki [44] attempted to anodize aluminum plies with phosphoric acid for hybridization with CFRP. The process of anodizing with the use of acid roughens the aluminum surface. This increases the wettability and within a certain roughness range can be advantageous for the interlocking of the metal – composite interfaces. Below this range wettability is insufficient and above it microscopic voids will form at the interface. In study by Wang [80] sulfuric acid was used for anodizing, followed by a nano-particle reinforced hybrid sol-gel coating. Even Wang observed signs of corrosion and results of his interlaminar shear strength tests were scattered and inconsistent.

Neither study tested the durability of the material. It is suspect that methods for protection

against galvanic corrosion are not controllable and therefore repeatable enough. Resulting pockets of aluminum oxide layers from inadequate protection at the interfaces would be detrimental for the fatigue life of any structure. Ensuring separation of the carbon and aluminum layers with glass fiber plies or polymeric coatings is possible, but only good until such laminates are drilled, which locally disrupts the protection. Possibly in low volume and highly controlled environment production, such as in the space sector, the surface treatment methods might be applicable. Otherwise the negative findings suggest that some technological advancements are still due before aluminum and carbon fiber can be coupled in a hybrid material of commercial aerospace grade quality.

Glass Fiber Reinforced Aluminum

TUD further lead the research to develop a glass reinforced aluminum laminate labeled GLARE, which was patented in 1987. In 1991 the Dutch company Akzo and Alcoa cooperated in producing Glare commercially. There have been ambiguities in the past regarding the specific material definition of Glare. Simply as a label, Glare can be the combination of a range of fiber, matrix and aluminum materials. Such a label is analogous to lumping all grades and alloys of steel simply under "steel". Glare is produced in 6 available variants with differing aluminum grades and prepreg fiber orientations [65]. Depending on the combination, each variant has distinctive characteristics and is therefore suitable for different applications [8]. These recognized grades are manufactured using S2-glass fibers in an FM94 matrix reinforced with 2024-T3 aluminum. Variants with high static strength utilize 7475t-761 and FM906 epoxy instead [2]. Since its commercialization, Glare has found applications throughout the aerospace sector. Most notably over $380 m^2$ of Glare is used in the Airbus A380 fuselage and more in the D-noses of the horizontal and vertical tailplanes, as well as the front empanage [22], or in the cargo door of the Boeing 777 [65]. It has also been used in smaller volume production aircraft such as the front radome bulkhead of the Learjet45 [61].

Titanium/CFRP

The first experiments testing the performance of hybrid titanium composite laminates (HTCL)s were carried out simultaneously at NASA and TUD. In attempts to develop heat resistant materials for high speed aircraft, Miller [49] built on the research of Kaufman [35], who showed that the fracture toughness of adhesively laminated aluminum plies was improved in comparison to that of an equivalent monolithic plate. Medenblik [46] carried out parallel experiments at TU Delft with laminated plies of TI-6Al-4V titanium and carbon fiber prepreg. They did not observe improvements to the laminate strength compared to monolithic titanium. On the contrary, strength in the transverse direction was less. They were among the first though to demonstrate the increase in fatigue life. Miller [49] followed up with a more in depth study considering factors affecting the material performance such as fiber material, volume fraction or orientation. They observed laminates with boron fibers exceeding the modulus values of those with intermediate modulus carbon fibers. And even though the strain to failure of the boron fibers was less, the ultimate strength of the two laminates was essentially the same. Other research into metal-fiber hybridization using boron fibers is limited. Except posing an increased health risk, the major reason for limited use of boron fibers, especially in civil aviation, is the high material price. The technology of local hybridization was already patented in the year 2000. However, pioneering studies of numerical methods for predicting

properties of locally reinforced HTCL laminates were carried out much later by Hundley [32] in the United States and Camanho et al. [12] in 2009.

2.1.2. Mechanical Properties of FMLs

There is a predominant focus in this section on the properties of FMLs in joining. It is essential to have knowledge about the bearing behavior, also for the purpose of good TZ design. There is a substantial benefit in using local hybridization in joints, precisely for the reason of improved bearing properties. There is a possible interaction of the bearing stress field with the stress concentrations at the APs in the TZ, which is discussed later.

GLARE

Mechanical joints using bolts or rivets are potential weak points in a structure since holes in the laminates create areas of high localized stress. The design of the geometrical parameters of a joint is one of the factors affecting its performance. As described in chapter 2.2, there are several possible failure modes that occur depending on the design of the joint. The study of these parameters specific to GLARE, but generalized to other FMLs has been the focus of many studies [48, 76, 81]. Generally finding, that compared to fiber-epoxy laminates, the laminate width to hole diameter (W/D) ratio required to avoid unwanted failure modes is less due to the increased bearing strength achieved by the inclusion of metallic lamina. Furthermore there is a difference between the bearing strengths observed in pin and bolted joint tensile and compressive tests. Pin-loading being more critical, since there is no lateral restraint which otherwise retards delamination. Frizzell et al. [22] performed pin-bearing tests in Glare 3 3/2 0.4 L specimens, the same grade used in the top of the fuselage of the A380. The W/D and edge distance to diameter (E/D) ratios were designed to promote either bearing, shear-out and net-tension failure. A very low E/D ratio of 1.3 was used to achieve shear-out failure and a W/D ratio of 2 for net-tension. Frizzell did not report on the minimum ratios required to induce bearing failure. The joints designed to fail in bearing used both ratios of 6 and showed the highest failure load, followed by the shear-out and net-tension specimens. Slagter and Wu [66] concluded form their study that minimum E/D and W/D should be a minimum of 3 and 4 respectively. In comparison with other authors this is quite conservative. Meola et al. [48] showed that W/D ratios of 2 were sufficient to achieve maximum bearing strength. Van Rooijen [75] concluded the minimum E/D ratio should be greater than 2.5.

The final failure in Glare specimens observed in the study done by Frizzell et al. [22] was due to a combination of plastic deformation of the metallic layers, delamination, fiber buckling and fracture. The researchers made micrograph observations of glass fibers protruding out from between the aluminum layers. The possible explanation is an elastic springback of the fibers separating themselves from plastically deformed aluminum. There is a bilinear stress strain relationship in Glare due to the interaction between the aluminum and composite layers. Additionally, the combination of materials dissimilar in mechanical properties leads to increased interlaminar stresses. A further concern are the residual stresses from manufacturing due to the different coefficients of thermal expansion (CTE). This issue has been studied in Glare [1] and has not been found to be a limitation to using Glare in certified structures. However it continues to be a topic in FMLs with more severe CTE

contrasts, such as HTCL and steel/CFRP laminates [32].

Titanium/CFRP

Graphite has a negative CTE. Compared to other aerospace metals, titanium has a relatively low CTE and is electrochemically compatible with CFRP. It also matches CFRP in it's low yield elongation, which makes it a good candidate for CFRP hybridization. Nevertheless decreased delamination resistance between metallic and composite layers is still observed. Kolesnikov et al. [39] did a series of tests on Titanium/CFRP globally reinforced laminates including impact testing. Their study on the effect of environmental conditioning reported similar absolute interlaminar shear strengths and degradation rates for the hybrid and fully composite laminates. Though the extent of delamination damage was larger than in the reference pure CFRP laminate, with a tendency toward a reduction in the extent of damage with increasing metal content.

The specific joint performance is influenced by the titanium content, which in turn depends on the number of bolt rows and type of loading. This makes optimized design of hybrid joints a complex task. Kolesnikov et al. [39] were able to demonstrate the improvement in joint efficiency even with sub optimal design parameters. That is using only unidirectional carbon plies in a $[0_4/Ti]_s$ layup, compared to a [50/40/10] CFRP laminate. The largest performance contribution was in the case of 90° off-axis loading where gains up to 41.5% were observed. Also in dynamic MINITWIST fatigue tests to simulate aircraft wing behaviour specimens reached numbers of cycles 5 times the A-320 aircraft life. The performance improvements were achieved with plies of single orientation. There is potential for further improvements through work on the stack orientations and sequence and the design of the transition zone.

Since joints are mostly designed to fail in bearing, much of literature on the topic of local metal hybridization applicable to joints focuses on the bearing strength. As part of the *Increase of Bolted Joint Performace for CFRP (BOJO)* project, Camanho et al. [12] and Fink et al. [21] tested locally reinforced joints with varying titanium content. The layup was kept constant, with only uni-directional (UD) plies. They noted more pronounced linear behaviour with increasing metal content. Improvements in ultimate bearing strength up to 153% were observed. In line with Kolesnikov's findings Kolesnikov et al. [39], the interlaminar fracture toughness in all three modes stayed within 5% of the reference CFRP laminate. Figure 2.1 from Fink [19] illustrates the relation between titanium content and absolute bearing strength. The highest strength of the reference CFRP laminate was surpassed at 20% MVC. A more useful measure of assessing the weight efficiency is the specific strength, plotted in figure 2.2, for which there was an increase of 29% at 50% titanium content. Camanho et al. [12] were also able to achieve a good numerical correlation for their bearing tests, exemplifying the ability to simulate damage in hybrid models. Camanho and Fink were able to apply the findings from their research and demonstrate the feasibility of integrating the technology in a complex structure in an industrial application of an Vega payload adapter re-design.

Steel/CFRP

Reinforcing composite laminates with metallic laminae has been shown to improve the mechanical properties of the laminate. However in the case of absolute bearing strength, the hybridized solution is still outperformed by the fully metallic design. Van Rooijen [75] experimented with the local

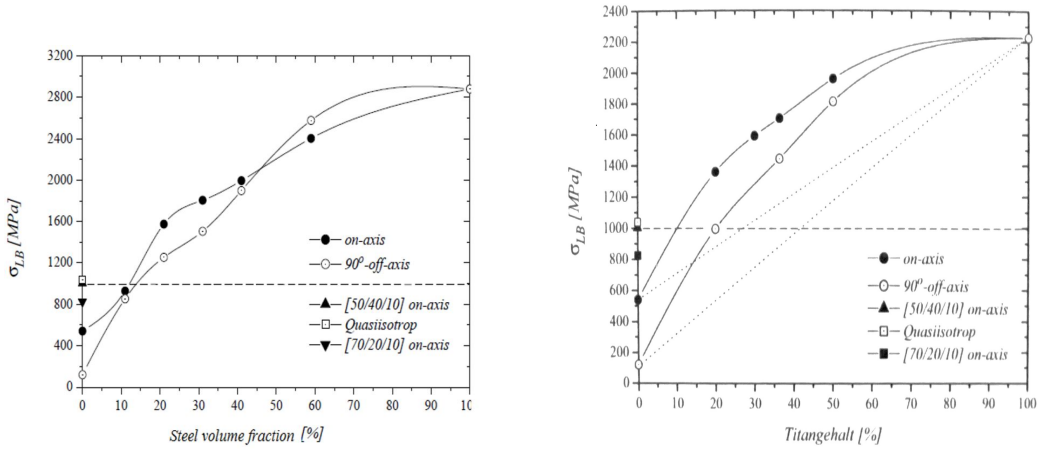

(a) Absolute bearing strength steel/CFRP laminate

(b) Absolute bearing strength HTCL laminate

Figure 2.1: Absolute bearing strengths of Steel/CFRP and HTCL laminates with varying metal content.[19]

addition of steel layers to Glare laminates. The idea being that the higher bearing strength of steel can push the strength of the hybrid above a purely aluminum design. The result was a small increase in the specific bearing yield strength with almost no effect on the specific ultimate bearing strength. The discussion with respect to specific strengths however overlooks some secondary aspects. In this case the same strength increase could have been achieved by the addition of aluminum layers. This would have resulted in a local thickening of the laminate, increasing the eccentricity. This would in turn have a negative effect on the fatigue behaviour.

The CTE of steel is 17 $\cdot 10^{-6}/K$ slightly higher than 8.6 $\cdot 10^{-6}/K$ of titanium. Consequently the resulting residual stresses are also higher. Prussak et al. [59] devised alterations to the laminate autoclave curing process for reducing the thermal residual stresses in three distinct methods. The first was to mechanically force elongation of the CFRP layer to match the thermal elongation of the steel layer. Secondly the lateral pressure was increased via a stiff coverplate on top of the laminate. Lastly the cure cycle temperature profile was modified to cool the autoclave back to room temperature as the curing process initiates with the aim of lowering the bonding temperature. Full solidification is then achieved upon again raising the autoclave temperature. The most effective method for lowering the residual stress was mechanical clamping with a reduction of up to 65%. Increasing the pressure and modifying the temperature resulted in 33% and 21% reductions in residual stress. The reductions in residual stress translated to increased tensile strength by up to 3.3%. The experiments were performed with specimens of 65% MVC. According to the authors the residual stresses in high MVC laminates are less severe, and therefore lower MVC laminates can draw even larger benefits from the investigated methods.

Fink et al. [21] also point out these secondary effects when comparing hybrid solutions to the composite laminates. Looking at figure 2.2, it is clear that the specific strengths of pure composite laminates cannot be achieved with hybrids. The maximum on-axis 0° specific bearing strengths of steel and titanium FMLs are approximately 550 and 600 $MPa\frac{cm^3}{g}cm^3$ at 20% and 50% metal volume content (MVC) respectively, compared to around 650 $MPa\frac{cm^3}{g}cm^3$ in the reference (quasiisotropic)

laminate. Now reading the absolute bearing strengths of the hybridized laminates at the metal volume percentages from figure 2.1, the values are 60% and 90% higher for steel and titanium. Consequently there are secondary weight saving potentials to the hybridization which are a result of this absolute strength increase, namely in the reduction in the amount of fasteners, secondary fittings or by overlap shortening. Fink [19] reports the minimum W/D ratio to achieve full bearing strength in steel/CFRP hybrids to be 2.9. Surprisingly, his reported minimum W/D ratio for HTCLs is lower - 2.2.

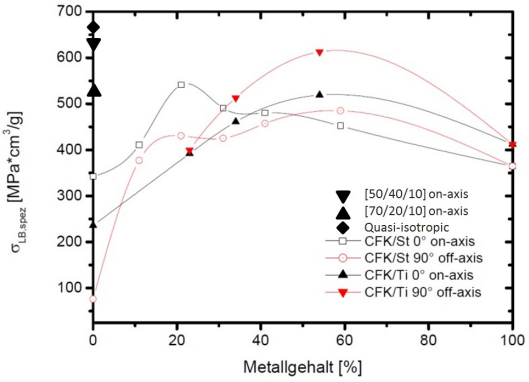

Figure 2.2: Comparison of specific bearing strength in HTCL and steel/CFRP laminates [19]

An advantage in using steel for local reinforcement is that due to it's high absolute strength and modulus, the layers needed to achieve the desired increase in bearing strength are thinner compared to titanium. Figure 2.2 shows that at low metal content up to approximately 25%, steel even outperforms titanium in specific bearing strength in both on and off axis loading. There are manufacturing constraints on the minimum thickness of steel sheets though. It is possible to manufacture sheets as thin as 0.025 mm. However using plies with such low thickness poses difficulties with handling. Additionally the surface treatment required for good adhesion involves a grit-blasting step, which can pose a risk of damaging the sheets or inhomogeneous work hardening for thicknesses below 0.08 mm [68].

Furthermore, the thickness of a layer in a laminate must be continuous. Metallic plies will therefore rarely have to be thinner than a unidirectional (UD) prepreg layer. That said, UD prepregs are available in ply thicknesses in the order of hundreds of milimeters. In most (aerospace) applications, the thinnest ply thickness will be around 0.1 mm. Buczynski [9] performed bearing tests on steel hybrid specimens using 0.1 mm steel plies and specimens with two steel plies bonded together, effectively resulting in 0.2 mm steel lamina. In both types of laminates he observed buckling of the steel layers. Within this range of thickness there was effect of thickness on strength. The MVC is ultimately determined by the necessary bearing strength [56]. The choice of material can then be dependent on the specific strength requirements, with steel and titanium being more suitable for lower and higher MVC respectively. Aluminum has been mostly excluded from CFRP hybridization due to the reasons given in section 2.1.1. The discussion of choice between titanium and steel is to some extent qualitative and rests on several trade offs. What remains clear is that the specific strength is not the only indication of the weight efficiency of a hybrid.

2.2. Failure Types in Unidirectional Composites and FMLs

Failure in conventional thermosetting composite materials is classified between intra-laminar and inter-laminar failure. There is little plasticity in the fiber or matrix, therefore these failures often occur in a brittle manner. In the case of FMLs, the behavior under tensile loading is inelastic due to the plasticity of the metallic layers [67]. Intralaminar plastic failure can be observed in the metallic layers or in the case of lamina with a thermoplastic matrix.

2.2.1. Intralaminar Failure

Figure 2.3 illustrates the possible intralaminar failure mechanisms. Generally they are in two classes; fiber and matrix fracture. There are often interactions between intralaminar and interlaminar failures. Namely, points of intralaminar failure serve as points for interlaminar failure initiation. Such behavior is specifically relevant to FMLs, where intraply failure will happen in the composite layer before plastic fracture in the metallic ply can occur.

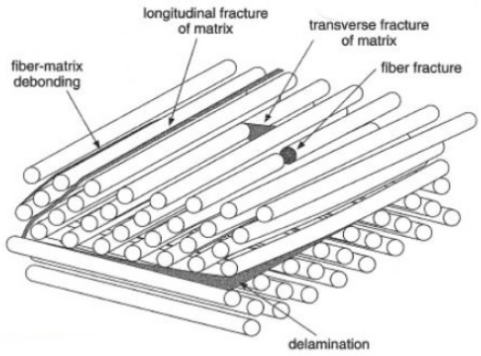

Figure 2.3: Failure modes in composites

Tensile Failure

Fiber strength in a composite follows a statistical distribution. Fibers have varying amounts of defects which can cause some to fail earlier than others. The failure to strain of the matrix is generally higher than that of the fiber. Therefore the first event in tensile failure of a 0° UD material is fiber failure. The stress is redistributed in the unbroken fibers, while the void created by the broken fiber acts as a stress concentration in the matrix. Figure 2.4 illustrates the possibilities for the ensuing microfailure modes [42].

(a) Shear stresses at the fiber ends cause debonding of the fiber from the matrix. The load carrying capacity is reduced over the critical length required to load the fiber through shear with the matrix.

(b) Matrix cracking occurs as a result of the void stress concentration

(c) increased average loading per fiber and stress concentrations cause further fiber breakage, creating a chain reaction of failures.

Cracks can coalesce to form a crack which continues to progress through the lamina. Breaks in defected fibers can occur ahead of the advancing crack tip but outside of it's plane. This effect is called fiber bridging and has also been observed in FMLs. The bridging of microcracks is a significant contribution to the material toughness.

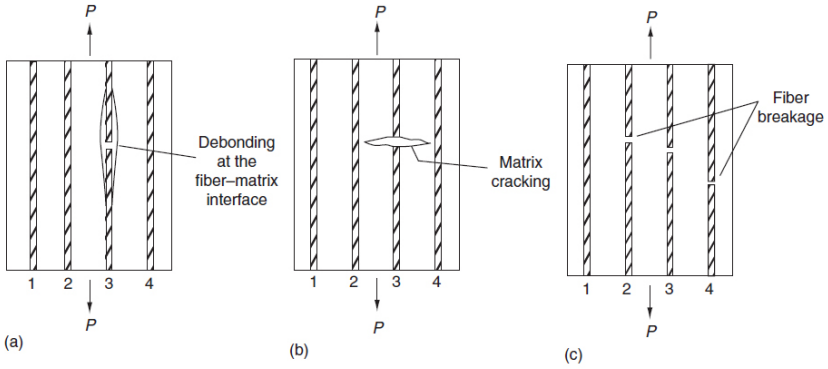

Figure 2.4: Microfailure modes under tensile loading [42]

Compressive Failure

Without the lateral support of the matrix all fibers would fail by buckling. In a laminate the failure in fibers depends on their internal structure. The types of failure modes observed in the fibers and matrix independently, as well as when forming a composite, are illustrated by Figure 2.5. Graphite fibers fracture under compression in shear along a plane of maximum shear [23]. The higher modulus of graphite fibers is due to the alignment of the crystalline structure along the length of the fiber. Shear failure and kinking is typical for fibers with such a crystalline structure with weak radial bonds. Aramid fibers also share these structural properties, however tend to fail in the kink mode. The difference is in the low failure strain of the graphite fibers which leads to fracture [13]. Brittle fibers with amorphous structures, such as glass fibers, tend to fail in bending with cracks being initiated at the tensioned side. Compression of ductile resins leads to plastic flow at 45° to the loading direction. Brittle resins exhibit shear band formation before ultimate failure [23].

The discussion of intralaminar failure is limited to unidirectional composites. The three common failure modes are shown in Figure 2.5. The most likely failure mode to occur in CFRP composites is shear crippling caused by fiber kinking, where fiber breaks are usually observed at kink band boundaries, as can be seen in micrograph c of figure 2.6 [18]. In uniaxial compression misaligned fibers will initiate the kinking process, disrupting the stability of the neighboring fibers. This process will propagate through the laminate until failure. The interaction of two kink bands with sufficiently high transverse tensile stresses can cause longitudinal splitting. This interaction is visible in micrographs b and d of figure 2.6. Longitudinal splitting can be the precursor to delamination and can also be caused by the relatively low strength of the matrix and fiber-matrix interface compared to fiber strength. The difference in Poisson's ratio between the matrix and fibers causes transverse stresses to develop in the matrix. Voids can then act as stress concentrations to initiate fracture along the fiber direction [23].

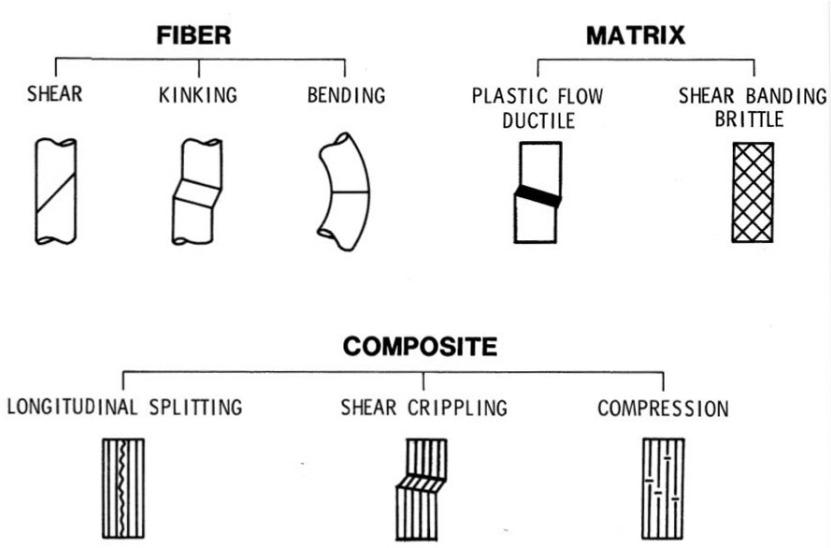

Figure 2.5: Common failure modes in fibers and matrix alone, and in UD composites[23]

2.2.2. Interlaminar Failure

Interlaminar failure is a debonding of the individual plies constituting the laminate. Delamination is then a type of matrix failure caused by crack nucleation and growth. The delamination can be initiated by impact, otherwise it generally starts at the free edges of the laminate. The discontinuous change of elastic properties give rise to shear stresses, with the free edges of holes being especially sensitive to delamination formation. Higher interlaminar stresses may arise due to large stiffness or orientation steps between neighbouring plies. Depending on the type of loading, the crack can grow in three types of modes. These are illustrated by figure 2.7 and are:

- Mode I, the most common opening mode caused by tensile loading normal to the plane of the crack.
- Mode II, the shearing mode which is driven by out of plane shear stresses applied normal to the crack edge.
- Mode III is the tearing mode driven by out of plane shear stresses applied parallel to the crack edge.

The metal interfaces in FMLs are just as sensitive to the free edge effect and serve as crack nucleation points for delamination. As stated by Marannano and Pasta [43], the onset of defects is then particularly common at the interfaces between metallic and composite plies. The delamination behavior is influenced by the material's fracture toughness properties, which is described by the critical energy release rate (ERR). Though Marannano and Pasta did not cite any concrete results, they found a good correlation between the individual analytical, numerical and experimental procedures for testing mixed mode (I and II) behaviour in FMLS. Petersen and Hühne [54] obtained experimental ERR values for steel-CFRP and CFRP-CFRP interfaces at various orientations. These are presented in table 4.1 and clearly show that ERR values for steel interfaces are lower compared to purely CFRP interfaces. Such a qualitative comparison indeed supports the hypothesis that, at least

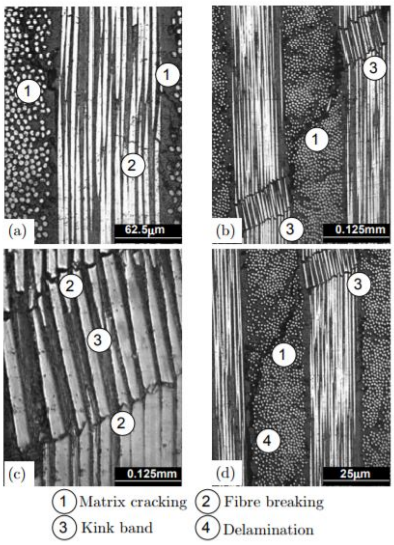

Figure 2.6: Micrographs illustrating failure modes in UD composites[57]

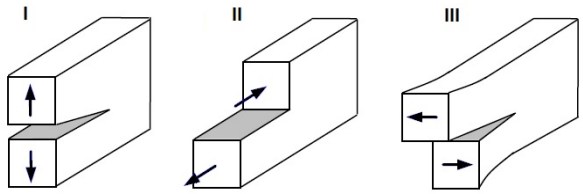

Figure 2.7: Crack growth modes: I Opening II Shearing III Tearing

for the specific case of steel and CFRP, the metallic interfaces are more susceptible to delamination. Khan et al. [36] looked at the delamination growth under cyclic loading. Here the authors were able to show that the cyclic load transfer at the fiber-metal interface causes shear stresses, resulting in delamination growth in the wake of the crack. The authors showed that delamination behavior was independent of applied load sequences, unlike the behavior observed in metals.

2.3. Failure in joining

The efficient design of joints is critical for the overall load carrying capability of the structure. Two important ratios E/D and W/D as illustrated by figure 2.8. In multibolt joints the spacing between holes also plays a key role. These ratios are detrimental to the expected failure mode. Figure 2.8 illustrates the different possible failure modes in composite laminates. The recommended design ratios are determined through bearing tests on the laminate in question. It is desirable that the joint fails by bearing failure rather than net tension or shear-out, as this can be better detected before complete failure of the joint. The geometrical ratios to avoid these modes will clearly differ depending on the laminate material and layup. Generally for purely fibrous laminates the shear-out resistance does not change beyond a certain E/D ratio [25], with minimum ratios around $E/D > 3$ and $W/D > 6$ [42]. For FMLs the required W/D ratio is less $W/D > 4$ [22].

For joints designed to fail in bearing, the most influential property is the bearing strength. This

is defined as the maximum contact pressure between two bodies (in this case the bolt and laminate). The bearing strength will also depend on the type of joint. The clamping force of a bolt can resist delamination growth and thereby increase the bearing strength by more than 20% [81]. The arrangement of bolts will also affect the load distribution and location of the final failure. Hart-Smith [25] make the point that to slightly reduce the bearing stresses requires a more complex stepped-lap joint. Just adding more rows of fasteners with uniformly thick members bolted together does not reduce the load on the end fasteners where final failure would occur. Herein lies the advantage of using metal hybridization - in increasing the bearing strength through the material and avoiding adding fasteners for which the added complexity of stepped thicknening is required.

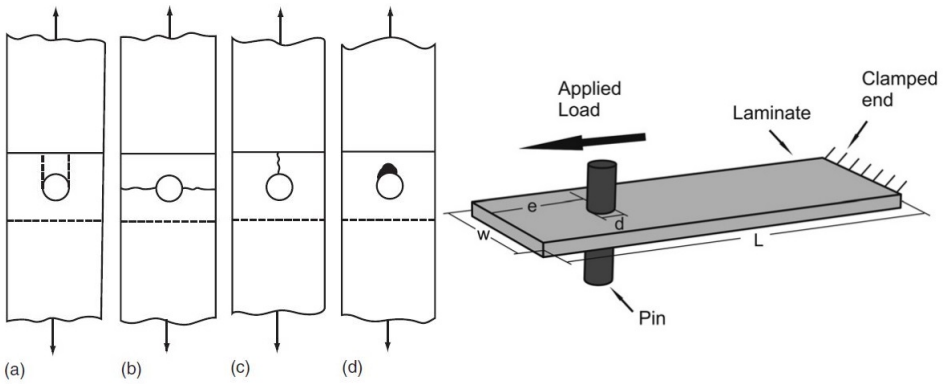

Figure 2.8: Failure modes in bolted laminates: (a) shear-out (b) net tension failure (c) cleavage (d) bearing failure. Combinations of failures modes are also possible [42]
Pin bearing test setup with ratios dimensions labels[22]

2.4. Failure Criteria

Many failure criteria exist and the failure predictions depend on the criterion used. The simplest of these criteria are the maximum stress and strain criteria. The maximum stress criterion relies on the principle that every ply will fail if the stress exceeds its corresponding strength. The maximum strain criteria is analogous in comparing strain values. The predictions for these two theories are similar for fiber orientations close to 0°. Knock-down factors can be used to account for imperfections in the plies or for environmental factors. The theories are simple to apply, however there is no account for the interaction of stresses (or strains). As a result, the laminate might fail in reality, even if the ply stress/strain is still under the failure limit. In some specific types of interactions, the criteria can on the other hand be conservative. The notation throughout this chapter which refers to the allowable stresses along and transverse to the fiber direction in tension and compression respectively is X^t, X^c, and Y^t, Y^c. The ply stresses are σ_x and σ_y, with shear stress and allowable annotated by τ_{xy} and S_12. Hill [29] proposed one of the first combined failure criteria based on the von Mises criterion for metals:

$$\left(\frac{\sigma_x}{X^{t,c}}\right)^2 + \frac{\sigma_x \sigma_y}{(X^{t,c})^2} + \left(\frac{\sigma_y}{Y^{t,c}}\right)^2 + \left(\frac{\tau_{xy}}{S_{12}}\right)^2 \geq 1 \tag{2.1}$$

The stress components are compared with their allowables, allowing for stress interaction by the

addition of individual stress contributions. Failure would occur if the value of the left hand side of the equation becomes greater or equal to one. The criterion of Tsai and Wu [71] built on the theory of Hill:

$$\frac{\sigma_y^2}{X^t X^c} + \frac{\sigma_y^2}{Y^t Y^c} - \sqrt{\frac{1}{Y^t Y^c}\frac{1}{X^t X^c}}\sigma_x\sigma_y + \left(\frac{1}{X^t} - \frac{1}{X^c}\right)\sigma_x + \left(\frac{1}{Y^t} - \frac{1}{Y^c}\right)\sigma_y + \frac{\tau_{xy}^2}{S_{12}^2} \geq 1 \tag{2.2}$$

The intention of Tsai and Wu was to mathematically generalize Hill's theory and account for the different strengths of composites in tension and compression. This theory and others such as that of Puck [16] or Hashin [26] attempts to capture the failure behavior of homogenized material, hence omitting the micro-mechanical mechanisms. There are a number of parameters to be experimentally determined as input for the model.

Cuntze criterion

The Cuntze criterion [14, 15] was validated by the World Wide Failure Exercise (WWFE). It draws many simmilarities from Puck, and identifies the same failure modes. It is based on the application of the Failure Mode Concept (FMC). This approach focuses primarily on the failure modes and then on the interaction of stresses within a mode [14]. Each mode corresponds to an independent failure mechanism and each mechanism is represented by one failure condition. Cuntze identified 5 failure modes shown in figure 2.9. The corresponding failure conditions are given by equation 2.3. Where in the case of FF1 and FF2 $\sigma_1^* = \sigma_{1f} V_f$. With σ_{1f} being the stress in the fibers, fiber failure can be approximated by $\sigma_1^* = \epsilon \cdot E_{||}^{t/c}$

$$\begin{aligned}
FF1 : Eff^{||\sigma} &= \sigma_1^* \Big/ R_{||}^t = \sigma_{eq}^{||\sigma} \Big/ R_{||}^t \\
FF2 : Eff^{||\tau} &= \sigma_1^* \Big/ R_{||}^c = \sigma_{eq}^{||\tau} \Big/ R_{||}^c \\
IFF1 : Eff^{\perp\sigma} &= \left[(\sigma_2 + \sigma_3) + \sqrt{(\sigma_2 - \sigma_3)^2 + 4\tau_{23}^2}\right] \Big/ 2R_\perp^t = \sigma_{eq}^{\perp\sigma} \Big/ R_\perp^t \\
IFF2 : Eff^{\perp\tau} &= \left[\left(\frac{1}{1-\mu_{\perp\perp}}\right) \cdot \sqrt{(\sigma_2 - \sigma_3) + 4\tau_{23}^2} + \frac{\mu_{\perp\perp}}{1-\mu_{\perp\perp}} \cdot (\sigma_2 - \sigma_3)^2\right] \Big/ R_\perp^c = \sigma_{eq}^{\perp\tau} \Big/ R_\perp^c \\
IFF3 : Eff^{\perp||} &= \left\{\left[2 \cdot \mu_{\perp||} \cdot I_{23-5} \sqrt{4 \cdot \mu_{\perp||}^2 \, I_{23-5}^2 + 4 \cdot R_{\perp||}^2 \cdot (\tau_{32}^2 + \tau_{21}^2)^2}\right] \Big/ (2 \cdot R_{\perp||}^3)\right\} = \sigma_{eq}^{\perp||} \Big/ R_{\perp||}
\end{aligned} \tag{2.3}$$

In equation 2.3 $R_{||/\perp}^{t/c}$ represent tensile and compressive strength of the fiber parallel and perpendicular to the fiber direction. The internal frictional values are defined by $\mu_{\perp\perp}$ $\mu_{\perp||}$. The invariant I_{23-5} and friction model parameters $b_{\perp\perp}$ $b_{\perp||}$ are defined by the following:

$$I_{23-5} = 2\sigma_2\tau_{21}^2 + 2\sigma_3\tau_{31}^2 + 4\tau_{23}\tau_{31}\tau_{21}$$

$$b_{\perp\perp} = \frac{1}{1-\mu_{\perp\perp}} \tag{2.4}$$

$$b_{\perp||} = 2\mu_{\perp||}$$

Each of Cuntze's five failure modes is characterized by one strength and one modulus. "The FF criteria are treated as decoupled from the IFF ones" [15], however the interaction of modes is expected and handled by an interaction factor used to numerically combine the failure modes [55]. This is a different approach to that of Puck, who argues that FF failures weaken the resistance against IFF and applies a weakening factor to account for this.

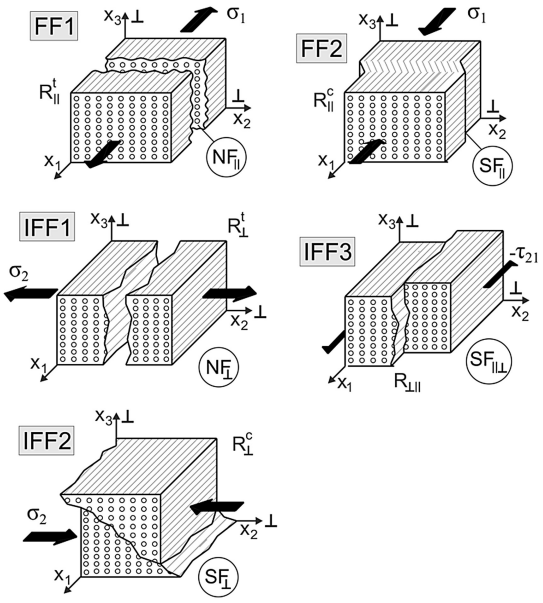

Figure 2.9: Tension and compression Fiber Failure (FF) and compression, tension and shear induced Inter Fiber Failure (IFF) modes[15]

As with the previous methods, there is a need to experimentally determine the parameters, namely a strength and modulus for each mode plus two Mohr-Coulomb friction property values. Petersen et al. [55] described the methods for experimentally determining these twelve properties, with a special focus on the friction values. The uniaxial strength and modulus values can be determined quite easily by statically loading 0° and 90° lamina. Petersen et al. used the ARCAN test to determine the shear strengths and friction values, but proposed that the IOSIPESCU test would be more applicable for determining strengths in an engineering environment due to its lower complexity. Hinton et al. [31] and Kaddour and Hinton [34] evaluated the predictive capabilities of the failure theories presented in the WWFE I and II. They evaluated the performance as "very good", as it provided a good fit with a large number of test data. They pointed out the dependence of the theory on a good characterization of the parameters described previously.

2.5. ATLAS Project Background

The context considered for the investigation of the TZ is the ATLAS (Advanced Technology Long-range Aircraft-concepts) project at DLR. The Department for Composite Design has developed an innovative design of a connection between the wing skin and center wing box. The design makes the use of FMLs, expecting to exploit their increased bearing properties, whereby reducing the structural weight. The design is considered at the concept level and detail designs of the joint are not available. The key data taken from the ATLAs project for the current project are the loading case and the base layup of the laminates, which are to be hybridized. The findings from this thesis project can be reintegrated back into the ATLAS project, as the design of the TZ is not influenced and itself does not influence the joint geometry, type of connection or it's construction.

2.5.1. Layup design

The base skin layup to be hybridized is taken from the design of a commercial, mostly composite, long range aircraft.

$$[45/90/\text{-}45/0_2/\text{-}45/90/45/0_4/45/90/\text{-}45/0_4/\text{-}45/45/0_4/45/0_3/\text{-}45/0_2]_s$$

The total thickness of the skin laminate is 16.256mm. The ratios of layers oriented by $(0/\pm 45/90)$ degrees are (59/32/9). The MVF is derived from the necessary bearing strength. Conventionally the laminate is locally thickened to increase the bearing strength. Instead, steel layers with higher bearing strength are substituted up to the point where the bearing strength of the overall laminate matches that of the original thickened section. From the ATLAS configuration, the minimum necessary MVF is 30%.

2.5.2. Loading Case

The purpose of selecting a combined loading scenario was to create a more inclusive and realistic study. There are often additional bending moments acting along the major tensile loads. Specimens with a TZ perform differently under pure tension or pure bending. Often designs that favor good performance under tension perform poorly under bending and vice versa. The design load case is dominated by in-plane tension with the ratio of tension to bending moment of approximately 0.01.

3

Experimental method

3.1. Previous Investigations of the Transition Zone

The study of the TZ became relevant with the advent of local hybridization at the hands of Kolesnikov et al. [39], who was one of the pioneers of local hybridization. The technique behind the initial designs of the TZ was to replace the least contributing plies first. Due to their lower load carrying capacities 90° and 45° plies were replaced leaving only 0° plies. If it was necessary to increase the metal content, 0° plies could also be interrupted for the laminate thickness to remain unchanged. As for the ordering of the transition zone, the plies were replaced in a staggered manner with little attention given to the separation distance.

Nekoshima et.al. [50] carried out a study to investigate the failure mechanisms at the transition zone of a HCTL. In their study titanium plies were added to the carbon fiber (CF) laminate, meaning that the CF plies remained continuous. They looked at a number of configurations with fixed metal content but varying separation distance and ordering. Petersen et al. [56] carried out a study with similar aims, where local areas of CFRP plies were interrupted and replaced with steel lamina in laminates loaded in tension or bending. The configurations under investigation are shown in figure 3.1. The locally hybridized specimens were compared with fully CFRP and a fully CFRP/steel hybrid laminates.

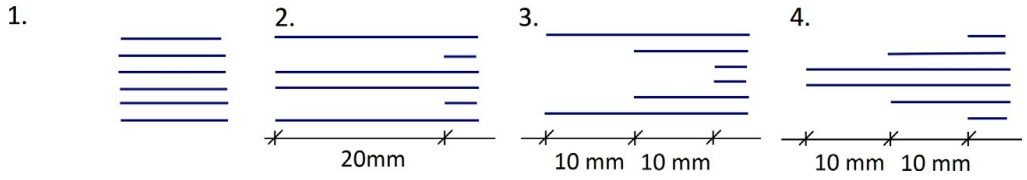

Figure 3.1: TZ arrangements investigated by Petersen et al. [56]

The quasi-isotropic and UD specimens with TZs did not show any plasticity under tensile loading, which is attributed by the authors to failure in the matrix and a resultant relaxation of stresses in the steel layers. With a quasi-isotropic layup, the full FML performed best in terms of absolute strength. It was followed by the reference CFRP laminate and lastly the locally hybridized laminates with specimen with TZ 1 performing worst. For a UD layup, the reference laminate showed highest strengths with the full FML and TZ specimens 2-4 at approximately the same strength, with TZ 1 again performing worst.

In the bending load case, the arrangement of the layers in the TZ is more influential on the strength. In the quasi-isotropic configuration, the strength of the reference laminate is on par with

the locally hybridized laminates. Specimens with TZ 2 and 3 had the highest strengths with quasi-isotropic layups, but quite the opposite was observed in the unidirectional specimens. The failure type in all combinations of layups and loading was predominantly delamination, but occuring at different layers.

The aforementioned studies considered various transition zone patterns, which were practically arbitrarily selected. They were informed by the logic described in the research by Kolesnikov et al. [39], however neither author designed a methodology to determine an optimum configuration. From the study of Petersen et al. [56] it is clear however, that the load carrying capacity of a locally hybridized laminate is dependent on many factors. Which include the layup, loading case and of the most relevance this thesis - the arrangement of the TZ itself.

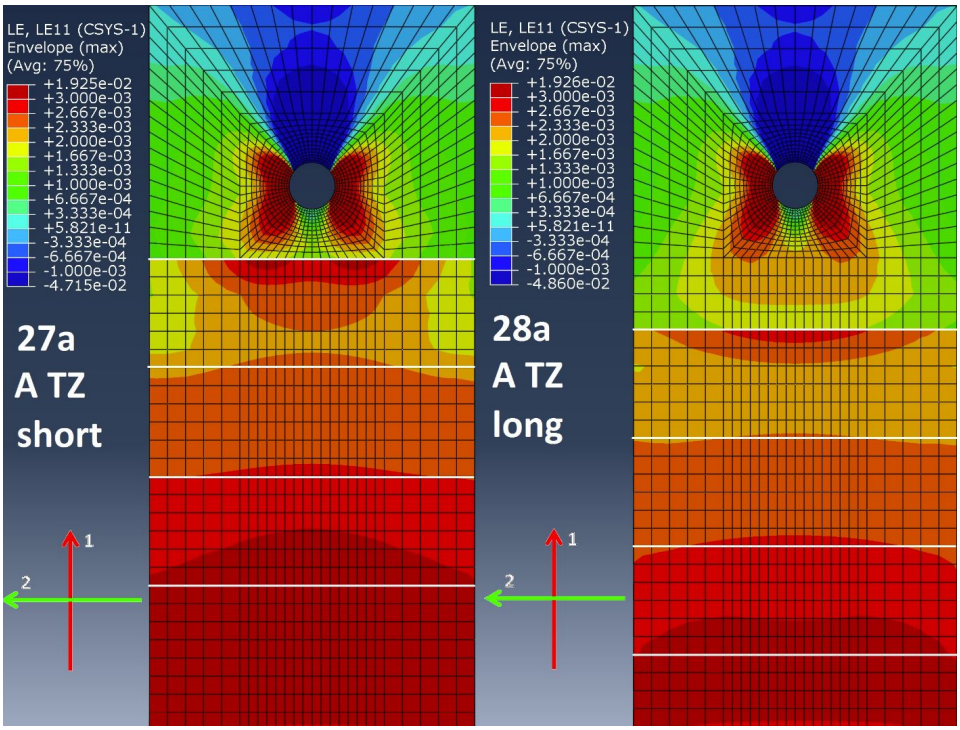

Figure 3.2: Strain field in the TZs of bearing loaded FML specimens [60]

Puzio [60] produced figure 3.2 using an experimentally verified FEM model. It illustrates the strain distribution in the longitudinal direction in the metallic ply around the hole and in the stepped substituted 90° CFRP plies in the TZ of bearing loaded FML specimens. The two models differ in the length of the metallic ply. The distance from the hole center to the first step is 10 mm and 20 mm in the left and right models respectively. The step distances between subsequent drop-off are 15 mm. The characteristic tensile strain butterfly shaped pattern is observed around the hole. With each metal ply drop-off the stiffness decreases resulting in a stepped increase in strain, expressed as color steps in the results visualization.

From the figure there are two observable strain effects. The strain field around the hole caused by bearing and a stiffness decrease due to step downs. Furthermore, there are local stress concentrations at the APs present in the specimen, as has been described previously. Clearly it should be a design aim to forego the superposition of these effects. Here the knowledge about bearing be-

haviour becomes important in the ability to predict the extent of the stress and strain field. In both cases in figure 3.2, the strain field decays rapidly to zero strain at the first ply drop. If the first drop off is closer to the hole, the stress flows through the transition into the neighbouring ply, resulting in a strain peak at that step. In the case where the first ply is longer, this effect is less significant. In the interest of minimizing the metal content and hence overall transition zone mass, the first drop-off should be as close to the hole as possible without the bearing strain field interacting with the first drop-off. Similarly, the subsequent drop offs should also be as close together as possible, but spaced so that there is no interaction between each other. A step distance of 15 mm is clearly sufficient to forego this effect in figure 3.2, however the exact spacing is expected to be dependent on the loading case and layup. The damage in Puzio's model was purely intralaminar, defined by a progressive damage model based on the Cuntze criterion. Without the inclusion of interlaminar failure in the model and being aware of the extent of the influence of delamination, the results are likely underestimating the TZ effects. The distances derived from this model should then be considered as a maximum, but extensions to the capabilities of the model are due before one could expect more conservative results.

3.2. Design of a Test for Combined Loading

The loading case of a wing root attachment joint, as described in the ATLAs project, is that of combined tensile and bending loading. Two types of test setup were considered for emulating the load case. The first method was used by Pellenkoft [53] to test Glare specimens in combined loading. The method exploits the otherwise undesirable effect of secondary bending in lap joints. The specimen for this method is prepared as a double lap joint, with the material being tested at the center and loaded by shear through the bonded overlap areas on each end. The maximum force that can be transferred into the specimen is determined by the shear strength of the adhesive. The advantage of this setup is that a conventional hydraulic grip system on a tensile testing machine can be used without any additional tooling. On the other hand, the quality of the test depends to a large extent on the quality of the preparation of the sample, which is itself more complex than a regular flat specimen.

The second possible setup is an adaptation of a test described in a NASA technical report [51]. A flat specimen is loaded in tension through a line offset to the centre-line of the specimen. The result is a bending moment in the specimen, which acts to deflect the center-line of the specimen to the line of loading. The condition for this moment is an enabled rotational degree of freedom at the ends of the specimen. Such a boundary condition calls for the design of special tooling. An example of such a fixture used in the aforementioned NASA report is shown in figure 3.3. The downside to this method is the need for additional tooling. However this is a one-time investment, which is traded off by the relative simplicity in specimen preparation. Furthermore, the load transfer into the specimen with this method is not limited by the strength of the adhesive. To reach ultimate failure in a reasonably sized CFRP specimen, the areas for shear load transfer would need to be excessively large. For this reason and other mentioned previously, the hinged tolling method was chosen and adapted.

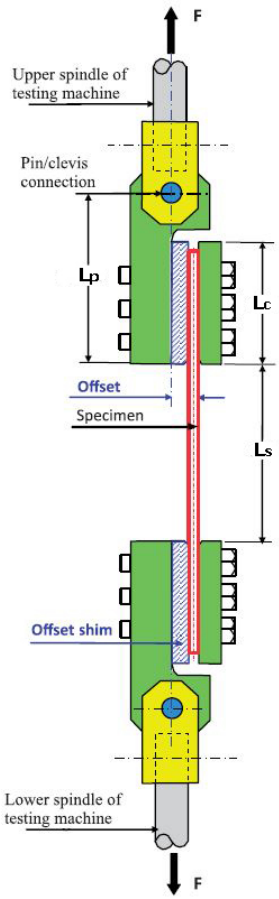

Figure 3.3: Hinged clamp tooling used by [37]

3.2.1. Calculation of Loading Ratio

The bending moment varies throughout the eccentrically loaded specimen. The resultant moment is dependent on the applied tensile force (F) and the eccentricity (e). As the specimen deflects towards the neutral axis, the eccentricity is effectively reduced by the displacement (y), leading to the expression for the moment to be:

$$M = -F(e - y) \tag{3.1}$$

The equivalent equation is 3.2. Deflection of the specimen is found by solving this second order differential equation.

$$EI\frac{\partial^2 y}{\partial x^2} = -F(e - y) \tag{3.2}$$

The general solution to equation 3.2 being

$$y = A\sin\left(\frac{\sqrt{F}}{EI}x\right) + B\cos\left(\frac{\sqrt{F}}{EI}x\right) - e \tag{3.3}$$

The boundary conditions for the pinned specimen of length L are $y = 0$ at $x = 0$ and $x = L$. Using the boundary conditions to solve coefficients A and B gives:

$$y = e\left[\tan\left(\sqrt{\frac{F}{EI}}\frac{L}{2}\right)\sin\left(\sqrt{\frac{F}{EI}}x\right)+\cos\left(\sqrt{\frac{F}{EI}}x\right)-1\right] \tag{3.4}$$

The maximum deflection occurs at the center of the specimen (L/2). Substituting $x = L/2$ into equation 3.4 gives

$$y_{max} = e\left[\sec\left(\sqrt{\frac{F}{EI}}\frac{L}{2}\right)-1\right] \tag{3.5}$$

The moment at the centre of the specimen and location of the TZ is then found by substituting the maximum displacement into equation 3.1. This is the moment assumed throughout the TZ. Even though the TZ spans a certain length, the variation in moment at the mid-section is minor. The ratio of the tensile force to the bending moment will largely affect the behavior in the TZ and determine which TZ design strategy is best. For the scope of this study, which mostly aims to establish a generalizeable methodology the load ratio is kept constant.

3.2.2. Design of Tooling

Figure 3.4 shows the experimental setup of a specimen loaded in the hinged fixture assembly. Two sets of attachment plates were designed and manufactured for the test. The final setup comprises of a clamping plate on each end of the assembly. These are fixed by the hydraulic clamps of the loading machine. The second set of plates is used to facilitate the load transfer into the specimen via two plates on each end. The load is introduced partly through bearing via an M8 bolt and partly by the frictional force due to the clamping force induced by two additional M10 bolts. The coupling element was kindly provided by the TU Delft materials laboratory. It serves as an intermediate part, connecting the two sets of plates by two perpendicularly oriented pins. The rotation of the fixture due to the eccentricity occurs in the outer pin attaching the coupling element and clamping plate.

The relation between the bolt tightening torque and resulting axial clamping load is given by equation 3.2.2. The standard tightening torque (T) for M8 and M10 8.8 strength grade bolts is 25.3 and 50.9 Nm. The coefficient of friction (μ_b) for steel bolts is 0.2. The resulting clamping force for an M8 and M10 bolt (D = 8 mm and 10 mm) is then 15 kN and 25 kN. In the present setup summing to an overall clamping force of 65 kN. With a coefficient of friction of 0.3 assumed between the composite and steel, the loading of the specimen by clamping is at minimum 20 kN.

$$F = \frac{T}{\mu_b D} \tag{3.6}$$

3.3. Specimen Design

Whereas specimens would conventionally be loaded directly through the hydraulic clamps of the machine, the necessity to enable rotation at the specimen clamps made this impossible. The clamping induced through the loading plate bolts alone would not yield enough force. The layup of the laminate requires more than a certain number of layers (thickness) to achieve a basic level of TZ

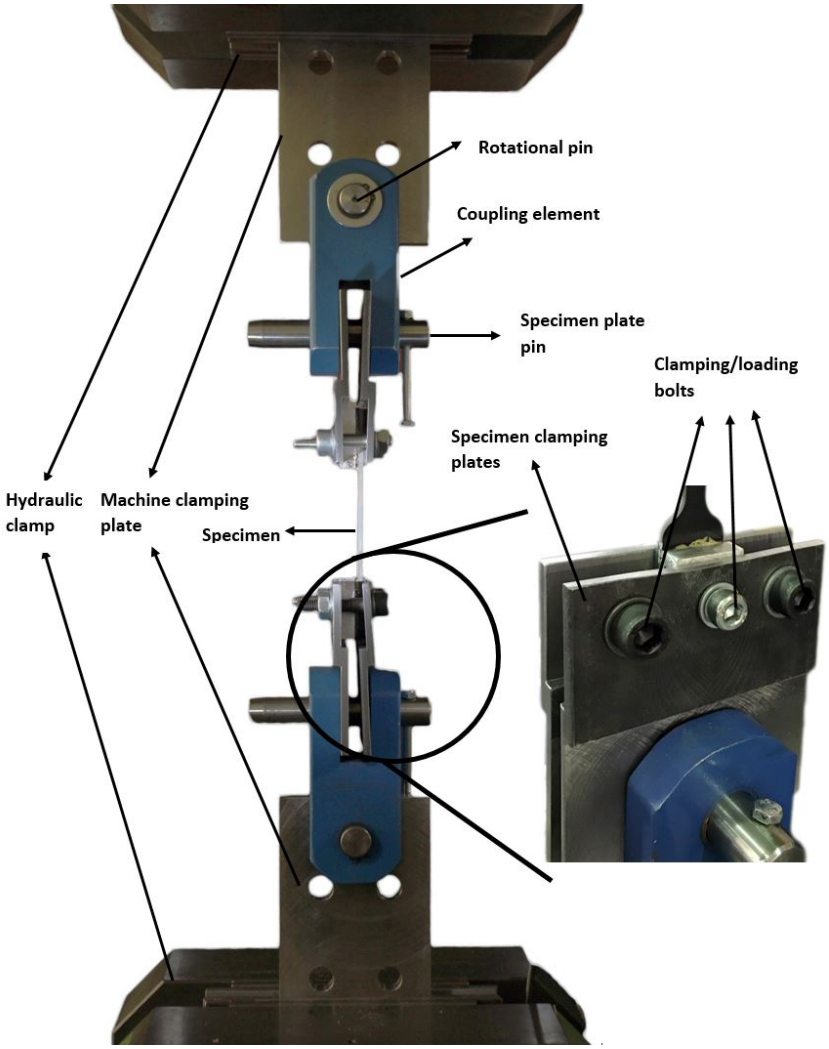

Figure 3.4: Experimental setup

design complexity. The implication is that either the loading force must be increased, and/or the failure force of the specimen reduced. Both methods are described in the Specimen Geometry section.

3.3.1. Layup

The details about the original layup are given in chapter 2.5.1. In its original configuration the laminate thickness is 16.3 mm. To be able to lead an experimental campaign with the available manufacturing possibilities, machinery and tooling it was necessary to reduce the laminate. The laminate was reduced in overall thickness, however the original orientation ratios were conserved. Therefore the directional properties remained unchanged. The layup of the final laminate with a thickness of 2.86 mm is:

$$(0_2/\text{-}45/90/45/0_2/\text{-}45/0/45/0)_s$$

The hybridization must follow the basic rules of laminate design, that is of symmetry and balance. Furthermore, the substitution of 0° plies should be strictly avoided. The 0° plies are the critical

load carrying plies and their interruption leads to a decreased overall load carrying potential and a higher risk for crack initiation at the AP of the composite and metal layers. Following the laminate and hybridization rules, the following hybrid design was chosen:

$$(0_2/St(\text{-}45)/90/St(\text{-}45)/0_2/St(\text{-}45)/0/St(\text{-}45)/0)_s$$

Overall, the orientation ratios were kept as close as was possible to the original layup. Achieving precisely the same ratios was however not possible with an overall smaller number of layers. The resulting ratios were (55/36/9). The ordering of the plies was also altered, namely the zero plies were placed on the outside of the laminate. Although this does not affect the elastic properties, it does impact the bending stiffness of the laminate. The ply orientations were free to be arranged to conveniently improve the flexibility for hybridization. In a realistic hybridization application this could likely not be the case. Often the form of the base layup is constant and the hybridization design would be compromised to fit. Unless the gains from a more ideally hybridized section outweighed the losses due to a rearranged sub-optimal base layup.

3.3.2. Transition Zone Design

Several TZ designs were conceived for the given laminate. The TZ arrangements were in the following categories. The halves of these arrangements symmetrical about the center-line are illustrated in figure 3.5.

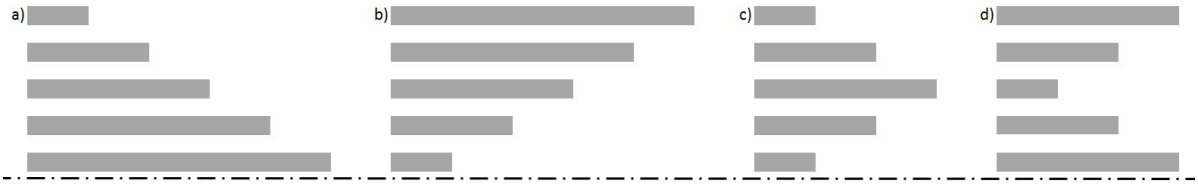

Figure 3.5: TZ arrangements: a) Short-Long b) Long-Short c) Short-Long-Short d) Long-Short-Long

a. Short-Long - From the outside to the laminate center-line, the metallic plies are increasing in length.
b. Long-Short - Metallic layers are arranged opposite to the Short-Long specimens.
c. Short-Long-Short - Metallic layer length increase and decrease from outside in.
d. Long-Short-Long - The opposite arrangement to Short-Long-Short.

This classification of ordering can be extended by further levels of going between shorter and longer steel foils. The number of times this can be done is limited by the number of steel foils in the laminate. For both the Short-Long-Short TZ and it's opposite themselves, there are multiple possible arrangements. As was observed in the study of Petersen et al. [56], different failure modes are expected in tension and bending. The purpose then in choosing the given arrangements was to make available a general range of orderings, in which the failure mechanisms of any further designs could be observed. The step size chosen for all the series was 10 mm, except for the short-long arrangement, where a 5 mm step was used. An FEM model correlated with the results of an exhaustive experimental campaign can be expected to capture all occurring failure phenomena.

3.3.3. Specimen Geometry

The specimen dimensions were selected in parallel with the design of the laminate and test setup. The specimen dimensions are shown in figure 3.6. M8 clearance holes were introduced to increase the loading force through partial bearing loading. The holes were sized and positioned to satisfy the minimum W/D and E/D ratios. With both ratios approximately 3, this is a conservative design owing to the additional clamping pressure exerted by the attachment plates.

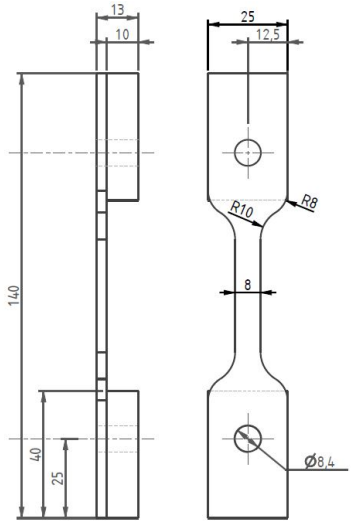

Figure 3.6: Dimensioned specimen drawing

The specimens were loaded through bearing and friction induced by the clamping plates. The specimens were drilled, which introduced a weak-point in the specimen outside of the intended failure region and otherwise weakest point of the specimen - the TZ. Even with bearing failure occurring first, there is enough residual strength due to the high E/D ratio for net-section failure to occur. Taking a stress concentration factor of 3 for the hole, the net section failure load would be expected around 17 kN. Summed with the clamping force exerted by the plates, the maximum load would be 37 kN. Experiments confirmed this prediction, with failure occurring around 35 kN. Apparently less force was transmitted through the clamping plates than was initially expected. Using a limit load of 30 kN, the maximum width of a monolithic CFRP specimen would be 8mm to fail at it's centre, resulting in the dog-bone shaped specimen showed in figure 3.6. Ideally the width of the specimen at its mid-section would be larger for possible edge effects to be observed. However as was observed in benchmark simulations and shown in figure 4.6, edge effects can be expected to be negligibly small.

3.4. Specimen Manufacturing

All specimen manufacturing was performed at the DLR Braunschweig laboratories. The DLR Institute of Composite Structures currently focuses on investigating hybridization using steel. Following the discussion of titanium vs steel hybridization in section 2.1.2, steel/CFRP materials were investigated mainly due to practical reasons of established material preparation techniques, manufactur-

ing procedure know-how and lower cost.

3.4.1. Preparation and Surface Treatment

The materials used were HexPly M21/35%/T700GC prepreg and stainless steel 1.4310 with a ply thickness of 0.13 mm. were used. The prepreg plies were cut using an automated plotter cutter. The only available method for cutting the metallic plies was manually using metal sheet shears. To be cut on the plotter, the sheet was too thick. Using other plotter cutters, such as a laser cutter would again affect the surface quality after being pre-treated. Prior to cutting the metal foil, a surface treatment is necessary for better wetting and adhesion. The surface treatment is divided into a pre- and post-treatment stage. The purpose of the pre-treatment is to de-grease the surface and abrasively remove any weakly adhered (oxide) layers [68]. Several methods are available for the pre-treatment. A pickling chemical treatment can be used for very thin foils (t<0.08 mm). The alternative method for thicker foils, which are not at risk of being damaged or work hardened is grit-blasting. The grit blasting method employed was vacuum assisted. The abrasive particles moving at a small angle relative to the foil did not pose a danger to damaging the foil. After grit blasting, the foil was cut into the necessary layup lengths. After cutting the foils, the post-treatment follows the standard *Boeing sol-gel* process. This chemical treatment consists of a dilute solution of alkoxyzirconium organometallic salt and a organosilane coupling agent in combination with a acetic acid catalyst [68]. The foils were cleaned with acetone before being submerged in the solution for a minimum of 60 seconds. After which they were removed from the bath and hung until completely dried.

3.4.2. Laminate Layup and Curing

The laminates were laid up by conventional methods by hand. Exceptional attention was given to laying up the layers combining metal and composite. Namely to the APs between the two materials. Care was taken to avoid either an overlap or a gap between the abutting plies. The manual cutting of the foils resulted in imperfectly straight edges. Consequently, even with the greatest care, the metal and prepreg layers in some cases did not align precisely.

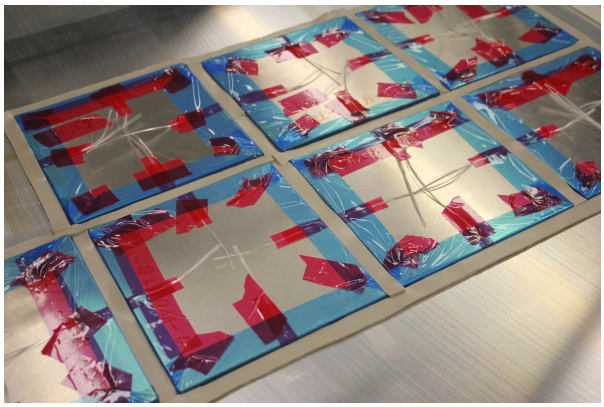

Figure 3.7: Laminates on the tool with sealant tape dams to prevent resin flow out

Figure 3.7 shows the assembled laminates placed on the tool and bordered with sealant tape. The purpose of these sealant dams is to prevent excess resin from flowing out during curing. The

fiber volume content thus remains constant. The remainder of the vacuum bagging procedure followed conventional techniques. The laminates were cured in an autoclave under the cycle graphed in figure 3.8.

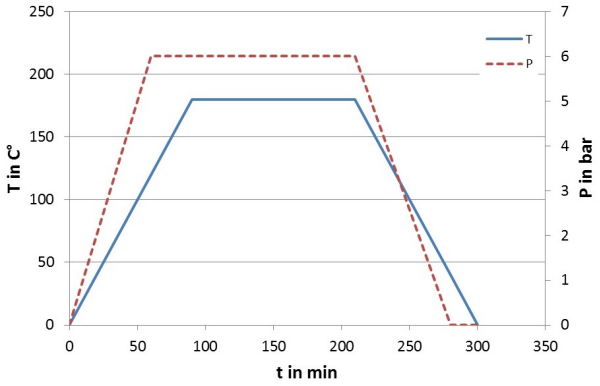

Figure 3.8: Autoclave laminate curing cycle

3.4.3. Specimen Preparation and Quality Inspection

Pre-manufactured glass fiber end tabs for the regions to be gripped were bonded using a Henkel Hysol EA9695 epoxy adhesive film. Specimens were then cut out with water-jet in their designed sizes. The spacer blocks were bonded to the specimen ends using the same adhesive film. The specimens were then drilled with an M8 clearance drill (8,4 mm).

Microscopy images were taken of the TZ cross-sections. A representative sample photo from each series is shown in figure 3.9. The actual TZ arrangement clearly differs from the ideal design. Due to the low level of accuracy in manual cutting the foils, step lengths vary by up to 2mm from their design length. Subsequently the TZ is not perfectly symmetrical.

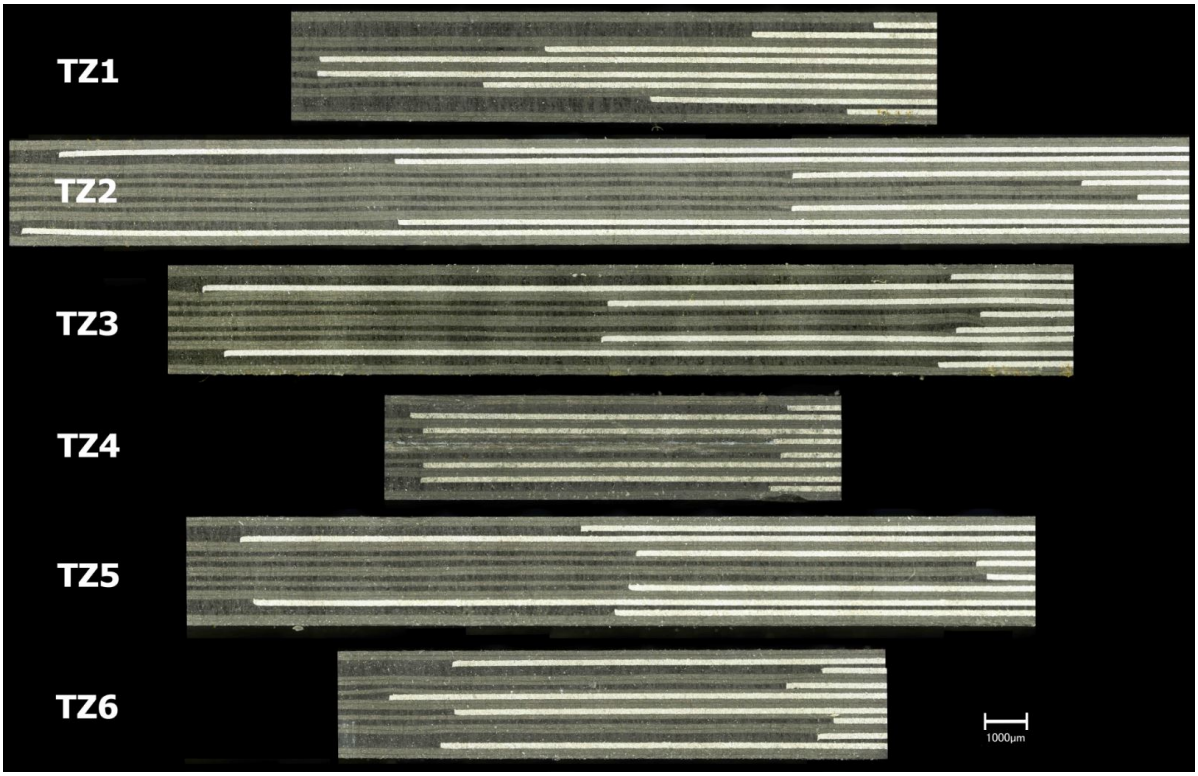

Figure 3.9: Microscopic images of TZ cross-sections

Zooming in closer on the APs and foil edges reveals further manufacturing defects. In some cases there are burrs on the edges of the foil, also caused by manual cutting. An example is shown in figure 3.10. The burr acts as an obstruction to a smooth adhesion between the foil and the neighbouring ply in the region around the foil edge. The burr can cause a flow of resin between the foil and neighboring ply. Figure 3.10 shows one of the most severe burrs. Here the extent of the foil and ply separation is approx. 1 mm. Overlaps of the foil and composite ply are also observed, such as in figure 3.10. These overlaps are caused by the imperfectly straight foil edges. Resin rich regions caused by gaps between APs are not visible from the microscopy images, but are also expected to be present.

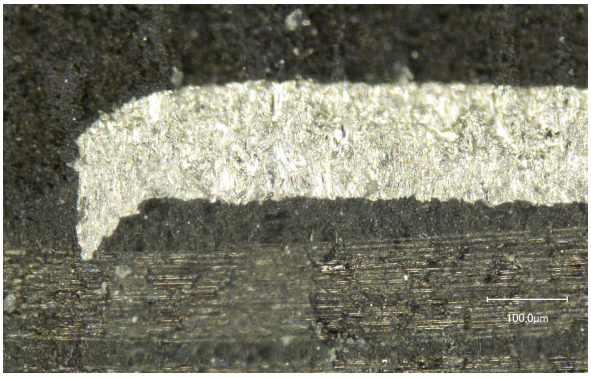

(a) Steel foil edge burr

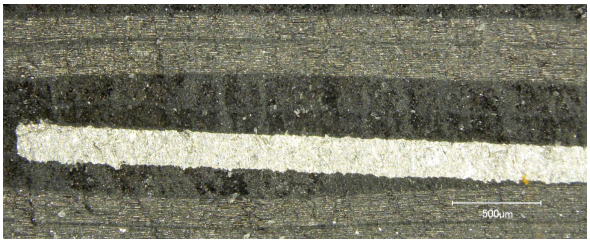

(b) Overlapping steel and composite layers

Figure 3.10: Manufacturing steel foil edge imperfections

Table 3.1: Test matrix showing excluded samples

		Series					
		TZ1	*TZ2*	*TZ3*	*TZ5*	*TZ6*	*COMP*
Specimen	*1*	TZ1-1	TZ2-1	X	TZ5-1	TZ6-1	COMP-1
	2	TZ1-2	TZ2-2	TZ3-2	TZ5-2	TZ6-2	COMP-2
	3	TZ1-3	TZ2-3	TZ3-3	TZ5-3	TZ6-3	COMP-3
	4	TZ1-4	TZ2-4	TZ3-4	X	TZ6-4	X
	5	TZ1-5	TZ2-5	TZ3-5	X	TZ6-5	X

All in all, 1 reference CFRP laminate and 5 hybrid laminates with various TZ designs were manufactured, each producing 5 test samples. Some samples and the entire series TZ4 were invalidated during their preparation, and therefore left out. The test matrix in table 3.1 shows which specimens were tested and gives their code names for further reference.

3.5. Strain measurement with Digital Image Correlation

Since it's early developments in the 1980s Digital Image Correlation (DIC) is emerging as an attractive method for strain measurement among other optical methods such as moiré, holographic or speckle pattern interferometry. The general method for implementing DIC is summarized in 3 steps by Pan et al. [52]. DIC is now available in both 2D and 3D, enabling the measurement of out of plane deformations. The methodology for both of these methods is elaborated in the following sections.

1. Specimen and experiment preparations.
2. Recording images of the specimen before and after loading.
3. Processing images using a computer program to obtain the strain information.

3.5.1. Specimen Preparation and System Setup

The setup of a typical 2D DIC system is shown in figure 3.11. Kosmann et al. [40] investigated different lacquering techniques and based on their reproduciblility and speckle size determined titanium dioxide and black iron oxide on a white powder background to have the best results. The surface of the object is then observed with an imaging device. This can be a conventional CCD, simple consumer digital camera, high-speed video camera or even scanning electron microscope imagery. For the 2D imaging system units to be accurately translated to physical displacements the specimen must be flat and it's plane be in parallel with that of the camera. In reality complete parallelism will not be achieved. A 5°deviation results in displacement errors less than 0.01 pixels [47]. Helm and Deaner [27] were able to show that off-axis angles as high as 30° can be compensated for by proper calibration.

A more important issue in the case of 2D DIC is out of plane motion. Changes in distance from the object to the lens alter the magnification. If slight out of plane motion is expected, a telecentric lens can be used or the camera should be placed further from the object to achieve a similar effect [45]. 3D DIC systems are available for tests with large out of plane displacements, however for the present application such a system is not necessary. With additional lighting higher lens F-stop numbers can

be achieved. By closing the aperture, the depth of focus increases, reducing the distortion in both 2D and 3D DIC.

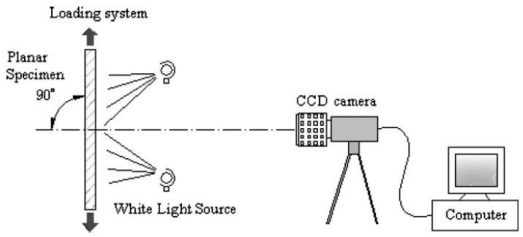

Figure 3.11: Typical 2D DIC setup[52]

As suggested by Kosmann et al. [40], the titanium dioxide and iron oxide powder combination was used to create the speckle patterns. The specimens were first sprayed with the iron oxide powder in an ethanol suspension. Once a homogeneously black surface was achieved, the surface was sprayed with the titanium oxide powder. The quality of the speckle pattern rested mainly on this step and was largely influenced by the judgment and skill of the person applying the pattern.

A digital Sony Alpha 7 II camera was used for recording images. The length of the TZ across the specimen series was just 20-40 mm, therefore a macroscopic lens was used in order to obtain a high resolution of the area of interest. With an image resolution of approx. 7000x5000 pixels, it was ensured that the camera resolution would not be a limiting factor to the level of measurement detail. The measurement resolution was then limited by the minimum achievable size of the individual speckles created by the deposited titanium oxide. The camera was used in conjunction with a trigger box linking the force/displacement output of the testing machine with the image recording. Thus enabling simpler synchronization of the data for post-processing.

3.5.2. Measurement and Calculation

An image is taken at desired stages of deformation of the object and recorded in a computer. A single pixel is impossible to track, therefore discrete areas of pixels called subsets are identified on each image. Kosmann et al. [40] specifies a minimum area of 10x10 pixels, but recommends larger areas to protect against voids in the specle pattern. There is a trade-off between using smaller subsets in the order of units of pixels or larger subset up to an order of hundreds of pixels. The subset should be large enough so that it is unique enough in its light intensity distribution to be distinguished from others and tracked. On the other hand using large subsets leads to increased error margins in the approximation of deformations. The choice of subset size is therefore critical to the accuracy of the measurements [52]. Each subset is unique in it's light intensity distribution and it is assumed that this intensity does not change throughout the deformation process. A comparison is made between images at succeeding stages of deformation. The mapping of points from the reference image to the deformed image is done according to a chosen shape/displacement mapping function [52]. Depending on the nature and complexity of deformation, the shape function can be of zero, first or second order. The entirety of the post-processing and analysis work was done using GOM Correlate software. The results were used to produce strain field plots, which are discussed and correlated with the numerical results in the Results chapter.

4

Finite Element Modelling

4.1. Modelling Interlaminar and Intralaminar Failure

The initiation and growth of delaminations is of the most detrimental in failure mechanisms of FMLs. There is a clear necessity for accurate modeling of delamination behaviour. There are two well studied methods for the use of FEM in simulating delamination. They are the Virtual Crack Closure Technique (VCCT) and the use of cohesive zone elements.

4.1.1. Virtual Crack Closure Technique

The VCCT technique first proposed by Rybicki and Kanninen [64] can be used to evaluate the ERR during delamination growth. This is done under the assumption that the energy released in opening a crack is equal to the energy required to close it back to it's initial length. The nodal forces and displacements from the finite element solution can be used to calculate the ERR in all three types of opening modes. The following equations specify the calculations of the ERR for the three modes:

$$\begin{aligned} G_I &= \frac{1}{2b\Delta a}(X_1 \Delta u_2) \\ G_{II} &= \frac{1}{2b\Delta a}(Z_1 \Delta w_2) \\ G_{III} &= \frac{1}{2b\Delta a}(Y_1 \Delta v_2) \end{aligned} \tag{4.1}$$

X Z and Y are the magnitudes of the nodal forces at point i and Δu and Δw the displacement of the nodes at that point to close the crack, with b the specimen thickness (width of the crack). The summation of the individual mode contributions gives the total energy release rate. Once a critical rate equal to the fracture toughness of the material is reached, the crack is predicted to propagate [72].

The advantage of this approach is that it is computationally efficient. Only one analysis is necessary to determine the energy release rate [10]. The added complexity of the method is that an initial crack must be included in the model. Furthermore the calculations detailed by equations 4.1 require nodal variable output ahead of and behind the crack, which may require remeshing of the model as the crack propagates [73].

4.1.2. Cohesive Zone Modelling

The cohesive zone model (CZM) is commonly applied in FEA to simulate interfacial fracture. Pioneered by Dugdale [17] and Barenblatt [6], the assumption of the CZM is that a plastic damage zone undergoing softening is developing around the crack tip. This is illustrated by figure 4.1, where there is a restraining stress, which is a function of the separation distance in the plastic zone acting to keep the separation surfaces together. Increasing separation distance leads to an increase in separation stress (traction) to a maximum cohesive strength. With further separation the traction decreases before reaching zero and complete decohesion occurs.

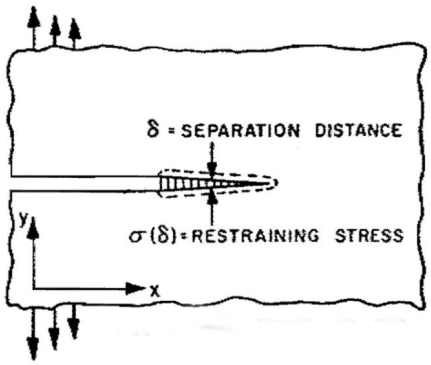

Figure 4.1: Dugdale Barenblatt crack model cohesive zone [62]

There are multiple models with distinctly defined cohesive constitutive equations. The simplest of which is the bilinear equation with a simple constant gradient ramp up and ramp down. Other examples of traction displacement curves used in literature are shown in figure 4.2. The area under the graphs in these figures is equal to the fracture toughness. Volokh [79] used the block peel test to compare bilinear, parabolic, sinusoidal and exponential separation laws. Their findings countered the conventional view that cohesive strength and separation work are the governing parameters of the cohesive zone model behavior. They were unable to draw conclusions about the relationship between the cohesive equation and model behavior, but were nevertheless successful in showing that the specific shape of the traction-separation curve is very important and not subsidiary, as was perceived previously. Clearly then, the choice of the model will affect the stability and convergence of the model.

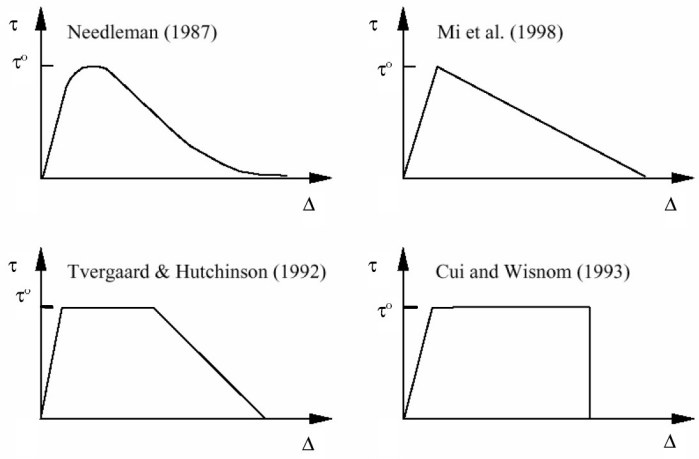

Figure 4.2: Plots of cohesive constitutive equations [82]

Modelling Parameters

There are a number of parameters in the delamination analysis which must be determined for accurate modelling. Most important of these are the numerical parameters of cohesive element (or the element with cohesive properties) size, strength, stiffness and the physical parameter of critical ERR. There are some numerical difficulties with the proper definition of the stiffness of the cohesive zone. The cohesive contribution to the compliance must be small enough so as to avoid effects on the global stiffness of the model. Similarly for element size, the cohesive elements at the interface must be sufficiently fine to capture the separation stress distribution in the cohesive zone and certainly the element size must be less than the cohesive zone length (CZL). Where the length of the cohesive zone is defined as the distance from the crack tip to the point where the maximum cohesive traction is attained [74]. Different models exist to estimate CZL with common models being those of Hillerborg et al. [30] and Rice [63], both taking the general form of:

$$l_{cz} = ME\frac{G_c}{(\tau^0)^2} \tag{4.2}$$

The parameter M depends on the specific cohesive zone model, such as one of those in figure 4.2. In the two common models and others using bi-linear traction-separation laws M is close to unity. E being the material's Young's modulus, G_c the critical ERR and τ^0 the interfacial strength. The ERR used in equation 4.2 is of mode I. The ERR for this mode is lower and the modelling of the cohesive zone is thus more conservative if mode II failure is expected to dominate.

Reading equation 4.2, the CZL is small in graphite-epoxy composites due to their relatively low fracture toughness and high strength. The minimum number of elements needed in the cohesive zone is not exactly established. The minimum number of elements used throughout literature is 2. Harper and Hallett [24] state that using more than 3 elements is conservative. Excessively fine meshes will clearly result in large computational times. It was shown by Turon et al. [74] that the mesh density can be reduced by a lowering of the interfacial strength. This method is allowable due to the fact that once a crack has been initiated, the results are relatively insensitive to the exact element stiffness as long as the fracture toughness (area under the traction-separation curve) is still

accurate. Blackman et al. [7] borders this argument with his findings that excessively low interfacial strength results in inaccurate load-displacement results, suggesting that limits should be set on the allowable strength reduction. The interfacial strength can be calculated using equation 4.3

$$\tau^0 = \sqrt{\frac{9\pi E G_c}{32 l_{cz}}} \tag{4.3}$$

Equation 4.4 was used by Turon et al. [74] to calculate the interface stiffness. The coefficient α is a parameter $\alpha \gg 1$. E_3 is the through thickness Young's modulus of the material. For transversely orthotropic materials $E_3 = E_2$. The value used by Camanho and Davila [10] for Graphite/Epoxy was $10^6 N/mm^3$ yielding accurate results.

$$K = \frac{\alpha E_3}{t} \tag{4.4}$$

Element vs. Surface Cohesive Modelling

There is a cohesive surface definition available in Abaqus, which can be used in place of cohesive elements. The results from both methods are close to one another. Nevertheless there are some advantages and drawbacks to this alternative method [69]:

- Unlike surfaces, elements can be given a thickness definition enabling thickness effects to be incorporated in the simulation.
- The use of elements gives direct control over the mesh density and stiffness properties. Refinement of the cohesive elements leads to increased accuracy. On the other hand cohesive surfaces are easily defined with a master-slave relationship and accuracy can be increased by refining the slave surface elements.
- Cohesive elements often require a small stable time increment. This is due to their relatively high stiffness. Which can also be reduced based on the previous discussion.

In summary, cohesive elements offer more control over their definition and failure characterization output. They are suitable for more detailed adhesive connection modelling, but require some preprocessing work and result in longer solution times. The use of cohesive surfaces offers increased simplicity on all fronts. Due to the complexity of the model and the number of cohesive zones within one model, the use of cohesive surfaces offers itself as the more practical approach.

4.2. Modelling Strategy

As is generally the practice for FEM model design, the aim throughout the design of the model was to reduce the computational time. When modelling composites, geometrical reduction of the model is made impossible by the plies angled to the plane of symmetry. Therefore the model could not be reduced in plane to its half or quarter, as could normally be done for a homogeneous material. The modelling of delaminations and the nature of the loading prevented further reductions of the model. Due to the out of plane loading of the specimen, the whole model was modelled fully

through its thickness. The region of interest in the model is the TZ and the surrounding area to which delaminations could extend. Only the region between the clamps was included in the model, that is the free 70mm long laminate section between the eccentricity blocks.

The definition of the cohesive surface is specified by the Abaqus Manual [28] in 3 steps. The ways in which these steps were covered is described in the following sections.

1. Defining the surfaces of the bodies that could potentially be in contact.
2. Specifying which surfaces interact with one another.
3. Defining the mechanical surface interaction model that governs the behaviour of the surfaces when they are in contact.

4.2.1. Surface Definition and Interaction Properties

The more cohesive surface interactions there are in a model, the more computationally intensive it is to achieve step convergence. From the studies on the TZ by Petersen et al. [56] and the research into failure of FLMs, the delamination can be expected to initiate at the APs of the steel and composite layers and propagate through the metal composite interface. The number of cohesive surface definitions should therefore be minimized to those interfaces which are expected to delaminate. In a combined tensile-bending loading case, a mixed-mode delamination is expected. By far the weakest steel-composite interface in mode I is at a fiber orientation of 0°. Of the composite interfaces listed in table 4.1, there are only 0° to 0° ply interfaces in the present model. The mode II ERR for this interface is higher than that of any steel interface. The delamination in purely composite laminates is a well studied topic and due to the reasons described is less likely be the point of critical damage initiation. The interest in this thesis is in the effect of introducing interrupted metallic plies in the laminate and their effect on delamination. It is then namely the steel-composite interfaces, which are studied for crack nucleation and growth to delaminations. The cohesive interactions were therefore only defined at the metal surfaces, which leaves only steel-0° and steel-90° interfaces.

The quantities specified in the model are G_Ic, G_IIc and G_IIIc, which refer to the critical fracture energies required to cause failure in the normal, first and second shear directions respectively. The critical ERR values of the steel-composite interfaces for the materials used in this study were found by Petersen and Hühne [54], and are summarized in 4.1. The ERR in mode 3 can be taken to be equal to that in mode 2. The standard tests used to determine the ERR are the double cantilever beam (DCB) and end-notched flexure (ENF) test, specified by standards ASTM D7905 [4] and D5528-13 [3]. Significant spread was found in the results of these tests. For this reason, benchmark correlation studies simulating the DCB and ENF tests were done with the experimental ERR values.

When the experiments are reproduced with FEM using the ERR values derived from the experimental results, the numerical results show a deviation. In the case of the DCB test, the results plotted in figure 4.3 show a good correlation, with a slightly reduced stiffness. A comparison of the results for the ENF test of a steel-0° interface is shown in figure 4.3. The line plotting FEM results using experimental values shows a steady softening with no clearly identifiable full degradation point. The critical ERR is too low in this case for fast fracture to occur. A reduction in the ERR results in the FEM line with adjusted values. The correlation of course does no only rest on the ERR. A para-

Table 4.1: Mode I, II and III fracture toughness for various material interfaces [54]

Interface Critical Energy Release Rate(kJ/m^2)	G_{Ic}	G_{IIc}/G_{IIIc}
Steel - 0°	0.229	1.887
Steel - 90°	0.474	1.560
Steel - 45°	0.408	1.685
0° - 0°	0.338	2.291
0° - 45°	0.538	2.707
0° - 90°	0.891	2.524
45° - -45°	0.821	2.418

metric study of the cohesive zone strength illustrated by figure 4.5 shows the effect of increasing the strength. With higher interfacial strength, the point of degradation is shifted toward higher loads. In combination then, the interfacial strength sets the point of rapid degradation, while the critical ERR sets the rate of softening. The strength is calculated using equation 4.3, which gives strengths of 10 MPa and 40 MPa for mode I and II respectively. Looking at figure 4.5, the point of failure correlates best with the experimental data with strengths of 15 and 30 MPa for the two modes. Figure 4.6 illustrates the severity of the edge effects in the models. In the DCB test, the delamination crack front was ahead at the centre of the specimen, where the opposite effect was observed in the ENF test.

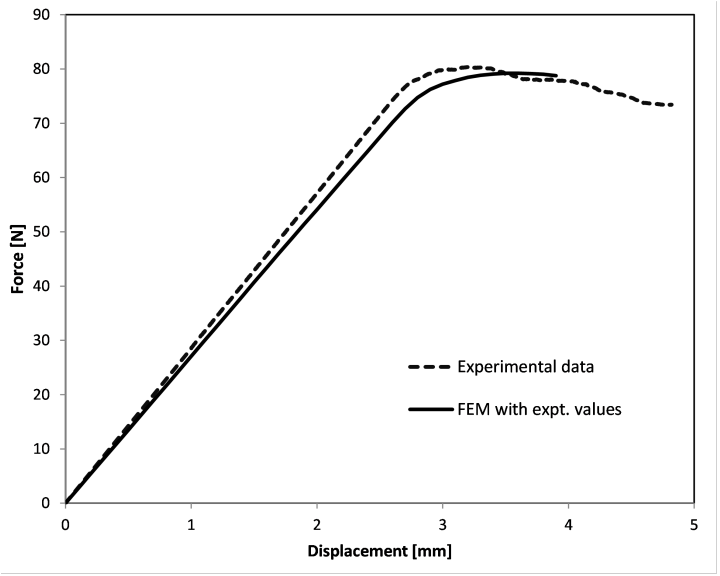

(a) FEM matching of experimental DCB test results for a steel-0° interface

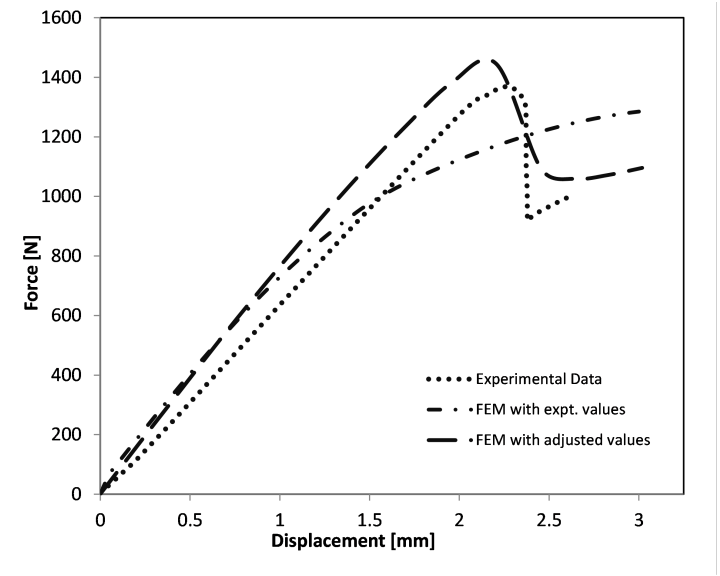

(b) FEM matching of experimental ENF test results for a steel-0° interface

Figure 4.3: Benchmark DCB and ENF test simulation correlations

The ENF experimental curve itself is one of a series, in which a significant spread of results was observed. Maximum force at failure ranged between 1370 to 1530 N at corresponding maximum displacement of 2.19 to 2.60 mm. In all cases, the numerical results exhibit a higher stiffness. However with the adjusted ERR values, the region of failure lies in the limits of the experimental series. There are several data reduction methods applicable in the calculation of the mode I ERR stemming from the DCB experiment results. Depending on which calibration method is chosen, in the case of the tests performed by Petersen et al. [56], the values can differ by as much as 8%. The discrepancy between the experimental and numerical results can therefore be simply due to an incorrect choice of correction method. The final adjusted ERR and strength values used for the steel-0° interface were 0.21 and 1.6 kJ/m^2 and 15 and 30 MPa for mode I and II respectively. The same correlation study was done for the 90°-steel interface, illustrated by figure 4.4. Here a good correlation was observed using experimental values and strengths found from the parametric study described previously. The interface stiffness used was $10^6 N/mm$, as reported in literature by Camanho and Davila [10].

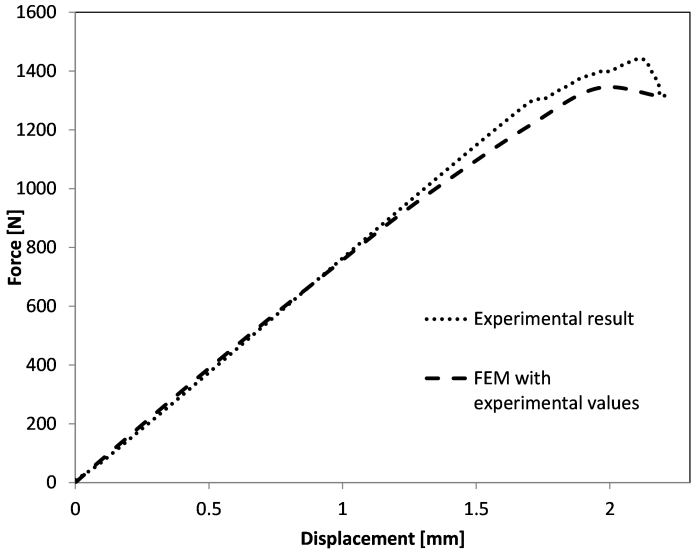

Figure 4.4: Correlation of ENF experimental and model results using experimentally obtained ERR

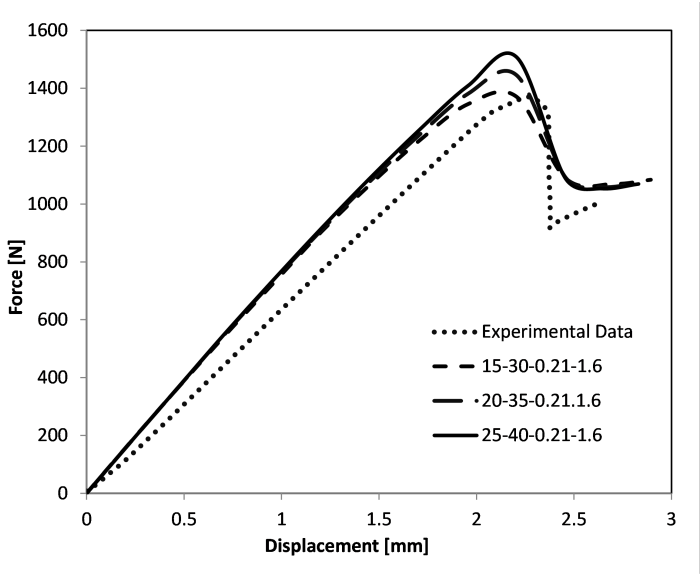

Figure 4.5: Effect of increasing interlaminar strength in FEM ENF test for a steel-0° interface
Legend nomenclature: mode I strength - mode II/III strength - mode I ERR - mode II/III ERR

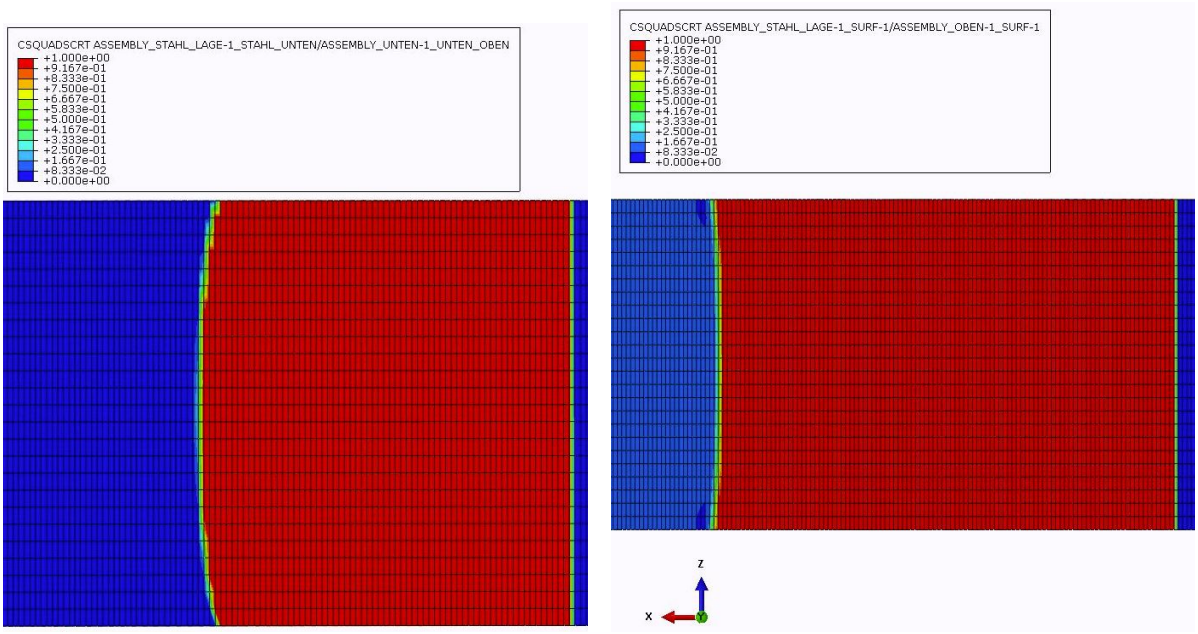

(a) Edge effects for the DCB test of a steel-0° interface

(b) Edge effects for the ENF test of a steel-0° interface

Figure 4.6: Edge effects observed in DCB and ENF simulations - crack progression in x-direction

4.2.2. Meshing Strategy and Boundary Conditions

The model could theoretically be reduced to 2D, however the definition of material orientation in Abaqus does not allow the 2 direction to be oriented out of plane. In the words of the Analysis User Guide: "When a user-defined orientation is used with two-dimensional solid elements such as plane stress or plane strain, the orientation must redefine only the X(1)- and Y(2)-directions: the third direction must remain unchanged (Z(3)-direction for plane strain and plane stress elements)." [28]. Even with the possibility of using a method of transformation of the engineering constants, the damage model intended to be used is only applicable to 3D elements. The modelling space is limited to 3D modelling, in which either solid or continuum shell elements can be created. To model delamination between individual plies, the plies had to be modelled as individual parts. A solid representation of the plies offers greater simplicity in modelling. The use of solid elements would normally be associated with a larger computational time, due to a larger number of elements through the part thickness. Since the thickness is much smaller compared to the other ply dimensions, only one element can be used through the thickness. Solid elements can then be used without involving additional computational time. Solid elements allow for full (non-reduced) integration and are more suitable for nonlinear modelling involving contact. The elements used in the study were therefore solid, full integration C3D8 elements.

Using equation 4.2, the length of the cohesive zone for the given material is 1 mm. With three elements in the cohesive zone, the element size in that region should not be larger than 1/3 mm. With only delamination of the metallic plies being modelled, the mesh was reduced to its minimum size at those interfaces. Both the metallic ply and composite part meshes needed to be refined. The same method for determining the element length was used in the benchmark simulations of the DCB and ENF tests. The models correlated well with the adjusted cohesive parameters, indicating that the element length was sufficient.

The model reductions and simplifications outlined in this section were implemented in the final design of the model. The mid-section of the specimens was modelled with the omission of the widened ends. The widening of the edges was not modelled for several reasons. The region of interest is in the narrowed section of the specimen, which is unaffected by the deformation in the far removed edges. The results can still be correlated locally by taking an equivalent section from the DIC results. Convergence issues and time step are reduced due to the lower complexity and removal of radii. The combined loading case was simulated by loading through offset reference points. Figure 4.7 shows reference points tied with coupling constraints to the specimen edges and offset to the specimen edges. Displacement boundary conditions were applied to RP1 with RP2 fixed. The offset in z is equal to the eccentricity due to the spacer blocks in the experiment. A displacement of the RP results in a moment in the specimen through the offset arm. The offset in x simulates loading through the tool, in which rotation occurs at the pins displaced at 170 mm from the specimen edges.

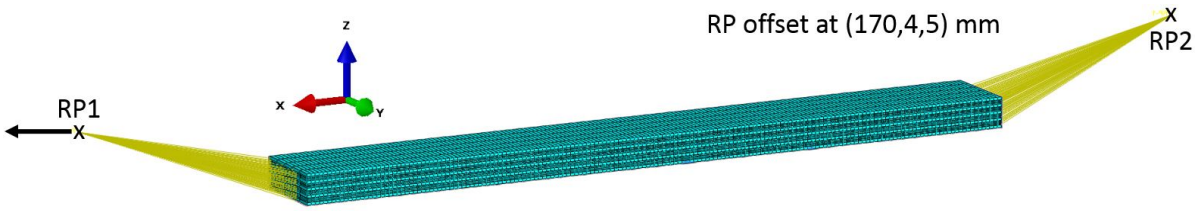

Figure 4.7: Model simplification and loading

4.2.3. Material properties

The material properties listed in table 4.2 are based on experiments made by Petersen et al. [55]. The same authors found the plastic properties of the metallic foil, which were incorporated in the model with a simple plasticity material property [56].

Table 4.2: Prepreg and steel foil elastic and strength material properties

HexPly M21/35%/UD134/T700GC				**Steel 1.4310**			
Elastic Properties [MPa]		**Strength [MPa]**		**Elastic Properties [MPa]**		**Strength [MPa]**	
E_{11}	114150	X^t	2230	E	167000	σ_u	1476
E_{22}	8300	X^c	1537	μ	0.3	$\sigma_{Rp0.2}$	1301
E_{33}	8300	Y^t	71				
μ_{12}	0.298	Y^c	202				
μ_{23}	0.295	S_{12}	78				
G_{12}	4100						
G_{13}	4100						
G_{23}	3000						

4.2.4. Stiffness Degradation and Damage

Progressive Damage Modeling - Intralaminar Failure

Progressive damage models can be implemented in Abaqus either using a user defined material or user defined field subroutine. The user defined field method has been demonstrated to be slightly less accurate than the slightly more complex user defined material definition. Nevertheless it has been used by several authors to simulate bearing failure including delamination and damage degradation [33, 70]. In Abaqus the material properties can be defined as functions of the solution data. As such, the stiffness can be defined as a function of the strain for the case of fiber failure and as a function of stress for matrix damage. The simulation is updated at each increment, where the subroutine is called at the end of each increment. The stresses and strains are called from the previous step and failure indexes are calculated to check against failure. If failure occurred, the material properties are degraded. If not, the failure indexes are recalculated with new stresses at the end of the step. Failure indexes are recalculated and properties are degraded in case of failure. The failure indexes can be calculated based on any chosen failure criteria.

The stiffness degradation was implemented with the use of a user defined field subroutine. The subroutine used in the model was originally developed by Puzio [60]. The subroutine captures the degradation in stiffness after damage has occurred, presented as a percentage of the original value.

The failure criteria in the subroutine are the Cuntze criteria. There are five distinct failure modes, also shown in figure 2.9.

- FM1 - Fiber tension failure
- FM2 - Fiber compression failure
- FM3 - Matrix tension failure
- FM4 - Matrix compression failure
- FM5 - Shear failure

There are only two material states - full stiffness and full degradation. The residual stiffness after each failure mode has occurred, is expressed as a fraction of the initial stiffness. The stiffness reduction factors for each mode are tabulated in table 4.3. As can be seen from the table, failure in some modes results in larger stiffness degradation than in others. For example tension fiber failure is clearly more damaging and results in a lower residual stiffness, whereas shear failure leaves tensile properties in the principal directions unaffected. Mixed mode failure is also possible. If the criteria for two types of failures are met, the most severe degradation for each stiffness is taken.

Table 4.3: Stiffness degradation in each failure mode (FM)

Mode	E_{11}^0	E_{22}^0	E_{33}^0	μ_{12}^0	μ_{13}^0	μ_{23}^0	G_{12}^0	G_{13}^0	G_{23}^0
FM1	0.001 E_{11}	0.001 E_{22}	0.001 E_{33}	0	0	0	0.001 G_{12}	0.001 G_{13}	0.001 G_{23}
FM2	0.1 E_{11}	0.1 E_{22}	0.1 E_{33}	0	0	μ_{23}^0	0.1 G_{12}	0.1 G_{13}	0.1 G_{23}
FM3	E_{11}	0.001 E_{22}	0.001 E_{33}	μ_{12}^0	μ_{13}^0	0	G_{12}	G_{13}	0.001 G_{23}
FM4	E_{11}	0.2 E_{22}	0.2 E_{33}	μ_{12}^0	μ_{13}^0	0	G_{12}	G_{13}	0.2 G_{23}
FM5	E_{11}	E_{22}	E_{33}	0	0	μ_{23}^0	0.2 G_{12}	0.2 G_{13}	0.2 G_{23}

Interlaminar Failure

Abaqus offers four default cohesive zone damage initiation criteria. The criteria are based either on stress or traction in linear and quadratic forms. The quadratic stress criterion used in this study is represented by equation 4.5. The peak values of contact stresses purely in the normal and two shear directions are defined by t^0. The quadratic stress criterion is visualized in figure 4.6. The crack in these models is progressing in the x-direction, with the red areas fully delaminated, where the criterion is satisfied.

$$\left\{\frac{t_n}{t_n^0}\right\}^2 + \left\{\frac{t_s}{t_s^0}\right\}^2 + \left\{\frac{t_t}{t_t^0}\right\}^2 = 1 \tag{4.5}$$

In defining damage initiation, the evolution of damage can be either linear or quadratic. A linear damage evolution branch would resemble that of Mi et al. and a quadratic one that of Needleman from figure 4.2. The claims by Volokh [79] about the influence of traction-separation curve shapes were based on mode I dominated tests. The choice between a linear or exponential softening branch did not show to have an effect on the present model results, as failure is predominantly in mode II. Finally a linear damage evolution relation was used.

5

Results and Discussion

5.1. Test Results

All specimen series were tested with the exception of TZ4 due to a manufacturing defect with a pre-existing delamination. With the exception of one specimen, the rest were tested until final failure. For the purpose of microscopy, testing of one specimen per series was stopped after sounds of first cracking were heard. The presentation and discussion of results in this chapter is done mostly for the representative series TZ1. Experimental and numerical results from all series were studied and correlated. Observations of phenomena in other series which are not made in the representative series are indicated where relevant.

5.1.1. Suitability of the Test

The intention behind the selection of a combined loading scenario was to create a more inclusive loading case. In realistic structure designs it can be expected that there will be a variation in stress across the thickness due to some additional bending moment. The bending moment generated by the test rig can be derived analytically, as was done in section 3.2.1. Local strain measurements can be taken from the DIC strain field output, as was done in figure 5.1. Point 2 lies on the side of the specimen in higher tension. The plot confirms a higher strain compared to the symmetrically positioned outermost AP. The moment creates a stress variation through the thickness of the laminate as intended. The reading confirms the observations from the model, where the extent of delamination on the side in higher tension is larger. The variation differs between specimen series, depending on the length of the TZ. The largest moment occurs at the specimen edges with a minimum at the centre. Shorter TZs therefore have a less significant variation of strain than longer TZs in which the APs extend toward the ends of the specimen. Whether the actual predicted bending moment was achieved, depends on the response of the fixture to loading.

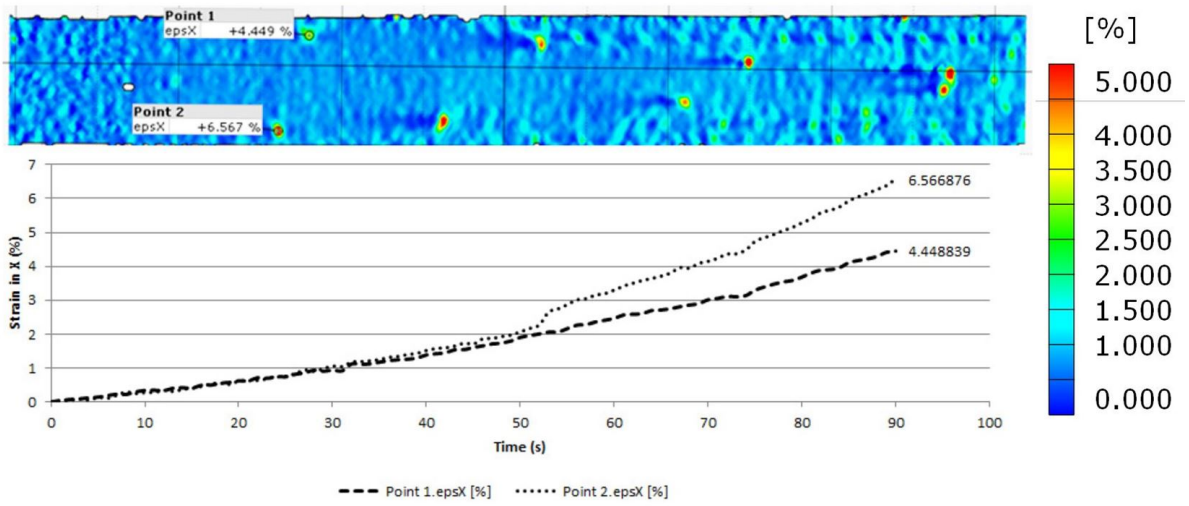

Figure 5.1: Strain variation at opposing APs in TZ1-5

The theoretical maximum out of plane deflection considering the whole apparatus according to equation 3.5 was expected to be approximately 10 mm. The exact value depends on the specific series bending stiffness and maximum failure load. From the DIC images a transverse movement of the specimen of about 5 mm can be read. Though this is movement after the pre-load of 1kN was applied, at which stage some rotation had already occurred. The pins will experience a frictional resistance to rotation under the tensile force. The actual bending moment in the specimen can be expected to be less than the theoretical value. Since it is ultimately the rotation which determines the induced bending moment and there are definite frictional losses at the pin. The use of strain gages at the mid-section of the specimen could give a better indication of the variation in stress due to the moment. Providing a better comparison than the transverse displacement and a check for the values obtained through DIC reported in figure 5.1.

5.1.2. Load/Displacement Response

Graph 5.2 shows plots of load versus displacement generated by the testing machine. Both measures are taken at the machine cross-head sensors. Plotted alongside are the FEM results with displacement and reaction force taken at the load introduction reference point. The FEM results show a reasonable fit, but there is a lack of correlation in the first 1 mm of displacement. Counter-intuitive effects are observed in this phase. The experimental plots exhibit a bilinear behavior. A softening knee is observed at around 5 kN of force with a linear response from thereon. The expected behavior follows more that traced by the FEM plot. The majority of transverse deflection due to bending occurs in the first few kN of loading. The result is a nonlinear ramp until a point at which no further bending is occurring, from which point the response is largely linear. The experimental curves are capturing behavior within the entire experimental setup. The specimens are partly loaded by bearing. Local deformation around the pin will be registered in the output, as will the fixture alignment, rotation and deformation. It is a speculative task of attempting to pinpoint the causes leading to the observed response. A correlation which omits the effects beyond the specimen boundaries is needed. The employment of such a method is discussed later in chapter 5.2.1.

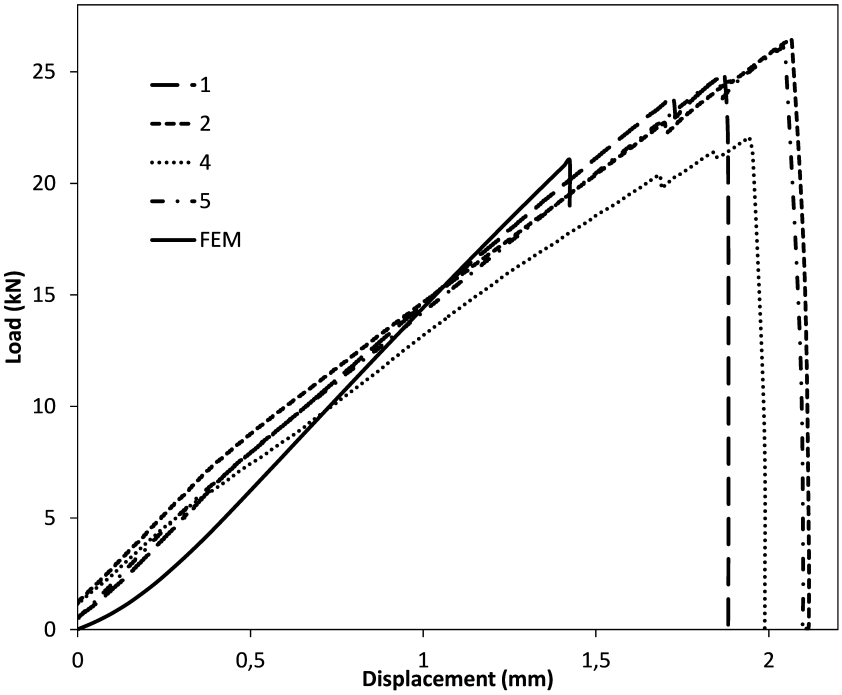

Figure 5.2: TZ1 Test data with FEM overlay

The test data for the remaining series are given in the appendix in figures 7.1 to 7.4. Plots of the mean final failure displacements and loads for each series are given in figure 5.3. Error bars have lengths of one standard deviation. The results of the full CFRP reference specimen are provided for comparison. The findings of the study of TZ arrangements by Petersen et al. [56] recognized the quasi-isotropic and UD reference laminates to outperform all locally hybridized specimens. This finding was not confirmed in the combined loading case. The advantage of an increased bending stiffness of the hybrid specimens likely contributed to lower stresses on the tensioned side in arrangements which did not suffer from the limitations of unfavorable TZ design. The relative performance of the individual series is discussed in relation to the FEM results later in this chapter.

5.1.3. Failure Identification by Microscopy

Post-failure microscopy analysis was done on the specimens in order to obtain a better understanding of the mechanisms leading to failure. The nucleation points for cracks were clearly the APs. This has been noted by previous authors and in the present case confirmed by observations such as that in figure 5.4. Curiously, the growth of the crack often did not result in a delamination of the steel layer at which the crack nucleated. Rather the crack would tend to progress through the neighbouring composite ply to the next steel-composite interface at which it would initiate delamination (figure 5.4 a)). This phenomenon was only observed at the four instances of steel foils neighbouring 90° plies. There is a much larger resistance to crack propagation through the 0° plies. Therefore if a crack grows in the direction of a 0° ply it will be stopped at that interface and grow into a delamination. Figure 5.4 b) shows this. Here a crack is growing both into the interface and through the neighbouring ply.

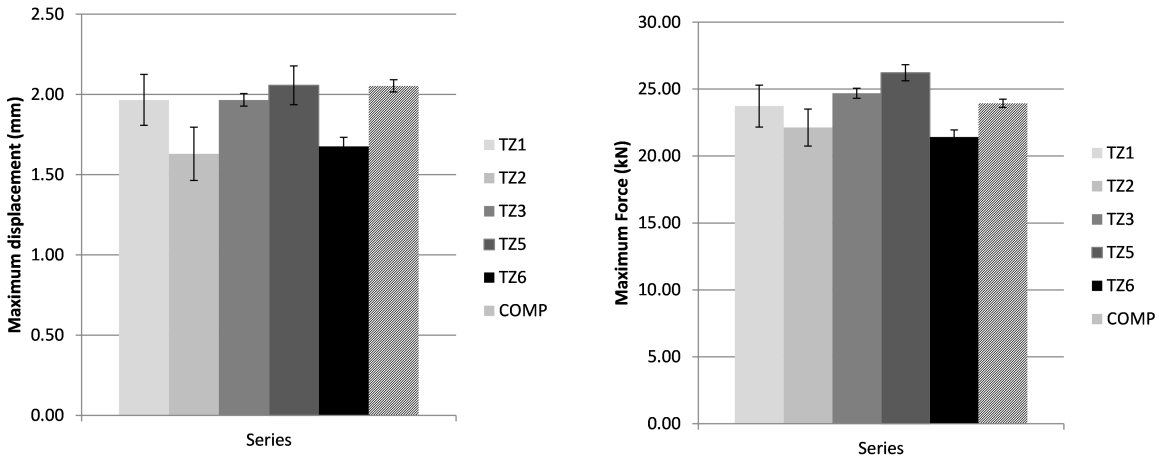

(a) Failure displacement

(b) Failure force

Figure 5.3: Comparison of average experimental series failure loads and displacements

These types of crack growth lead to the failures shown in figure 5.5. In Figure a) the delamination can be seen to be extending from the AP along the steel foil. According to table 4.1, the critical ERR of the Steel-0° interface in mode II is higher than that of the steel-45° interface. Naturally, the crack therefore initiates at the weaker surface. After progressing approximately 1 mm, the intralaminar crack goes through the neighboring 45° and 90° plies to reach the next 0° ply and continues along that interface. The initial growth of the crack in figure b) is through the adjacent ply. This growth is in mode I, for which there is a significantly lower critical ERR. The path of least resistance is for the crack to grow until the next steel layer before being stopped there, rather than causing mode II delamination failure directly at the AP interface.

As figure 5.6 a) illustrates, cracks did not necessarily initiate at APs. While the layers remain in cohesion at ca. 0.2 mm from the foil end, there is apparent separation further along its length. The initiation, growth and indeed presence of these cracks and delaminations using microscopy on unpolished surfaces proves to be unreliable. These separation between layers can be as small as $5\mu m$, as can be seen in figure 5.6 b). Such delaminations can therefore be present in varying extents without simply being detected.

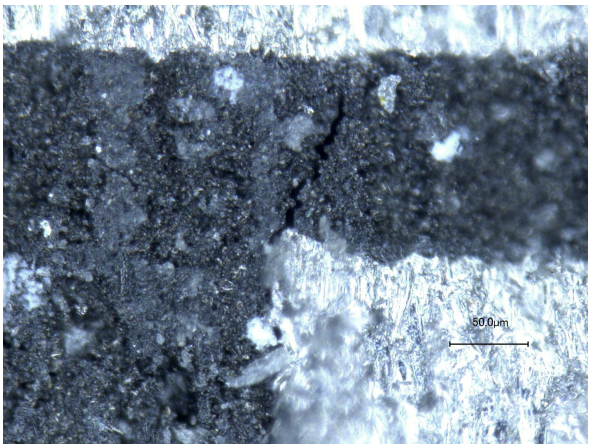

(a) AP crack growth toward neighbouring interface

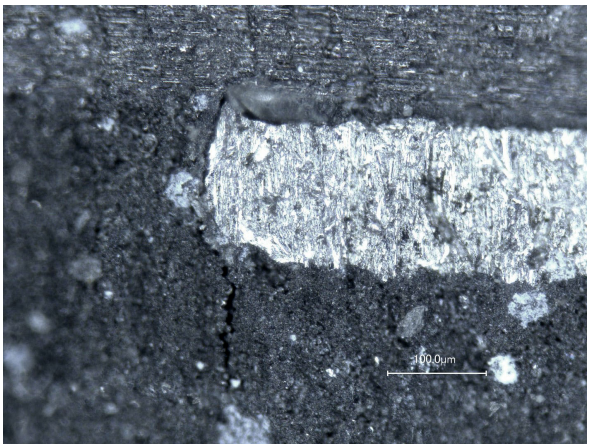

(b) AP crack growth combined with delamination

Figure 5.4: Crack growth at abutting points

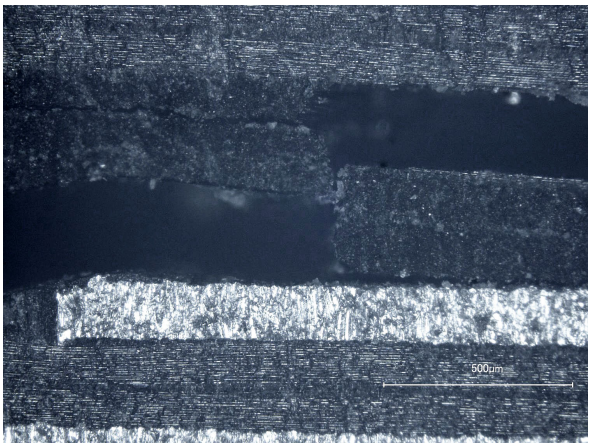

(a) Delamination growing through to next 0° ply

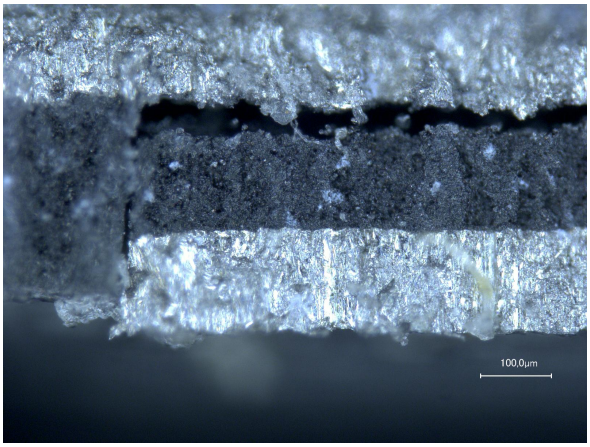

(b) AP crack growth to neighbouring metal interface

Figure 5.5: Crack growth through composite layers

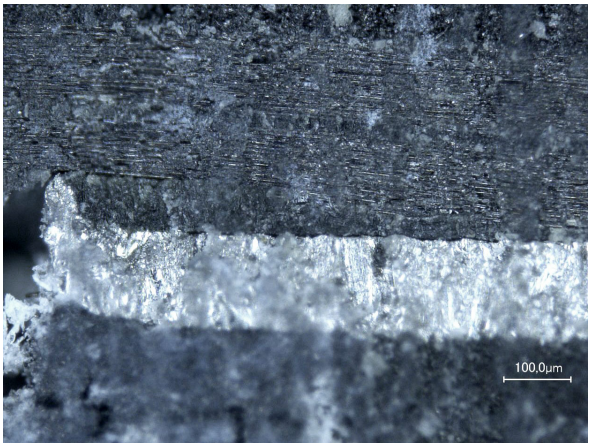

(a) Delamination not extending to foil end

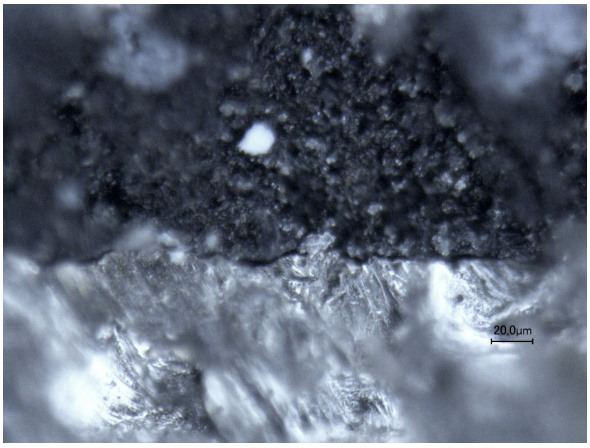

(b) Hardly detectable delamiantion

Figure 5.6: Delaminations not originating at APs

5.1.4. Strain Field Analysis with DIC

A high quality speckle pattern was achieved following the methodology outlined in chapter 3.5.1. Of the 40 megapixel image, approx. 3 megapixels were dedicated to the sprayed zone. Due to the high quality of the speckle pattern small 20x20 pixel subsets were used. At this subset size there were approx. 7500 subsets available for tracking, providing a good resolution.

Figure 5.7 shows a comparison of the original pattern and its loss after first specimen cracking. The pattern was effectively made by powder deposition with very low adhesion between the surface and the titanium dioxide and iron oxide particles. Cracking in the specimen caused the powder to be shaken from the surface and all subset tracking capability to be lost. The cracking occurred at around 80% of the ultimate failure load. The majority of the loading response was therefore successfully recorded, but the data before final fracture where major delamination growth would be observed was not available.

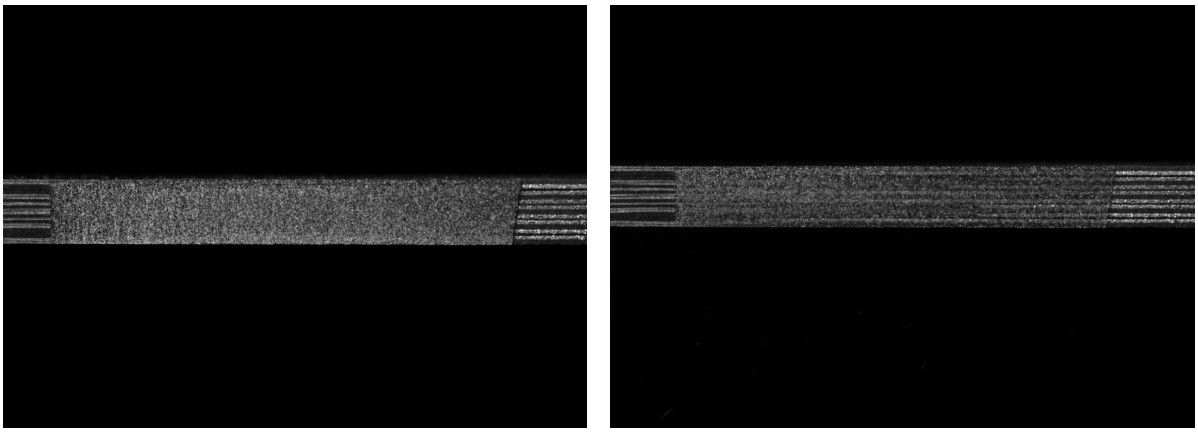

(a) Virgin speckle pattern (b) Speckle pattern after specimen cracking

Figure 5.7: Loss of spleckle pattern due to specimen cracking

Two useful outputs were taken from the correlation processing software. The longitudinal strain (x direction) and the shear strain in the xy plane. Figures 5.8 and 5.9 show an example output for the TZ1-4 specimen at the latest recorded stage. The visualizations of these variables for a representative specimen from the rest of the series are given in figures 7.5 to 7.12 in the appendix. The legends were set in the ranges from 0% to 5% for longitudinal strain and ± 0.05 and 5° for shear strain and angle. Locally longitudinal strains reached values up to 10% and shear strain up to 0.1. The range was limited with the intent of accentuating the areas of stress concentration.

The strain concentrations are clearly visible in figure 5.9 at the locations of the APs. Naturally it is also here where most delaminations originate, as has been observed in microscopy images. The novelty in this type of stress concentration observation using DIC is in mapping the extent of the concentrations and the possible stress interaction. Figure 5.9 is a good example of this. The two leftmost APs lie approximately at the same location in the x direction and are separated by two 0° layers in y. There is a third strain peak present between those at the APs. Presumably this is a result of the vicinity of the two APs and their stresses interacting.

Strain peaks at the APs results in zones of the metal foils behind the APs to be in a state of lower

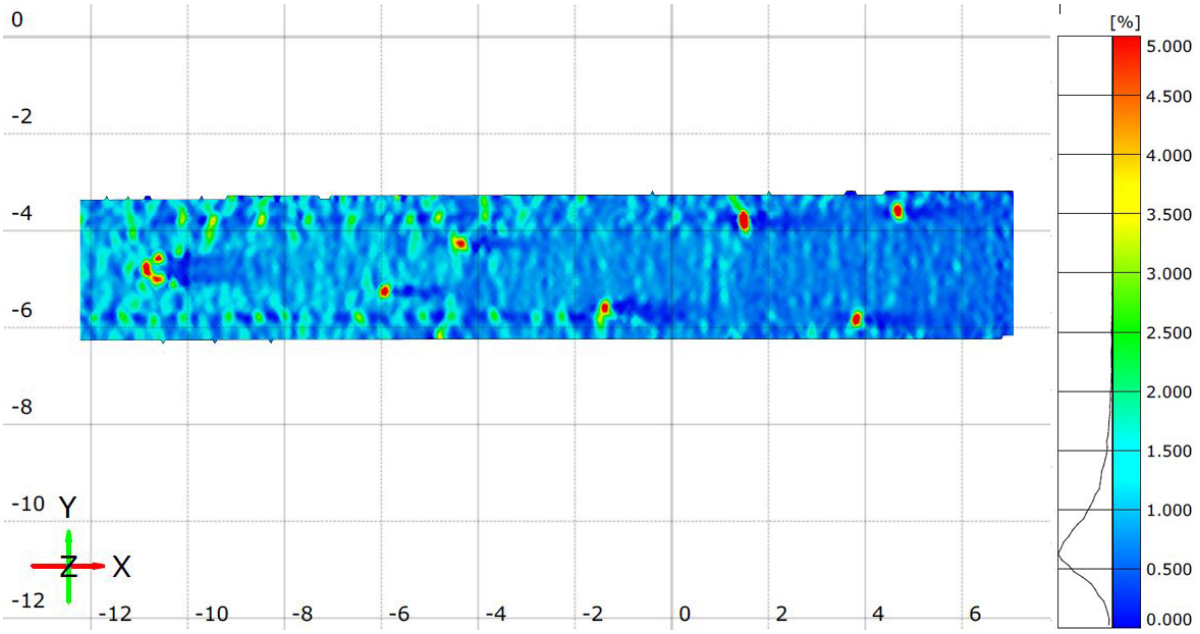

Figure 5.8: TZ1-4 Longitudinal strain in x

strain. These show up in figure 5.9 as deep blue trails to the red strain peaks. The strain mismatch at the interface of the adjacent composite plies along these lengths results in shear strains, which are visualized in figure 5.8. Whenever the value of the shear stress in these zones exceeds the shear strength of the interface, delamination will occur. The extent of the delaminations is not necessarily limited to the extent of the regions highlighted in the shear field. More so that these zones serve as delamination initiation points. There seem to be no interactions longitudinally between the individual shear zones. This could be due to delaminations not extending far enough at this stage of loading. Or that fine interlaminar crack growth simply cannot be visualized with this method.

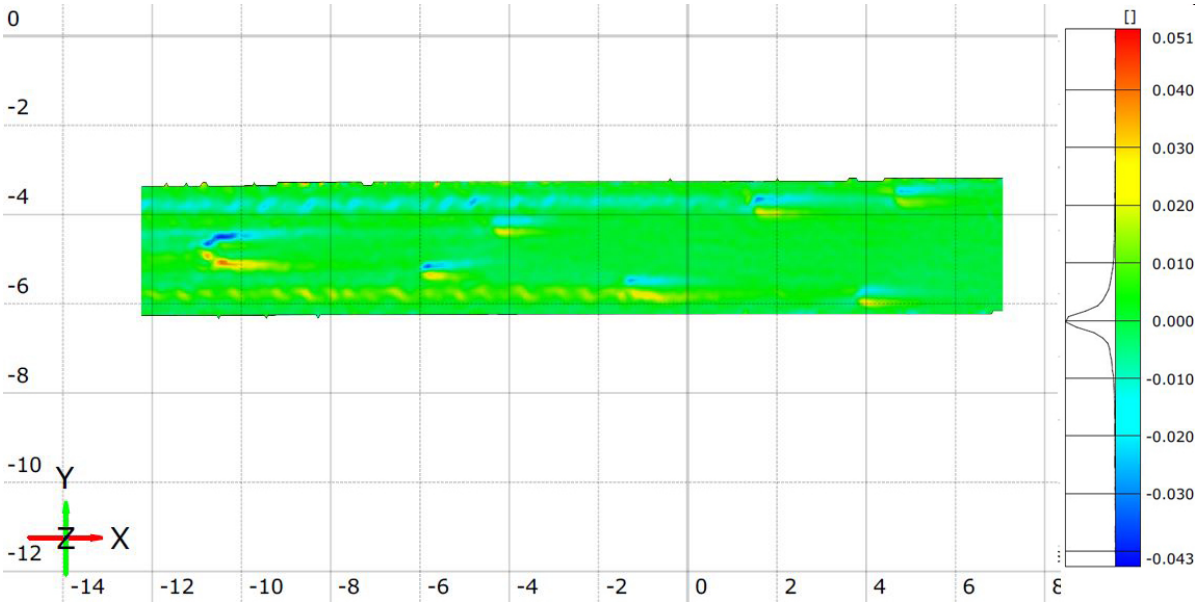

Figure 5.9: TZ1-4 Shear strain in xy

5.2. Numerical Results

5.2.1. Model Correlation

It has been discussed in section 5.1.2, that a correlation of the overall displacements is not a valid one owing to the hardly characterizable deformation effects of the apparatus. An alternative method is a more local comparison. A local elongation of the specimen can be calculated by taking the displacement at two boundary points. The displacement along an equivalent section of the specimen in the FE model should match. The section chosen for the comparison was the approx. 20 mm long stretch shown in fig 5.9. The data could only be compared to the extent to which the DIC measurements were available. The premature loss of the speckle pattern occurred for the TZ1 specimen correlated in figure 5.10 at a load of 15 kN, which translates to around 1 mm of global displacement. There is a close match between the two results at this early stage of loading. DIC analysis strongly indicates delamination at this stage of loading, which is supported by the model results. Even though there is a slight divergence of the curves, the trend remains consistent, indicating that the effect of the growth of delaminations is being captured by the model. Convergence can be further studied even more locally. This is done in the subsequent section in terms of delamination and damage criteria.

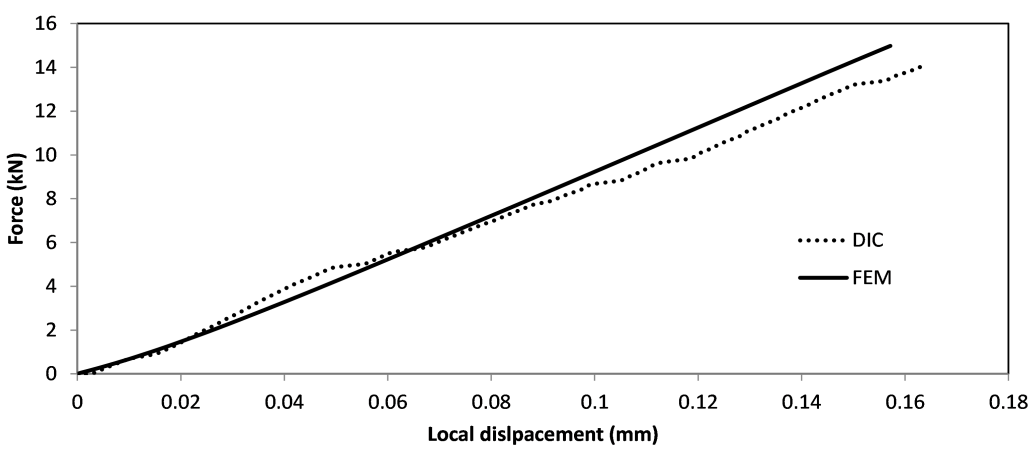

Figure 5.10: Local model correlation of DIC and FEM displacement of TZ1-4

5.2.2. Failure Mode Identification

Delamination

It has been discussed in section 5.1.3, how cracks were initiated and the mechanisms leading to larger delamination. Most times the failure locations were more numerous and the sequence of failure events from these images is unrecognizable. DIC data can only give indications toward the initiation of failure, but not final failure due to the loss of the pattern. These tools can be used as hints toward telling which APs were locations for the first crack and delamination formation and at which interfaces catastrophic failure finally occurred. These locations might not be coincident due to the more complex behavior such as cracks jumping through layers. The numerical outputs that can be correlated with these observations are the quadratic traction criterion mapping delam-

ination extent and the failure criteria index values recognizing the modes of failure listed in section 4.2.4.

The very first delamination occurs at the cohesive surface defined at the APs. As shown in figure 5.11, the delamination initiates at the foil corner/edge. From there delamination and full separation of the AP surfaces quickly follows. Once the AP surfaces have separated, the separation continues by a delamination of the steel foil from the adjacent composite layer. This behavior reflects that observed in microscopy images, particularly figure 5.4. What the model is not able to explicitly show is the related finding, that cracks born at APs tend to grow through the thickness of adjacent layers. There are indications of this by the locally increased matrix failure indexes FM3 and FM5 in the neighbouring plies. Nevertheless the failure indexes do not reach anywhere near 1 in this early stage of loading.

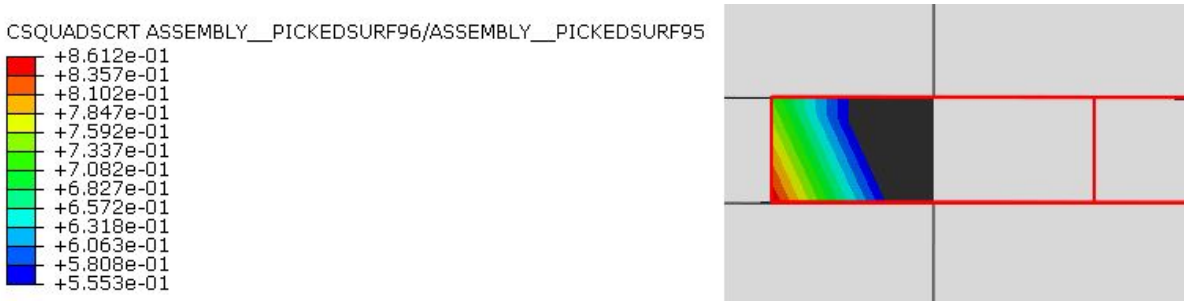

Figure 5.11: First separation at AP initiating at foil edge

Even though the model does not capture crack growth through the thickness of plies, there is an effect of the APs on the delamination of neighbouring steel-composite interfaces. The linearly staggered pattern of TZ1 in figure 5.12 illustrates this effect well. Here, where the specimen is in the stage of final failure, there is extensive delamination extending from all APs. However, there are also areas where the damage criterion is elevated further along the foil length, namely at the longitudinal positions of the other APs. The value of the damage criterion along the lengths of the longest foils is plotted in figure 5.14. Spaced at 5 mm, there is a clear effect of the neighbouring APs on the delamination tendency at these intervals. There is a critical peak at the position of the second AP, and a slight elevation at 10 mm. At 15 mm there is no significant effect.The fact that the peak does not decay to a baseline level between APs indicates that there is an occurring interaction. The interaction of the stress concentration at the first and second APs is a result of the longitudinal vicinity, but also of the through thickness distance. The two longest foils are separated by one ply only (0.13 mm). The effect of this interaction is analogous to the crack growth through adjacent plies. Though only at interfaces where the AP is neighboring a 45°or 90° ply. In the TZ1 pattern this occurs only at the position of the 90° ply in the layup, but in more complex stackings it is far more common.

The effects of interactions both due to the longitudinal and through thickness vicinity of APs are also apparent in the arrangement of TZ6. The delamination extent before failure is visualized in figure 5.13. The APs in this arrangement are aligned on two fronts. The multiple stress interactions lead to delaminations on average extending further than those in TZ1 and any other TZ. The DIC image of shear strain in specimen TZ6-5 in figure 7.11 also shows higher levels of shear strain and

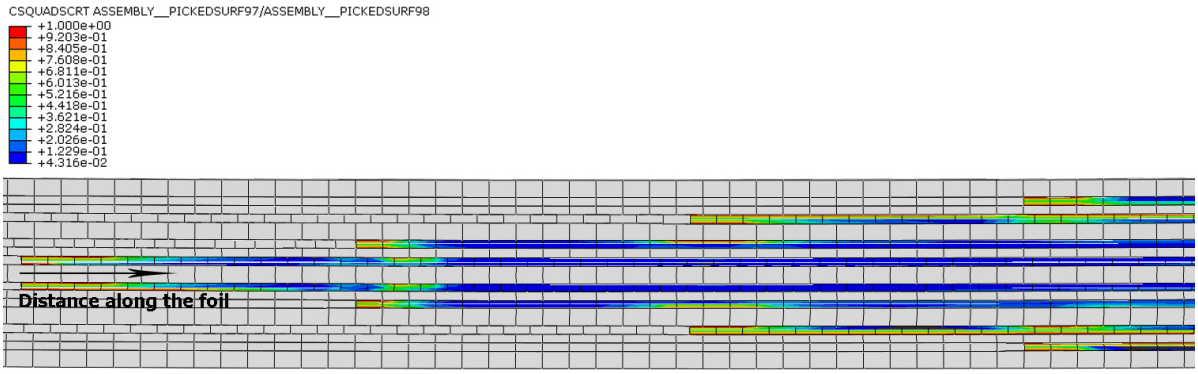

Figure 5.12: Delamination visualization with the quadratic traction criterion

length of extent compared to other TZ DIC images. It is clearly the arrangement in combination with the step lengths chosen, which determine the strength of the TZ.

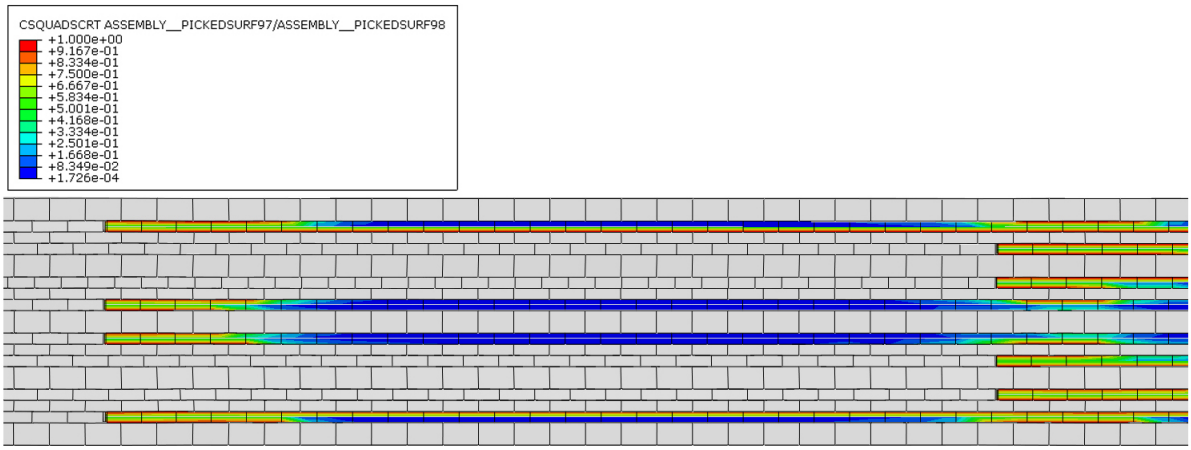

Figure 5.13: Delamination visualization with the quadratic traction criterion

The extent of the delamination is clearly much larger than indicated by the shear strain DIC output in which there is no interaction between the APs and adjacent interfaces. The microscopy images confirm that delaminations extend further and there is a coherence between microscopic observations and FEM delamination lengths. The delaminations on the side of the specimen in greater tension are longer. This is an effect seen in the DIC shear plot and delamination visualization. The difference is significant enough to also cause final failure on this side of the specimen.

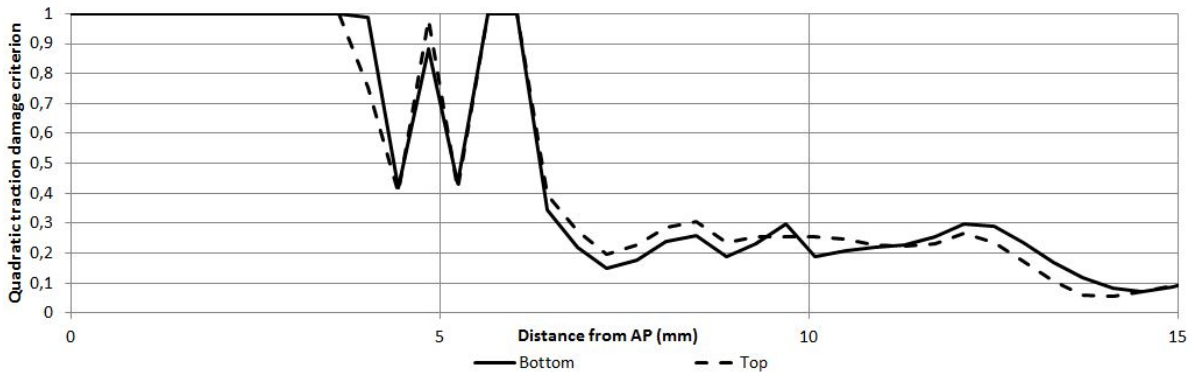

Figure 5.14: Damage criterion indicating delamination along long TZ1 foil (path shown in figure 5.12)

Intralaminar Failure

Of the failure modes recognized by the Cuntze criterion, the ones of interest are FM1, FM3 and FM5. Tensile matrix damage is reported at multiple locations throughout the TZ. Figure 5.15 shows a mapping of the FM3 index at final failure. The failure criterion is satisfied at and around the APs, and largely throughout the 90° ply and to it adjacent 45° ply. The same regions report shear damage. These effects can be seen in the DIC images. Spots of increased longitudinal strain and shear bands are visible in figures 5.9 and 5.8. In bending, the outermost foils experience the largest peeling stresses. In the given arrangements, the outer foils also neighbor 90° plies, which are the most vulnerable to matrix damage. Consequently, in all arrangements there is failure in the 90° ply and full delamination of the adjacent foil.

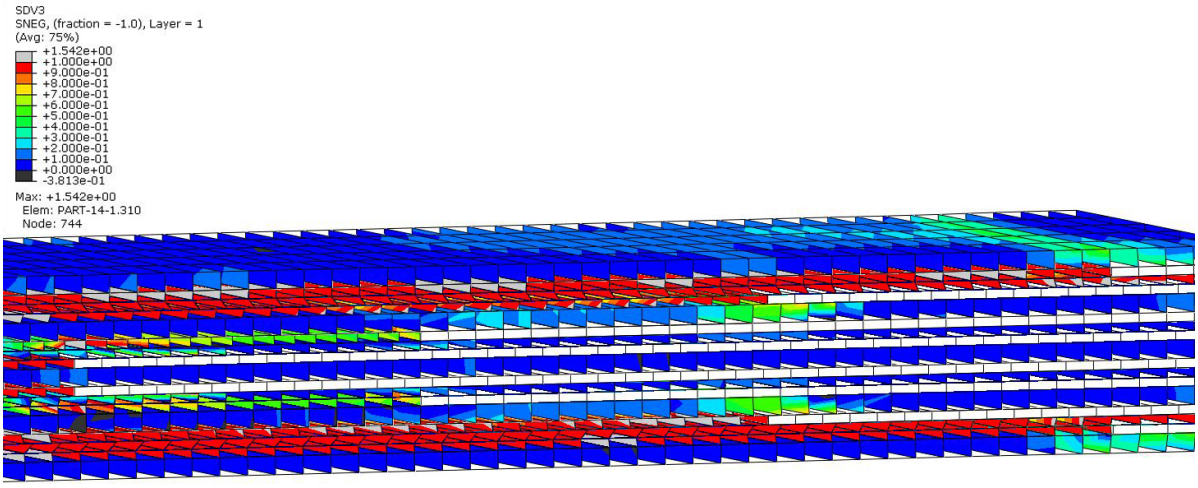

Figure 5.15: TZ1 matrix tensile damage failure mode index

The matrix failure at this location is guaranteed in all cases and is essentially the precursor to ultimate failure. The load carrying capacity of the outer layers is severely diminished by the full delamination and matrix damage. The delamination and matrix damage extent are fairly equivalent on both sides of the specimen. The stress concentration at the outermost AP causes tensile failure in the outermost 0° ply. This occurs expectedly first on the side with higher tension. Failure at this location was observed in all TZs except TZ1. An output of the FM1 index in TZ2 is visualized in figure

5.16. There is clear fiber damage at the bottom 0° plies. In the visualizations of FM1 in other TZs provided in the appendix the damage is less significant, but reliably present in the same region. The exception to the first 0° ply failure location is TZ1. Figure 7.13 shows that it is instead the central 0° layers, which experience initial damage. However the FM1 index is also close to 1 in the bottom 0° layers, which will likely be he next to fail. First fiber failure is crucial though, since full failure of the specimen ensues after the first rupture of a 0° ply.

Though metal plasticity was modelled, the plastic strain in the metallic layers was practically zero. The regions with stress peaks tended to delaminate, rather than transferring the load into the specimen to cause plasticity. Failure occurred before tensile strains in the fully hybrid section of the specimen reached plasticity limits. The lack of plasticity is consistent with the experiments of Petersen et al. [56], in which plasticity was only present in the fully hybrid specimen.

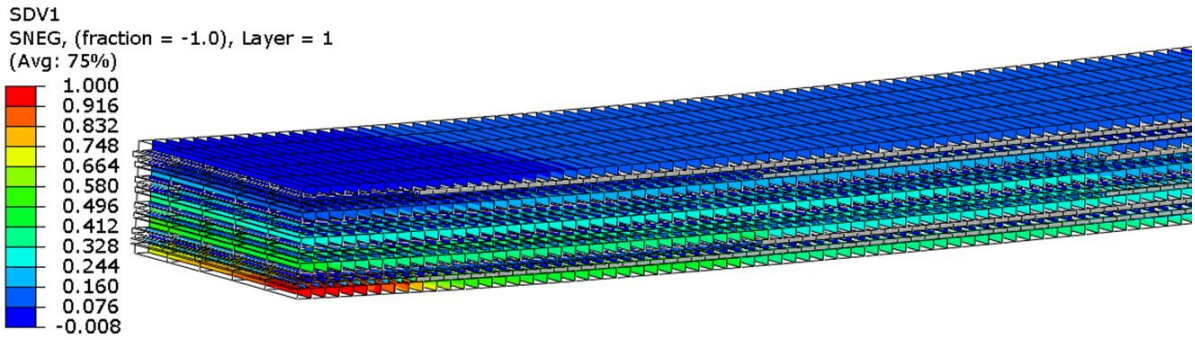

Figure 5.16: TZ2 Tensile fiber failure mode criterion visualization

5.2.3. Predictive Capabilities of the Model

The failure loads from the model for the individual TZs are compared in figure 5.17. The percentages above the bars indicate the percentage deviation from the mean experimental failure loads 5.3. Both the displacement and force at failure from numerical results were lower for all TZs. The maximum force was used for the basis of comparison, since it is less influenced by the deformation effects of the tooling. The failure forces are lower in the range of 12% to 21%. Values trending overall lower suggest a systematic discrepancy between the model and test. Section 5.1.1 discusses the likely causes for a lower than predicted applied bending moment. A reduced bending moment to tensile force ratio would result in a higher tensile failure force. These effects are absent in the model where the full moment is applied and subsequently failure forces are lower. Since the error is systematic, there is still a match between the relative performance between the individual TZs. The arrangement failing at the highest force is TZ5, followed by TZ1 and TZ3. TZ2 and TZ6 fail at a load compared to one another and lower than the other three.

The manufacturing imperfections described in section 3.4.3 will also have an effect on the ultimate failure load. It is expected, that the presence of foil burrs and ply overlaps would decrease the failure load. The other imperfection resulting from inexact manual cutting of the foils was illustrated by figure 3.9. The steel layer were therefore not perfectly aligned, resulting in unintended spacing between some APs. The mechanisms by which stress interactions at APs are significant in reducing the TZ strength have already been discussed. Reducing these effects by unintentionally

spacing the APs would lead to an increase in the failure force and contribute to the discrepancy observed in figure 5.17.

The TZ4 pattern was also simulated. TZ4 is a single step distance ordering, just as TZ6, but inverse in it's arrangement - long foils in TZ6 are short in TZ4. Therefore where TZ6 has a long foil at the outermost position, the outermost foil in TZ4 is short (3.9). The failure forces of the two series are comparable, with TZ4 performing marginally better. The relative superiority of TZ4 is a good illustration of the points discussed in the previous section. A long foil further out in the laminate experiences larger peeling forces. The matrix damage in the outer composite layers will consequently occur sooner, leading to a an earlier failure in the outer 0° plies. The vicinity of the AP to the outer higher stressed 0° plies in TZ6 also contributes to earlier failure by having a stress concentration point closer to the point of critical failure.

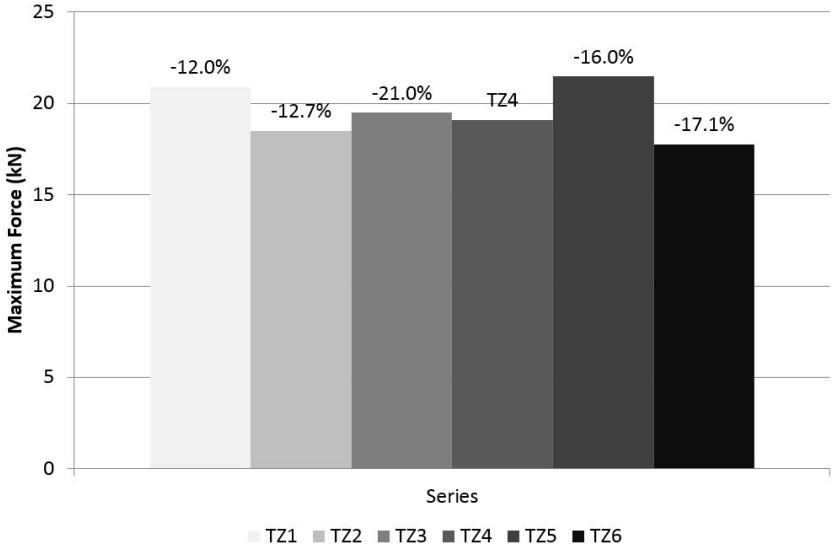

Figure 5.17: Comparison of ultimate failure force across TZs from FEM results with deviation from experimental values

5.2.4. Variation of Step Distance

After identifying the best performing arrangement, the model can be further used to investigate the effect of altering the step length. TZ5 models of various TZ step lengths were run. Results with step lengths of 2 mm longer and 1 and 2 mm shorter are compared with the original design in figure 5.18. Reducing the step size resulted in a significant decrease in the strength of the TZ. A step length reduction from 10 mm to 8 mm lowered the failure force by 25%. Shortening the metal foils amplifies the interactions between the APs, as discussed in the previous section. On the other hand a 1 mm increase in the length also did not increase the failure force. In fact, a longer TZ lead to a decrease in the overall strength. The bending moment increases away from the center of the specimen. The further the APs extend, the higher the peeling forces on the outer foils. A TZ reaches its highest strength when a balance is found between step lengths being long enough, so that there is no interaction, and the TZ being compact, so that the peeling stresses are felt less by the outer foils. The second point to this balance is very specific to the present specimen length. In longer specimens, where the moment increases more gradually the effect is less significant. The task would then be

simply to find the shortest step distance where the overall strength is still not affected by stress concentrations from the APs. This length might be different for different arrangements. Step lengths also do not have to be constant throughout the TZ. Doing a true evaluation of the most favorable combination of arrangement and step length would require a more complex selection algorithm.

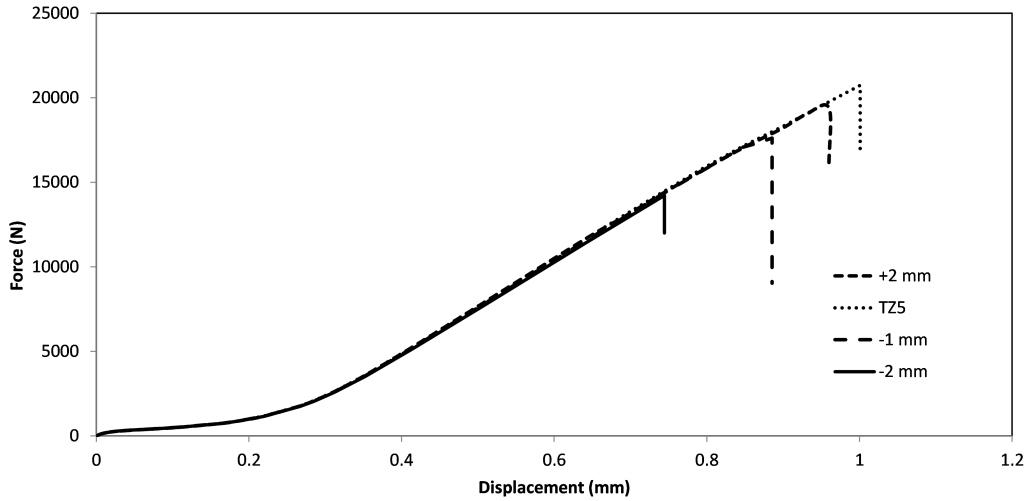

Figure 5.18: FEM results for TZ5 with varying step lengths

5.3. Relation of Results to the ATLAS project

The methodology described in the thesis has been successful at relatively evaluating the strength of varying TZ arrangements. Both testing and simulation was done on a reduced laminate, however it can be used with just as much validity for more extensive layups.

Assuming that the ATLAS base laminate described in section 2.5.1 cannot be rearranged, the highest achievable MVC is 25%. With this arrangement, only ±45° plies can be substituted. This means that there must be two positions in the laminate where ±45° plies are substituted surrounding an uninterrupted 90° ply. Extensive matrix damage of adjacent 45° and 90° plies has been shown in this thesis to be a major event toward ultimate failure by fiber failure. One half of a possible TZ arrangement based on the findings in this chapter is suggested in figure 5.19. The initial spacing length suggestion is 10 mm. The outermost foil is kept shortest to avoid very early damage of the outer three angle-plies. The sixth and eighth foils are the longest, but spaced by three step lengths to forego any longitudinal interactions. The pair of foils 13 and 14 are only spaced by two lengths, as the stresses due to bending are less severe further toward the center-line of the laminate. The innermost three foils experience the lowest stresses, do not contribute to the bending stiffness and are spaced in the through-thickness direction by 3-4 plies. These foils are kept short, and can be of equal length due to the large spacing distance.

Such a TZ described here can be used as the starting point to a more complex optimization. It is based on the qualitative findings of this study, which are by themselves hardly transferable. Without numerical validation, the design of a TZ is more of an art than a science. As noted previously, an

algorithmic evaluation with iterative simulation is needed, in which the step lengths are adjusted and reordering performed.

10 mm	20 mm	30 mm	40 mm	50 mm	60 mm
1		45			
2		90			
3		-45			
4		0			
5		0			
6		-45			
7		90			
8		45			
9		0			
10		0			
11		0			
12		0			
13		45			
14		90			
15		-45			
16		0			
17		0			
18		0			
19		0			
20		-45			
21		45			
22		0			
23		0			
24		0			
25		0			
26		45			
27		0			
28		0			
29		0			
30		-45			
31		0			
32		0			

Figure 5.19: Suggestion of an ordering for the ATLAS laminate with an initial spacing of 10 mm

5.4. Discussion Summary

The load carrying capacity is related to some general sequences of failures and relations between occurring failure types. Very initial failure occurs at the steel and CFRP ply abutting edges. In tests, the crack from this location has a tendency to grow into the neighboring ply and continue until the next 0° or steel layer. A comparable effect is observed in the model, where through-thickness vicinity of an AP to a steel interface initiates delamination at that interface.

Delaminations extend from all APs at varying lengths, depending on the relative position of the APs. Both longitudinal and through-thickness vicinity of APs result in interactions of the stress concentrations at the APs. The through-thickness spacing is determined partly by the base laminate, which dictates which layers can be substituted. The longitudinal spacing is a design choice, which influences the overall TZ performance. The step distance can be increased to a point where longitudinal interaction is eliminated. Elongation of the step length past this point yields diminishing returns.

The failure sequence of events described in this chapter is illustrated in its completeness in figures 5.20, 5.21 and 5.22. The figures show matrix damage, fiber damage and delamination of the longest foil neighboring the 90° ply. This illustration of events is presented specifically on the model results for TZ5, but can be generalized to the other orderings as well. Intralaminarly, the first matrix damage occurs in the 90° layers and the 45° layers neighboring them at a load level of approx. 11.7 kN. This stage is illustrated by the outputs in figure 5.20. The delamination at the neighbouring foil is relatively short in the extent of $< 2mm$ at this stage. Though the effects of an interaction can be seen at the location of the neighboring AP, initiating delamination at a second point. The exact TZ arrangement determines whether the full foil delamination will occur at the outermost or second outermost foil. If the longest foil is positioned at the outermost position, the first delamination happens there at a lower load due to the increased peeling stresses. The maximum fiber damage criterion at this point is far from critical at 0.366.

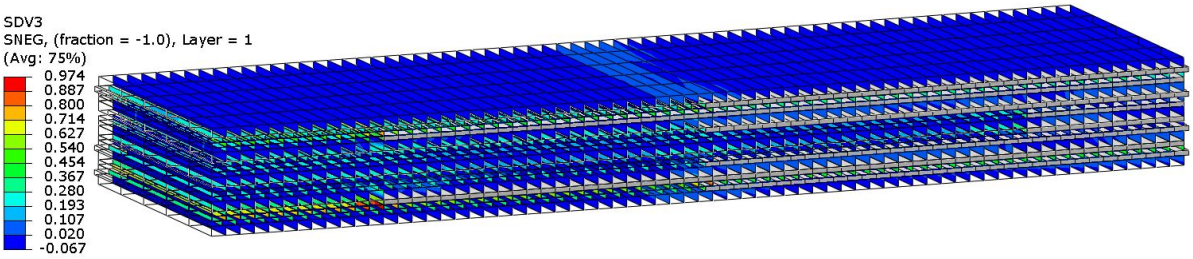

(a) Matrix damage

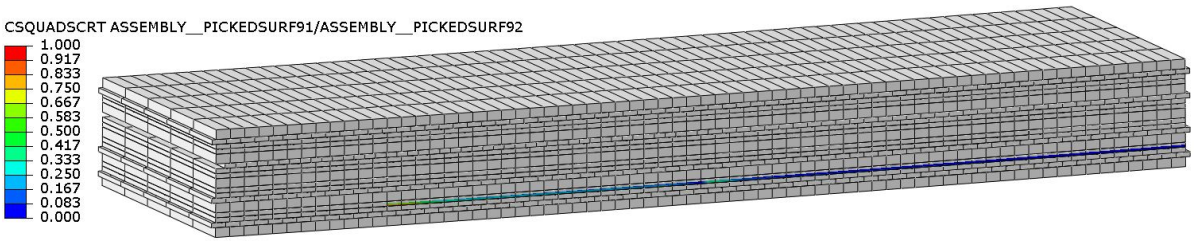

(b) Quadratic traction damage criterion

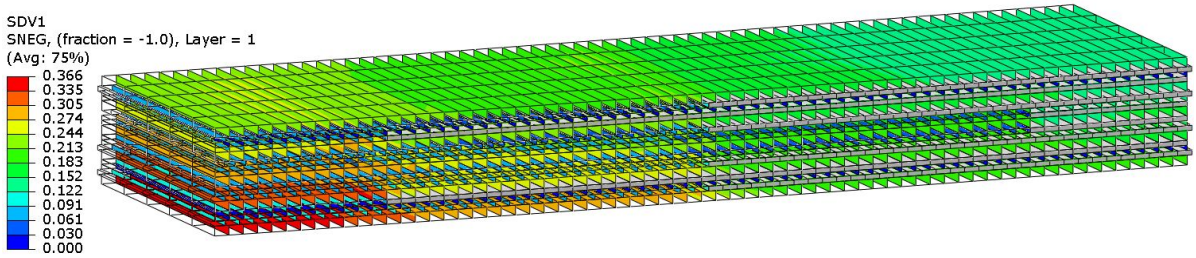

(c) Fiber damage

Figure 5.20: State of damage at 11.7 kN of loading

The state at the next stage of loading at 14.5 kN is illustrated by figure 5.21. At this point the matrix damage has spread entirely through the 90°and 45° layers. Within the additional 3 kN of loading from the previous stage, the delamination has spread far along the length of the foil to merge with the delamination at the second AP. Seeing as the matrix damage has just occurred, the fiber damage is still not critical at this point.

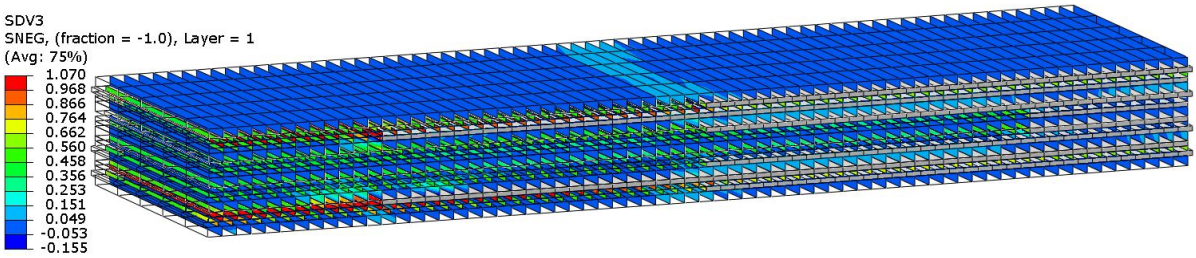

(a) Matrix damage

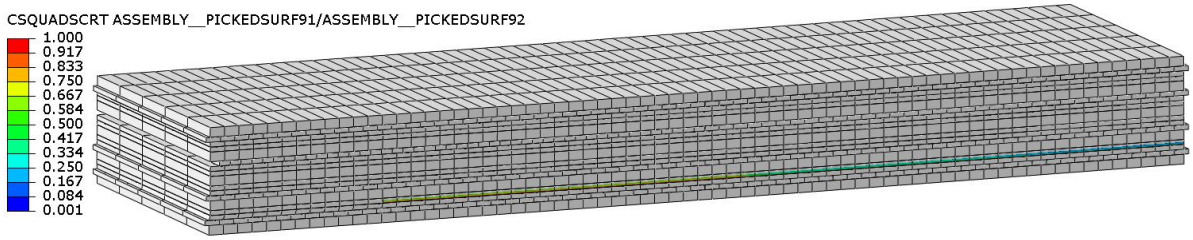

(b) Quadratic traction damage criterion

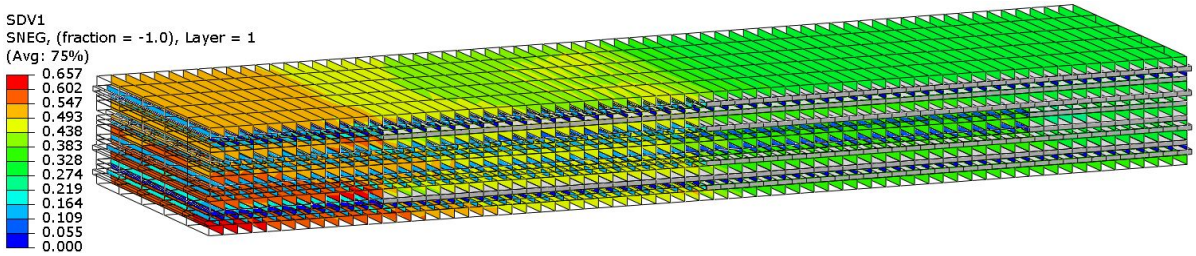

(c) Fiber damage

Figure 5.21: State of damage at 14.5 kN of loading

The fiber damage criterion quickly increases until the next stage. At 20.7 kN ultimate failure occurs in the 0° layer on the side of the specimen in higher tension. In all of the TZs except TZ1, the first 0° ply failure occurred in the edge layer. In TZ1 this first failure happens at the middle 0° plies. After first 0° ply failure occurrs, the residual load carrying capacity is lost.

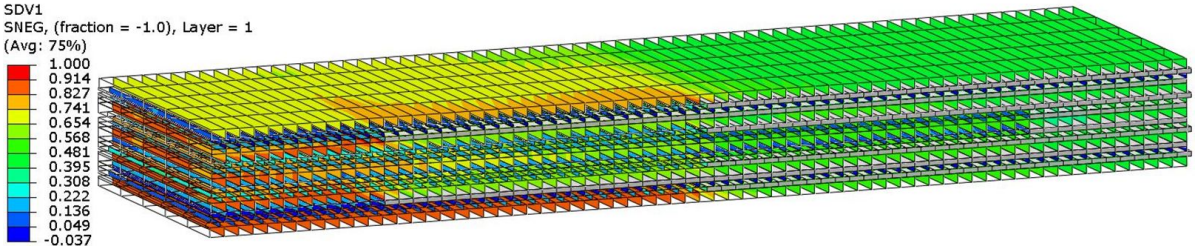

Figure 5.22: Fiber damage leading to ultimate failure at a load of 20.7 kN

There are essentially two groups of comparably performing TZs; TZ1, TZ3 and TZ5 performing by up to 20% better than TZ2 and TZ6 specimens. Not coincidentally do series TZ2 and TZ6 have their longest steel foils at the outermost position. The comparison between the inverse arrangements TZ4 and TZ6 underlines the contribution of positioning long foils at the outside to earlier failure. An interesting effect is exhibited by the short-long-short series TZ3 and TZ5, which have

their longest foils at the second outermost position, yet they reach the highest loads. The effect is attributed to a balance of placing long foils at the outside to achieve a higher bending stiffness, but not too far to be early initiators of full delamination and failure.

6

Conclusion

Experimental results showed, that the method designed for combined loading testing was suitable for applying a through-thickness varying tensile stress. Though the resultant moment is likely lower than that calculated by equation 3.1. Further investigations would be required to quantitatively express by how much the calculated and expected loading differs. Nevertheless DIC analysis confirmed the variation in strain through the specimen. The DIC results are further useful in identifying delamination nucleation points. Microscopy imagery of these points confirmed the foil APs as the nucleation sites for delaminations and cracks, which were likely to grow intralaminarly through the thickness. Extensive delamination can be expected to extend from all APs in the TZ.

The global behavior of the model deviates from the experimental results in absolute terms between 12 and 21%, but relative trends can be seen. Inefficiencies in the tooling and imperfections in the TZ arrangement lead to higher experimental failure loads. In this respect, the model provides conservative results. Nevertheless, due to the lack of global correlation, ultimate failure displacements and forces obtained from the model must be critically evaluated. However it is possible to carry out a more accurate local load/displacement correlation instead for FEM validation purposes. Besides correlating based on the load/displacement response, the model was capable of capturing delamination growth as a result of stress interactions. APs spaced too closely lead to stress interactions and earlier failure.

The matrix failure is first recognized in weak layers. Combined with delamination at the interface of those layers, the strength of the specimen is significantly reduced. The event leading to final failure is fiber damage. Fiber failure is likely to occur in the stress peak around an AP at the closest 0° ply to the zone of matrix damage.

A comparison of the experimental results for the individual TZ series shows significant differences in the average forces reached. A closer identification of the failure sequence of events using the model results is telling of the properties of a good TZ design specific to this layup. Long foils at the outside of the laminate increase the bending stiffness of the laminate. However the longest foils should be kept away from the very outside of the laminate, since this leads to premature delamination and matrix failure. APs should be spaced through the thickness of the laminate by as much distance as possible. A spacing of 5 mm lead to extensive interaction, while extending spacings past 10 mm can in fact result in weakening of the TZ. The exact ideal spacing is specific to the TZ arrangement.

Even though a prediction of the absolute results could not be achieved, the model can be used to make relative comparisons between TZs. The model is set up as a tool for further simulations, which can be aimed at investigating further orderings for increasing the ultimate TZ strength. A

method for simple TZ design improvement can be firstly to choose of a pattern from a pool of self-selected designs. The initial designs can be based on the guidelines from this thesis. Their strength can be evaluated using the model. For the best performing pattern, the model can be further used to iteratively find the minimum step distance between the APs, at which stress interaction does not occur. By following this methodology, an efficient TZ design can be chosen, ensuring that the TZ does not become a weak point of the structure and the locally hybridized joint can reach it's full bearing strength.

Recommendations for Further Work

- The potential for using DIC for more extensive correlation was set back by a loss of the speckle pattern at loads far before ultimate failure. The powder deposition method was suitable for achieving a good resolution, but failed to provide a durable pattern. Spray paints instead of powders can be used to produce the pattern. Some of the resolution might be sacrificed, but this might be an acceptable trade-off for extending the measurement to the entire test duration.

- A reduction in the friction in the pins of the fixture by the use of different lubricants can lead to a better correlation between the analytical and actual moment applied during the test. Measuring stress using strain gages at the laminate mid-section can give a better idea of the actual moment in the specimen.

- The model has been proven valid for a combined loading case of a given loading ratio. Experimental data from Petersen et al. [56] can be used to validate the model on the constitutive single load cases of pure bending and tension. On the other hand, the validity of the model can be tested on unrelated load cases, such as pure torsional loading.

- The model capabilities can be further extended by including some of the effects which were not considered in this model design:

  - The modelling of residual stresses, which have been shown to influence properties of hybrids can be considered. For example by the addition of a global temperature load.
  - Cohesive surfaces can be extended also to composite interfaces to better understand the extent to which through-thickness crack growth can be observed.
  - Considerations of more complex material properties, such as nonlinear shear behavior, the orthotropy of the steel foil or an improved degradation method (with more degradation steps).

- The process of improving the TZ design in this thesis is valid, but simplistic. There are several variables and interactions between them, which influence the quality of the TZ design. To truly reach an optimum design, a neural network with a genetic algorithm can be implemented for identification of patterns and TZ optimization.

7

Appendix

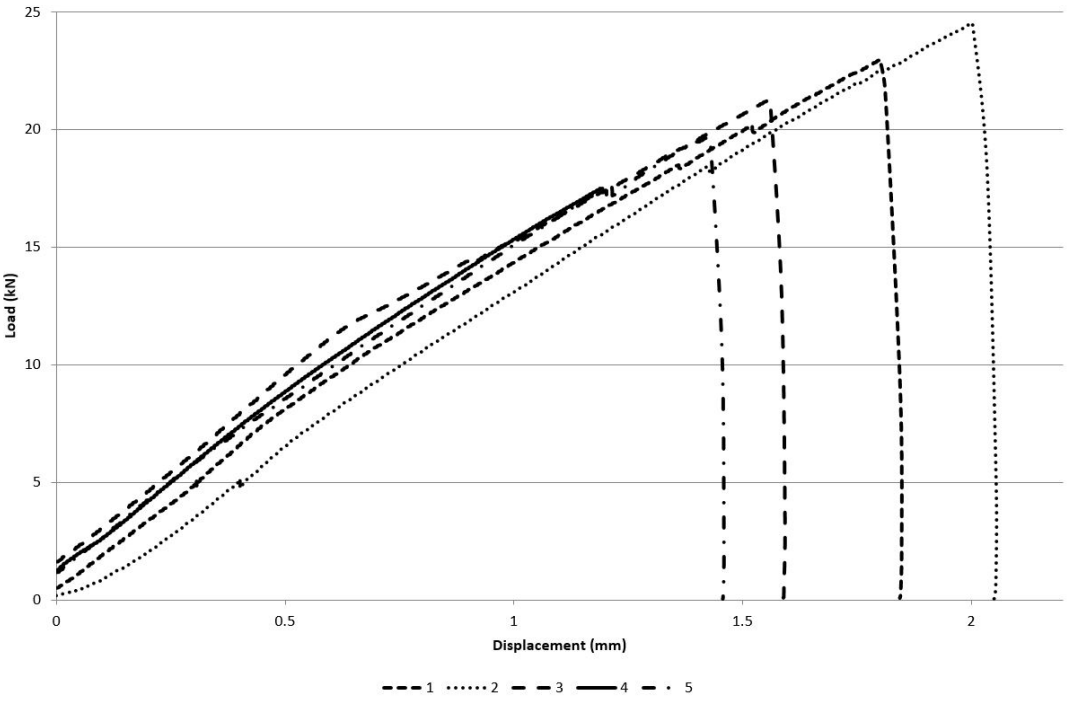

Figure 7.1: TZ2 Machine force/displacement output

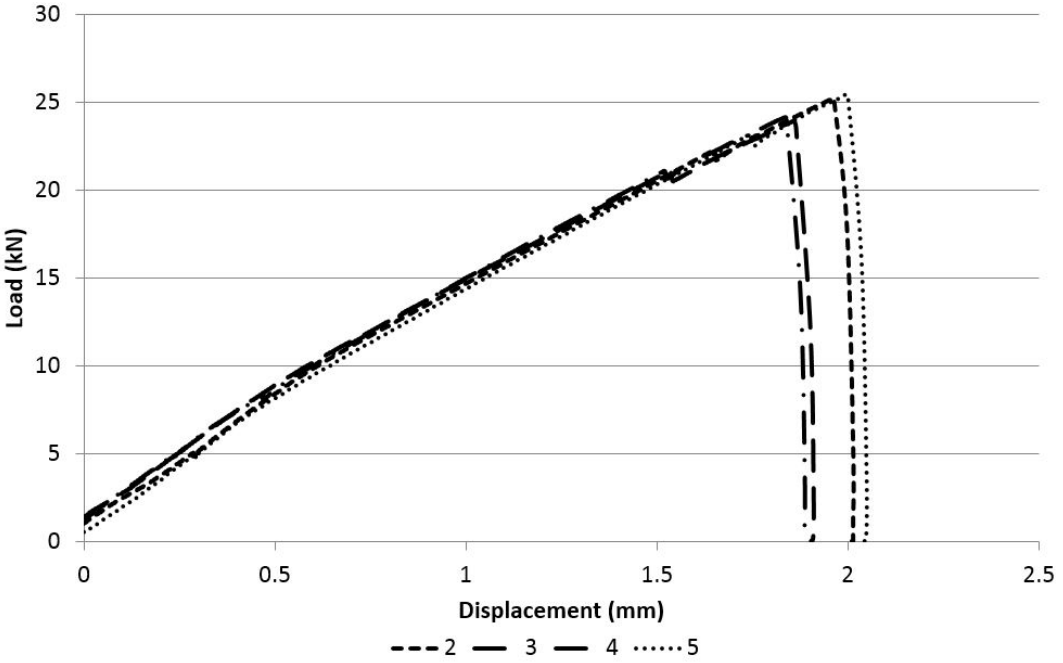

Figure 7.2: TZ3 Machine force/displacement output

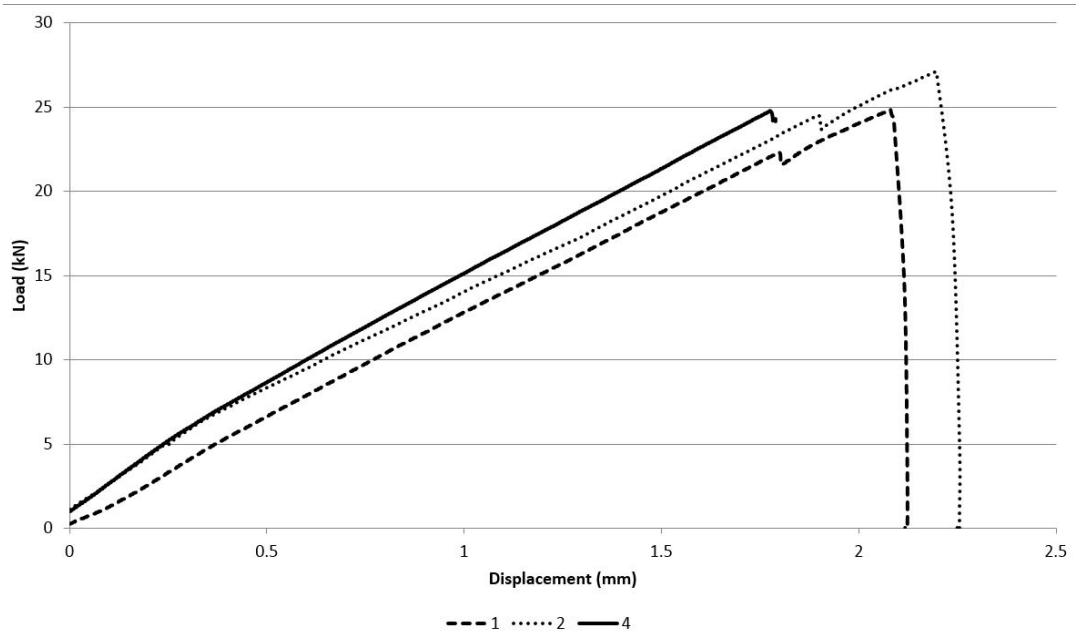

Figure 7.3: TZ5 Machine force/displacement output

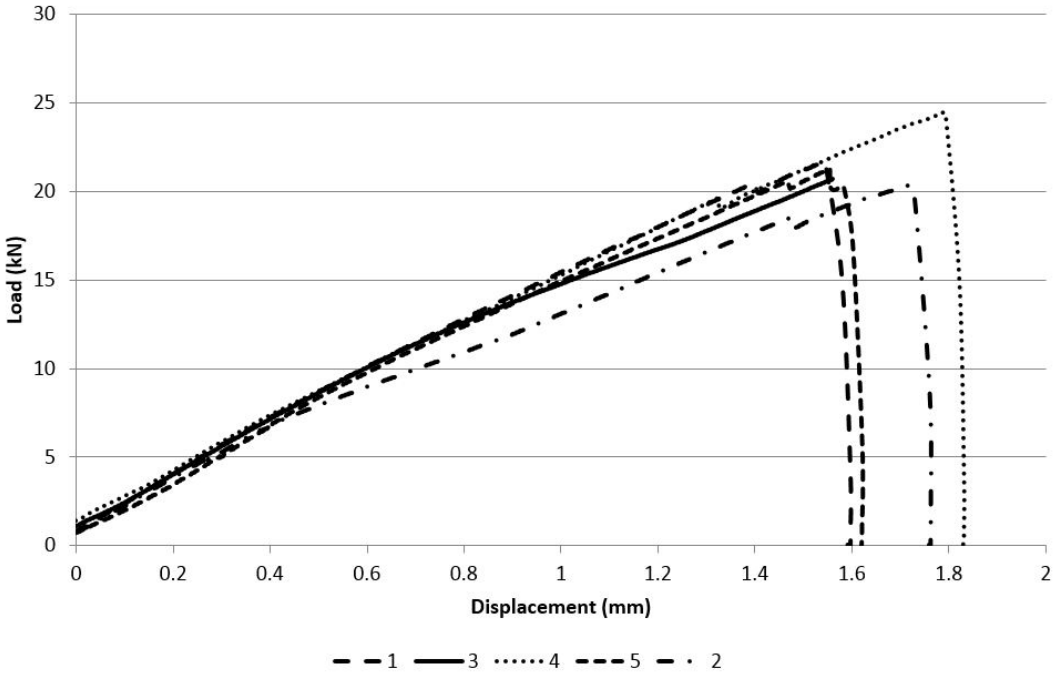

Figure 7.4: TZ6 Machine force/displacement output

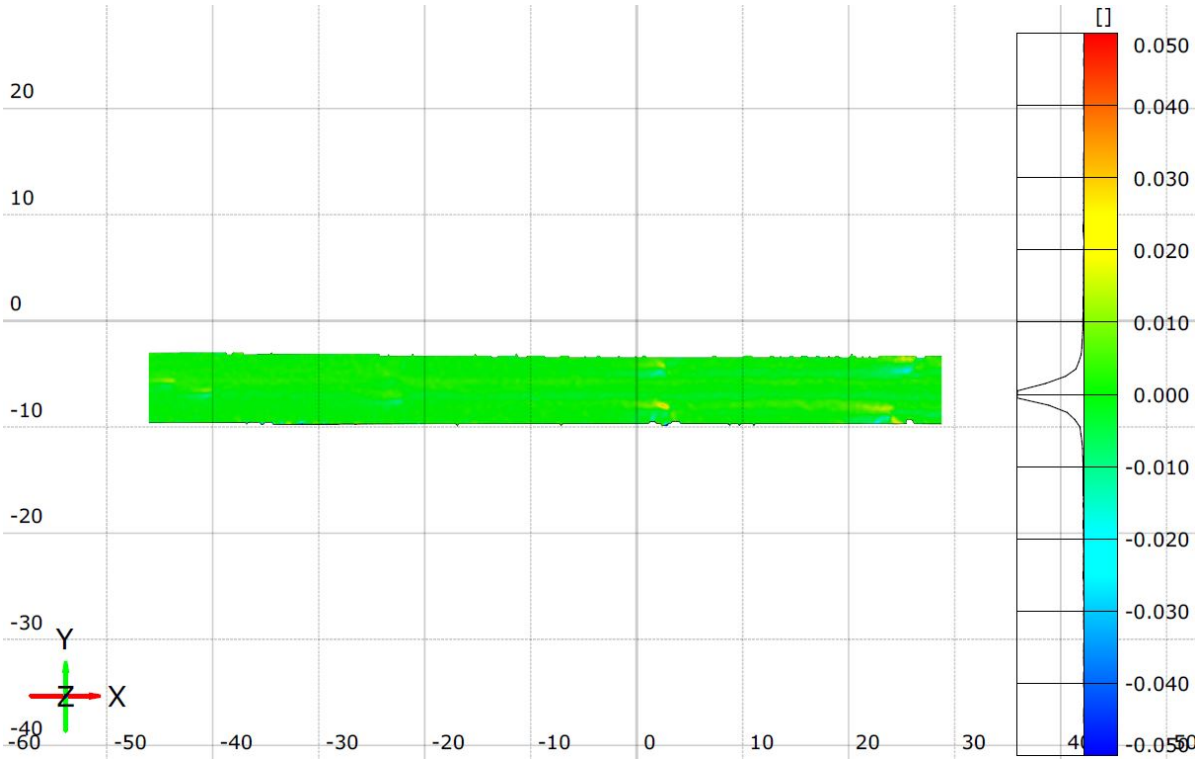

Figure 7.5: TZ2-1 Shear strain

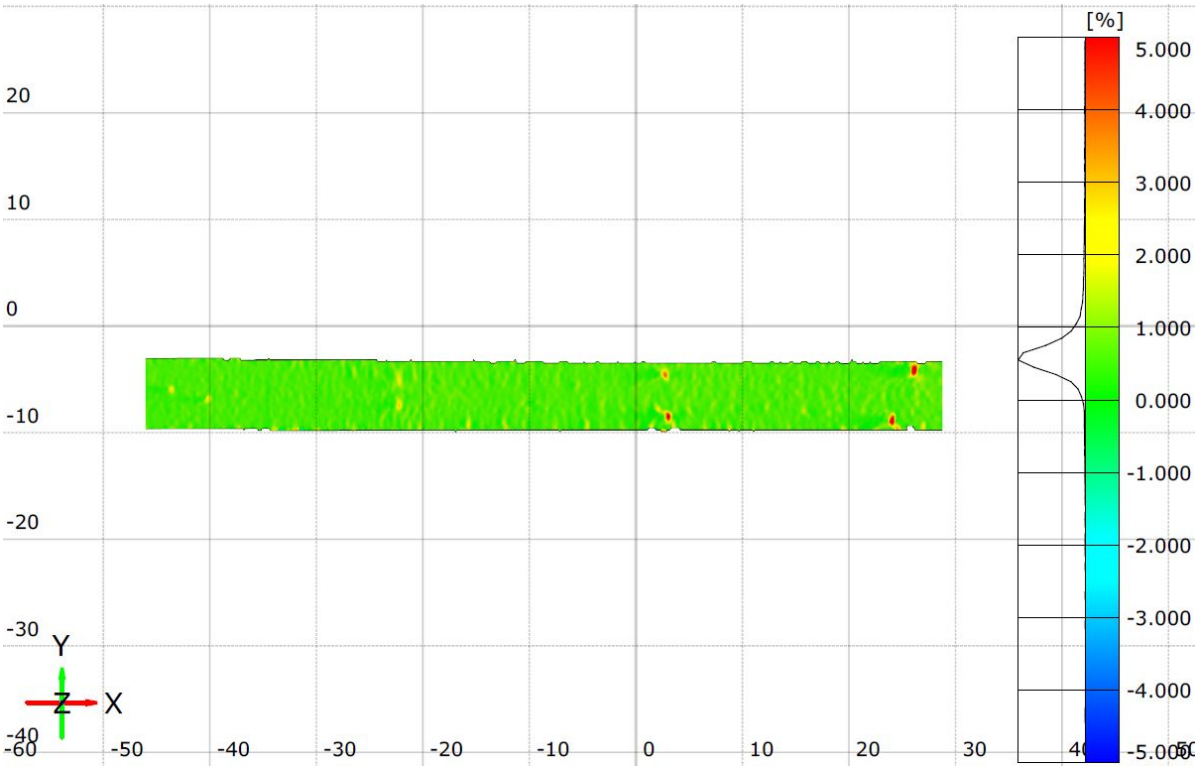

Figure 7.6: TZ2-1 Strain

Figure 7.7: TZ3-4 Shear strain

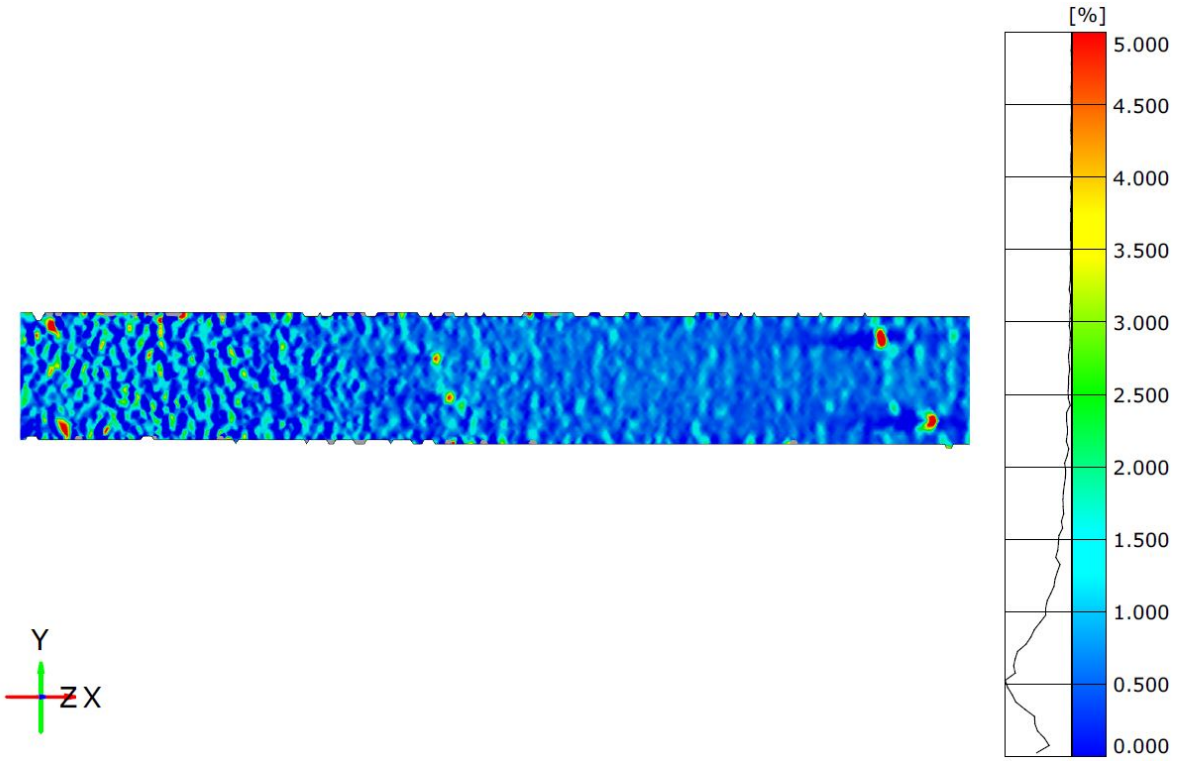

Figure 7.8: TZ3-4 Strain

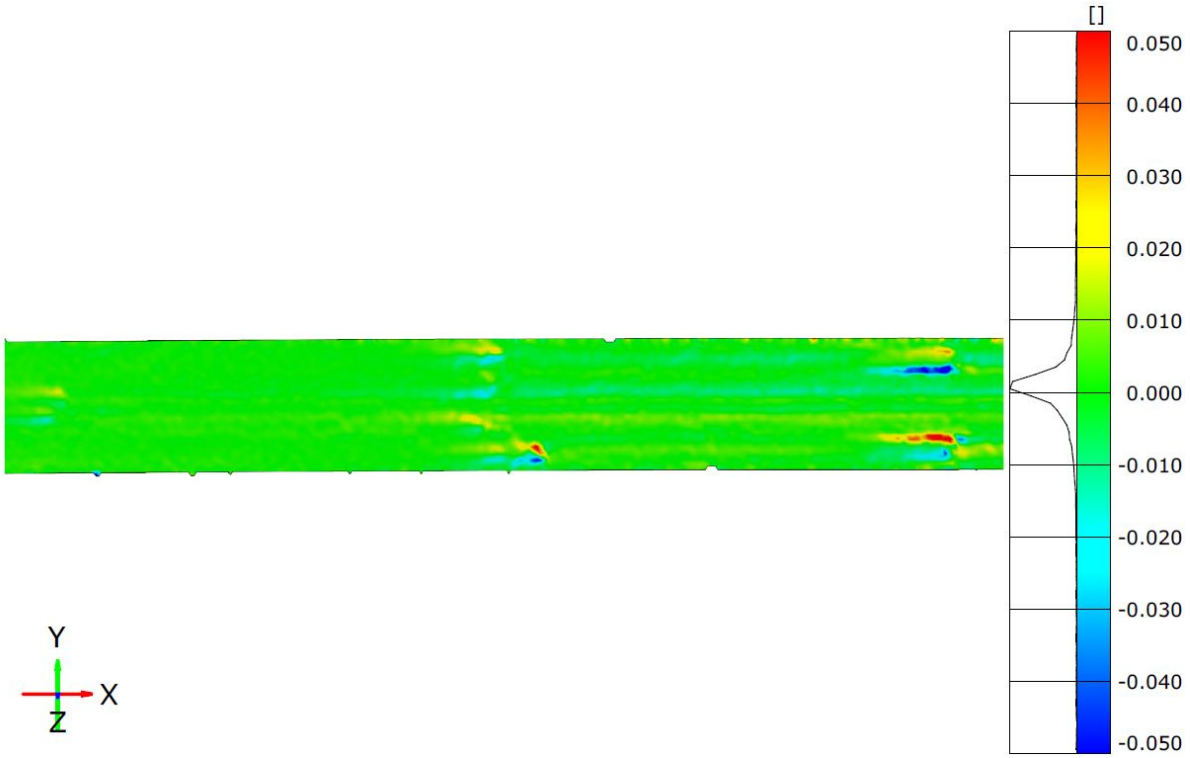

Figure 7.9: TZ5-1 Shear strain

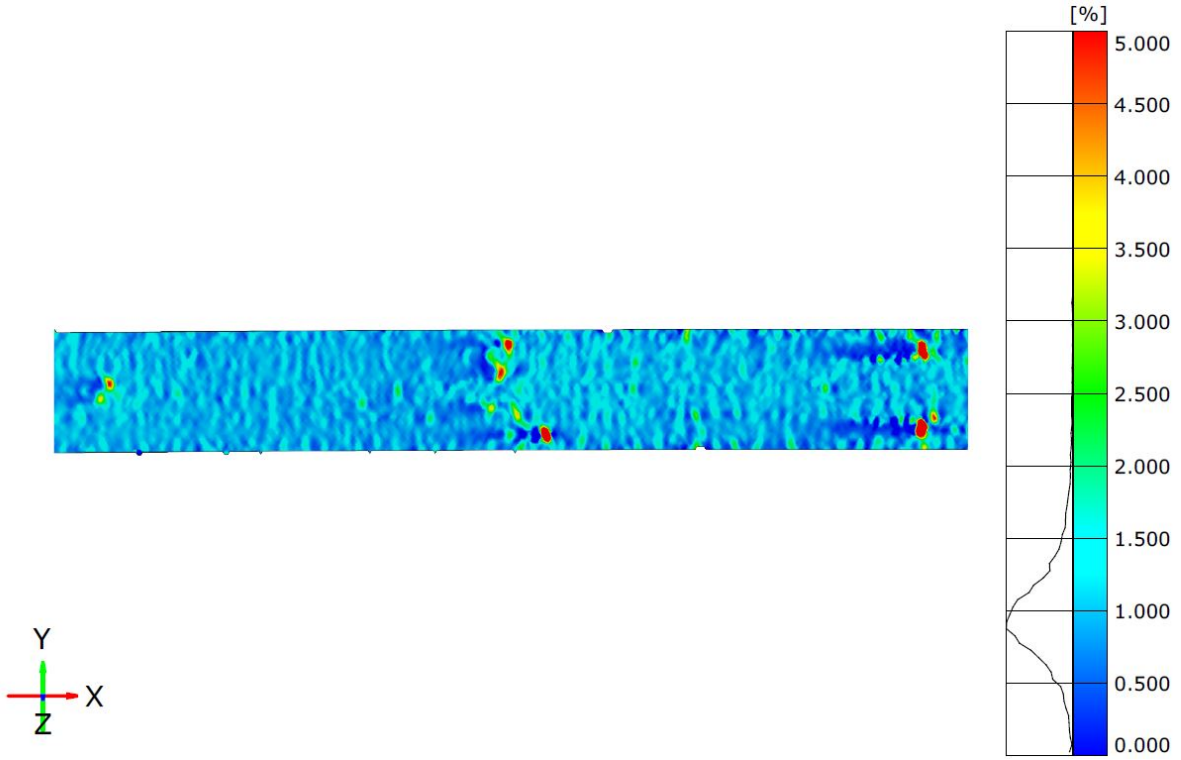

Figure 7.10: TZ5-1 Strain

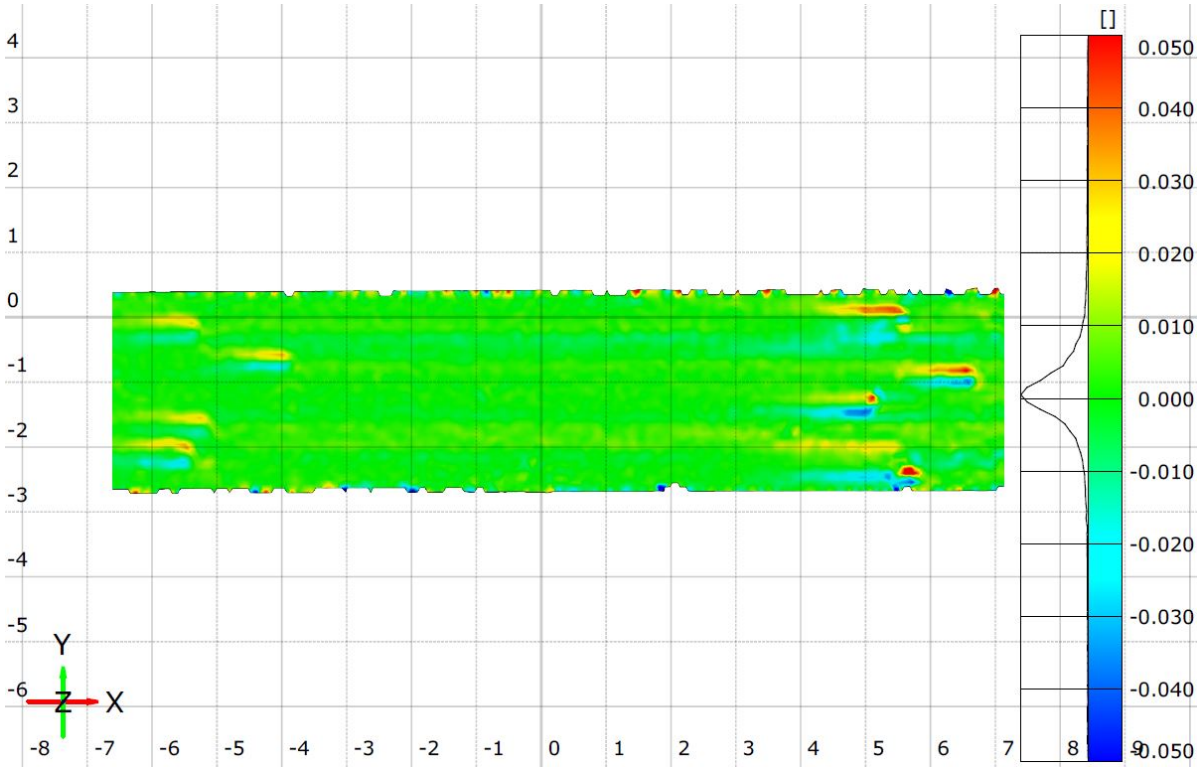

Figure 7.11: TZ6-5 Shear strain

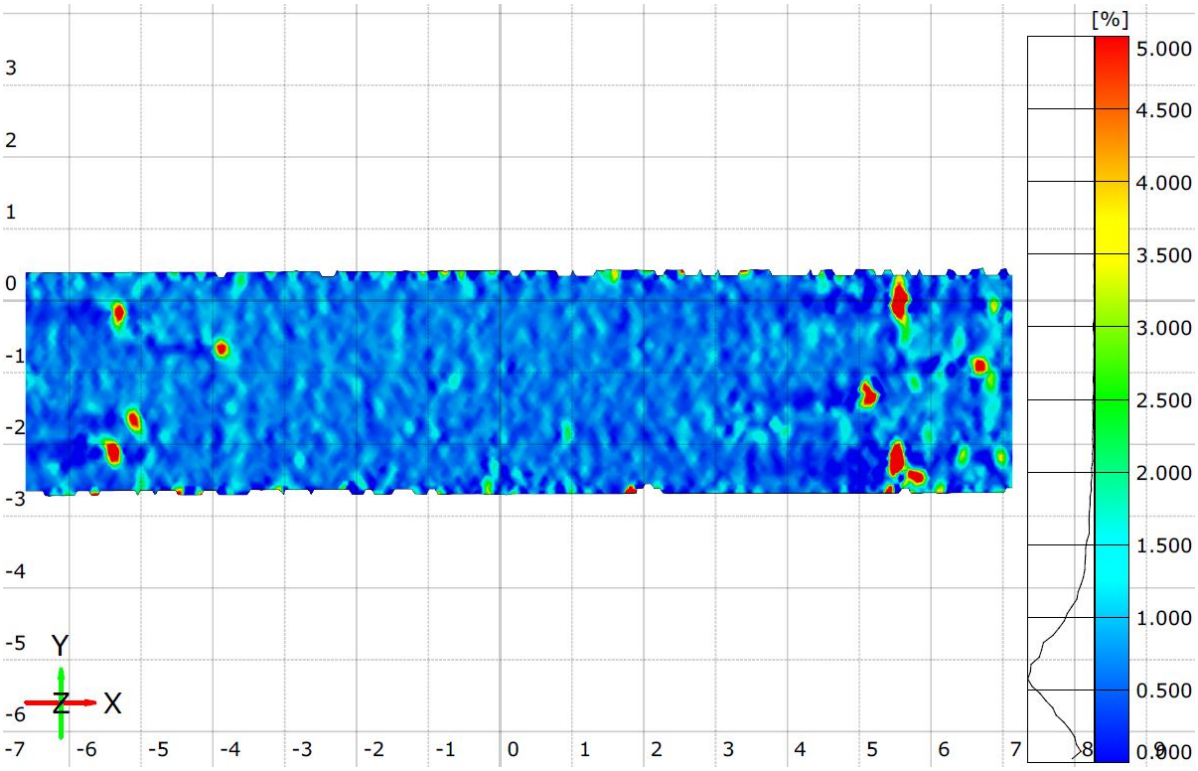

Figure 7.12: TZ6-5 Strain

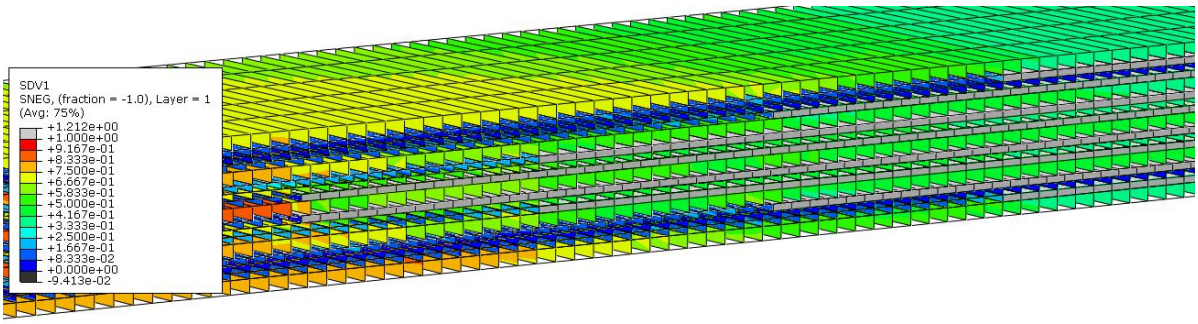

Figure 7.13: TZ1 Tensile fiber failure mode criterion visualization

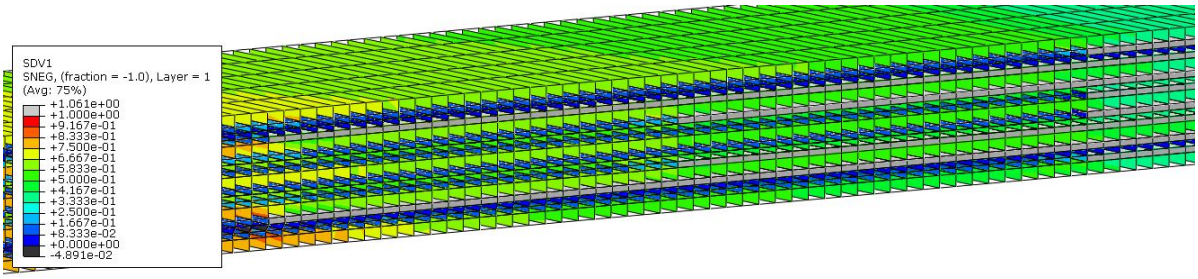

Figure 7.14: TZ3 Tensile fiber failure mode criterion visualization

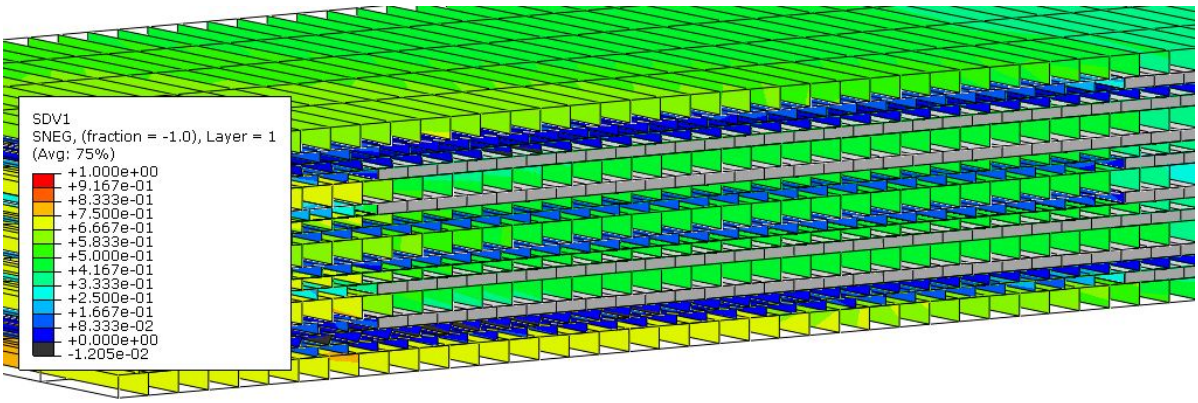

Figure 7.15: TZ4 Tensile fiber failure mode criterion visualization

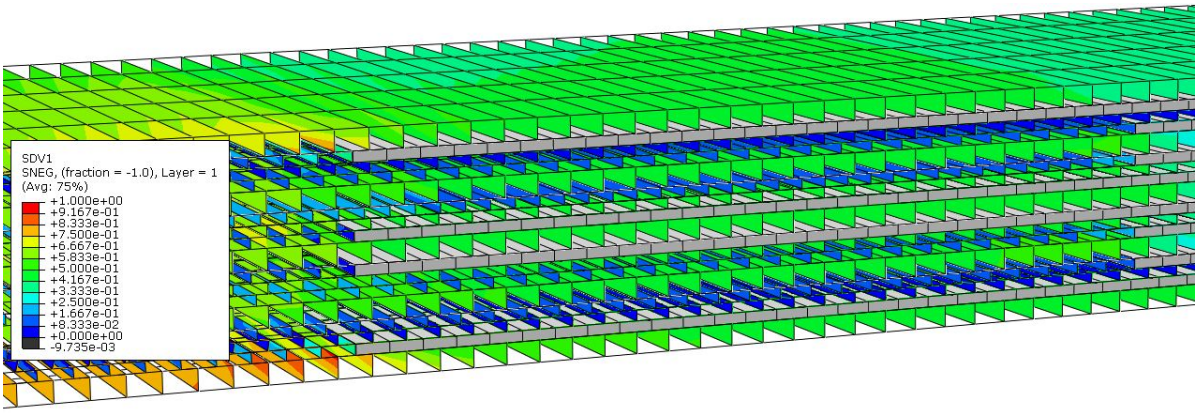

Figure 7.16: TZ6 Tensile fiber failure mode criterion visualization

Bibliography

[1] Analytical and numerical residual stress models for fiber metal laminates – comparison and application. *Procedia Materials Science*, 2:68 – 73, 2013. ISSN 2211-8128. Materials Science Engineering, Symposium B6 - Hybrid Structures.

[2] R. C. Alderliesten. *Fatigue and fracture of fibre metal laminates*. Springer International Publishing, 2017. ISBN 978-3-319-56227-8.

[3] ASTM. ASTM D5528-13 standard test method for mode i interlaminar fracture toughness of unidirectional fiber-reinforced polymer matrix composites. *ASTM International*, 2013.

[4] ASTM. ASTM D7905 standard test method for determination of the mode ii interlaminar fracture toughness of unidirectional fiber-reinforced polymer matrix composites. *ASTM International*, 2014.

[5] A.C. Asundi. Fiber metal laminates: An advanced material for future aircraft. *Journal ofMaterials Processing Technology*, 63:216–211, 1997.

[6] G. Barenblatt. The mechanical theory of equilibrium cracks in brittle fracture. *Advances in Applied Mechanics*, 7:55–129, 12 1962.

[7] B. R. K. Blackman, H. Hadavinia, A. J. Kinloch, and J. G. Williams. The use of a cohesive zone model to study the fracture of fibre composites and adhesively-bonded joints. *International Journal of Fracture*, 119(1), Jan 2003.

[8] E. C. Botelho, Rogério Almeida Silva, Luiz Cláudio Pardini, and Mirabel Cerqueira Rezende. A review on the development and properties of continuous fiber/epoxy/aluminum hybrid composites for aircraft structures. *Materials Research*, 9(3):247–256, 2006.

[9] A. Buczynski. *Development of a carbon-fiber/stainless steel laminate concept— improving the bearing characteristics of carbon-fiber composites by addition of steel strip reinforcements*. Master's thesis, Delft University of Technology, Delft, 2009.

[10] P. P. Camanho and C.G. Davila. Mixedmode decoheseion fe for simulation of delamination in composites. *NASA*, 2002.

[11] P. P. Camanho, C.M.L. Tavares, R. de Oliveira, A. T. Marques, and A.J.M. Ferreira. Increasing the efficiency of composite single-shear lap joints using bonded inserts. *Composites Part B: Engineering*, 36(5):372–383, 2005.

[12] P. P. Camanho, A. Fink, A. Obst, and S. Pimenta. Hybrid titanium–cfrp laminates for high-performance bolted joints. *Composites Part A: Applied Science and Manufacturing*, 40(12): 1826–1837, 2009.

[13] C.C Chiao and T.T. Chiao. Aramid fibers and composites. *Handbook of Composites*, pages 272–317, 1982.

[14] R.G. Cuntze. The predictive capability of failure mode concept-based strength criteria for multi-directional laminates—part b. *Composites Science and Technology*, 64(3):487 – 516, 2004. Failure criteria in fibre reinforced polymer composites Part C: Additional theories conclusions and recommendations.

[15] R.G. Cuntze and A. Freund. The predictive capability of failure mode concept-based strength criteria for multidirectional laminates. *Composites Science and Technology*, 64(3):343 – 377, 2004. Failure criteria in fibre reinforced polymer composites Part C: Additional theories conclusions and recommendations.

[16] H. M. Deuschle and Alfred Puck. Application of the puck failure theory for fibre-reinforced composites under three-dimensional stress: Comparison with experimental results. *Journal of Composite Materials*, 47(6-7):827–846, 2013.

[17] D.S. Dugdale. Yielding of steel sheets containing slits. *Journal of the Mechanics and Physics of Solids*, 8(2):100 – 104, 1960.

[18] A.G. Evans and W.F Adler. Kinking as a mode of structural degradation in carbon fiber composites. *Acta Met.*, 26:725 – 738, 1978.

[19] A. Fink. *Lokale Metall-Hybridisierung zur Effizienzsteigerung von Hochlastfügestellen in Faserverbundwerkstoffen*. PhD thesis, DLR, 2014.

[20] A. Fink, B. Kolesnikov, and H. Wilmes. Cfrp-titanium hybrid - improving composite structure coupling. Technical report, DLR, 05 2005.

[21] A. Fink, P. P. Camanho, J. M. Andrés, E. Pfeiffer, and A. Obst. Hybrid cfrp/titanium bolted joints: Performance assessment and application to a spacecraft payload adaptor. *Composites Science and Technology*, 70(2):305–317, 2010.

[22] R. M. Frizzell, C. T. McCarthy, and M. A. McCarthy. An experimental investigation into the progression of damage in pin-loaded fibre metal laminates. *Composites Part B: Engineering*, 39 (6):907–925, 2008.

[23] T.H. Hahn and J.G. Williams. Compression failure mechanisms in unidirectional composites. *NASA*, 1984.

[24] P. W. Harper and Stephen R. Hallett. Cohesive zone length in numerical simulations of composite delamination. *Engineering Fracture Mechanics*, 75(16):4774–4792, 2008.

[25] L. J. Hart-Smith. *Mechanically-Fastened Joints for Advanced Composites — Phenomenological Considerations and Simple Analyses*, pages 543–574. Springer US, Boston, MA, 1980.

[26] Z. Hashin. Failure criteria for unidirectional fiber composites. *J. Appl. Mech 47*, pages 329–334, 1980.

[27] J. Helm and R. J. Deaner. Off-axis two-dimensional digital image correlation. Technical report, Acopian Engineering Center, 12 2017.

[28] Hibbit, Karlsson, and Sorensen. *ABAQUS/Standard Analysis User's Guide*. Hibbit, Karlsson, Sorensen Inc., USA, 2014.

[29] R Hill. The mathematical theory of plasticity. *Oxford University Press*, 1950.

[30] A. Hillerborg, M. Modéer, and P.-E. Petersson. Analysis of crack formation and crack growth in concrete by means of fracture mechanics and finite elements. *Cement and Concrete Research*, 6(6):773 – 781, 1976.

[31] M.J Hinton, A.S Kaddour, and P.D Soden. A further assessment of the predictive capabilities of current failure theories for composite laminates: comparison with experimental evidence. *Composites Science and Technology*, 64(3):549 – 588, 2004. Failure criteria in fibre reinforced polymer composites Part C: Additional theories conclusions and recommendations.

[32] J. M. Hundley. *Multi-Scale Progressive Failure Modeling of Titanium-Graphite Fiber Metal Laminates*. PhD thesis, University of California, Los Angeles, 2009.

[33] C. Hühne, A.-K. Zerbst, G. Kuhlmann, C. Steenbock, and R. Rolfes. Progressive damage analysis of composite bolted joints with liquid shim layers using constant and continuous degradation models. *Composite Structures*, 92(2):189 – 200, 2010. ISSN 0263-8223.

[34] A. S Kaddour and M. J. Hinton. Maturity of 3d failure criteria for fibre-reinforced composites: Comparison between theories and experiments: Part b of wwfe-ii. *Journal of Composite Materials*, 47(6-7):925–966, 2013.

[35] J.G. Kaufman. Fracture toughness of 7075-t6 and -t651 sheet, plate and multilayered adhesive-bonded panels. *Journal of Basic Engineering*, 89:503 – 507, 1967.

[36] S.U. Khan, R.C. Alderliesten, and R. Benedictus. Delamination growth in fibre metal laminates under variable amplitude loading. *Composites Science and Technology*, 69(15):2604 – 2615, 2009.

[37] UA Khashaba, SM Aldousari, and IMR Najjar. Behavior of [0]8 woven composites under combined bending and tension loading: part i experimental and analytical. *Journal of Composite Materials*, 46(11):1345–1355, 2012.

[38] B Kolesnikov. Composite material with a reinforced connecting area, 2000. PCT/DE99/00790.

[39] B. Kolesnikov, L. Herbeck, and A. Fink. Cfrp/titanium hybrid material for improving composite bolted joints. *Composite Structures*, 83(4):368–380, 2008.

[40] J. Kosmann, Dirk Holzhüter, Thomas Löbel, Christian Hühne, and Martin Schollerer. High resolution digital image correlation strain measurements of adhesively bonded joints. In *ECCM17 - 17th European Conference on Composite Materials*, June 2016.

[41] R. Li, N. Huong, A. Crosky, A.P. Mouritz, D. Kelly, and P. Chang. Improving bearing performance of composite bolted joints using z-pins. *Composites Science and Technology*, 69(7):883 – 889, 2009. ISSN 0266-3538.

[42] Mallick. *Fiber-reinforced Composites - Materials Manufacturing and Design*. CRC Press, third edition, 2007.

[43] G.V. Marannano and A. Pasta. An analysis of interface delamination mechanisms in orthotropic and hybrid fiber-metal composite laminates. *Engineering Fracture Mechanics*, 74(4):612 – 626, 2007. Fracture and Damage in Engineering Applications.

[44] A. Marzuki. Effect of anodizing on strength of carbon-fibre aluminium-laminated composites. *Advanced Materials Research*, 748:216–221, 2013.

[45] N. McCormick and Jerry Lord. Digital image correlation. *Materials Today*, 13(12):52 – 54, 2010.

[46] E. W. Medenblik. *Titanium fibre-metal laminates*. Master's thesis, Delft University of Technology, Delft, 1994.

[47] L Meng, G Jin, and X Yao. Errors caused by misalignment of the optical camera axis and the object surface in the dscm. *Journal of Tsingua University*, 46:1930–1932+1936, 11 2006.

[48] C. Meola, Antonino Squillace, Giuseppe Giorleo, and Luigi Nele. Experimental characterization of an innovative glare® fiber reinforced metal laminate in pin bearing. *Journal of Composite Materials*, 37(17):1543–1552, 2003.

[49] J.L. Miller. Preliminary evaluation of hybrid titanium composite laminates. Technical report, Virginia:NASA, 1994.

[50] Y. Nekoshima. Mechanical behavior of thin titanium films/cfrp hybrid laminates containing transition region. *THE 19TH INTERNATIONAL CONFERENCE ON COMPOSITE MATERIALS*, 2013.

[51] Susan O. Palmer, Alan Nettles, and C C. Poe. An experimental study of a stitched composite with a notch subjected to combined bending and tension loading. *NASA Langley Research Center*, 09 1999.

[52] B. Pan, Kemao Qian, Huimin Xie, and Anand Asundi. Two-dimensional digital image correlation for in-plane displacement and strain measurement: a review. *Measurement Science and Technology*, 20(6):062001, 2009.

[53] F.J. Pellenkoft. *Investigation on the elastic behaviour of and crack propagation in Glare loaded by combined tension and bending*. Master's thesis, TU Delft, 2000.

[54] E. Petersen and C. Hühne. Determination of critical energy release rates for steel-cfrp interfaces considering residual thermal stresses. In *European Conference on Spacecraft Structures, Materials and Environmental Testing ESA-ESTEC, Noordwijk NL*, 2018.

[55] E. Petersen, R.G. Cuntze, and C. Hühne. Experimental determination of material parameters in cuntze's failure-mode-concept-based ud strength failure conditions. *Composites Science and Technology*, 134(Supplement C):12 – 25, 2016.

[56] E. Petersen, D. Stefaniak, and C. Hühne. Experimental investigation of load carrying mechanisms and failure phenomena in the transition zone of locally metal reinforced joining areas. *Composite Structures*, 182:79–90, 2017.

[57] S.T. Pinho, P. Robinson, and L. Iannucci. Fracture toughness of the tensile and compressive fibre failure modes in laminated composites. *Composite Science and Technology*, 66:2069 – 2079, 2005.

[58] F. Pottmeyer, J. Bittner, P. Pinter, and K. A. Weidenmann. In-situ ct damage analysis of metal inserts embedded in carbon fiber-reinforced plastics. *Experimental Mechanics*, 57(9):1411–1422, Nov 2017. ISSN 1741-2765.

[59] R. Prussak, D. Stefaniak, Christian Hühne, and Michael Sinapius. Residual stresses in intrinsic ud-cfrp-steel-laminates - experimental determination, identification of sources, effects and modification approaches. In *20th Symposium on Composites*, volume 825 of *Materials Science Forum*, pages 369–376. Trans Tech Publications, 8 2015.

[60] T. Puzio. *The influence of the Transition Zone on the structural behavior of pin connected areas in local metal reinforced composites*. Master's thesis, TU Delft, 2017.

[61] C.D. Rans. 2 - bolted joints in glass reinforced aluminium (glare) and other hybrid fibre metal laminates (fml). In Pedro Camanho, , and Liyong Tong, editors, *Composite Joints and Connections*, Woodhead Publishing Series in Composites Science and Engineering, pages 35 – 76. Woodhead Publishing, 2011.

[62] J. R. Rice. A path independent integral and the approximate analysis of strain concentration by notches and cracks. *Journal of Applied Mechanics*, 35:379–386, 1968.

[63] J. R. Rice. The mechanics of earthquake rupture. In *in Physics of the Earth's Interior, edited by A.M. Dziewonski and E. Boschi*, pages 555–649, 1980.

[64] E.F. Rybicki and M.F. Kanninen. A finite element calculation of stress intensity factors by a modified crack closure integral. *Engineering Fracture Mechanics*, 9:931 – 938, 1997.

[65] T. Sinmazçelik, Egemen Avcu, O. Bora, Mustafa, and Onur Çoban. A review: Fibre metal laminates, background, bonding types and applied test methods. *Materials & Design*, 32(7):3671–3685, 2011.

[66] W. J. Slagter and H. F. Wu. Parametric studies of bearing strength for fiber/metal laminates. Technical report, Structural Laminates Company, Delft, 1992. SLC-report SL-019-E.

[67] P. Soltani, M. Keikhosravy, R. H. Oskouei, and C. Soutis. Studying the tensile behaviour of glare laminates: A finite element modelling approach. *Applied Composite Materials*, 18(4):271–282, 2011.

[68] D. Stefaniak, Kappel Erik, Kolesnikov Boris, and Hühne Christian. Improving the mechanical performance of unidirectional cfrp by metal-hybridization. In *ECCM15 - 15th European Conference on Composite Materials*, June 2012.

[69] Dassault Systemes. Surface-based cohesive behavior lecture 6, 2017. URL 50.16.225.63/v2016/books/usb/pt09ch37s01alm66.html. 2017-12-27.

[70] S. C. Tan and Jose Perez. Progressive failure of laminated composites with a hole under compressive loading. *Journal of Reinforced Plastics and Composites*, 12(10):1043–1057, 1993.

[71] Stephen W. Tsai and Edward M. Wu. A general theory of strength for anisotropic materials. *Journal of Composite Materials*, 5(1):58–80, 1971.

[72] A. Turon. *Simulation of delamination in composites under quasi-static and fatigue loading using cohesive zone models*. PhD thesis, Universitat de Girona, 2006.

[73] A. Turon, Pedro Camanho, and Josep Costa. An engineering solution for using coarse meshes in the simulation of delamination with cohesive zone models. *NASA*, 04 2005.

[74] A. Turon, C. G. Dávila, P. P. Camanho, and J. Costa. An engineering solution for mesh size effects in the simulation of delamination using cohesive zone models. *Engineering Fracture Mechanics*, 74(10):1665–1682, 2007.

[75] R. G. J. Van Rooijen. *Bearing Strength Characteristics of Standard and Steel Reinforced GLARE*. PhD thesis, TU Delft, 2006.

[76] R. G. J. van Rooijen, J. Sinke, T. J. de Vries, and S. van der Zwaag. The bearing strength of fiber metal laminates. *Journal of Composite Materials*, 40(1):5–19, 2005.

[77] A. Vlot, L. B. Vogelesang, and T. J. de Vries. Towards application of fibre metal laminates in large aircraft. *Aircraft Engineering and Aerospace Technology*, 71(6):558–570, 1999.

[78] L.B Vogelesang and A. Vlot. Development of fibre metal laminates for advanced aerospace structures. *Journal of Materials Processing Technology*, 103(1):1–5, 2000.

[79] K. Y. Volokh. Comparison between cohesive zone models. *Communications in Numerical Methods in Engineering*, 20(11):845–856, 2004.

[80] W.X. Wang. galvanic corrosion-resistant carbon fiber metal laminates. *16th international conference on composite materials*, 2007.

[81] H.F. Wu and W.J. Slagter. Parametric studies of bearing strength for fibre metal laminates. *J Aircraft*, 31:936–945, 1994.

[82] Z. Zou, S.R. Reid, and Shuguang Li. A continuum damage model for delamination in laminated composites. *Journal of the Mechanics and Physics of Solids*, 51:333–356, 02 2003.